Digital Signal Processing Assessment for Optical Coherent Receiver using Dual-Polarization Quadrature Phase Shift Keying Modulation

Mathieu Chagnon

Department of Electrical & Computer Engineering
McGill University
Montreal, Canada

October 2010

A thesis submitted to McGill University in partial fulfillment of the requirements for the degree of Master of Engineering

Abstract

In this work, we evaluate different approaches of digital signal processing applied after a coherent receiver in order to recover the binary information of an optical signal modulated in Dual-Polarization Quadrature Phase Shift Keying. We explain in details the functioning of a coherent receiver as well as the optical and electrical signals travelling inside. We present the criteria of the two lasers employed for modulation and demodulation, i.e., the *signal* and *local oscillator* lasers, as a function of the modulation format and the binary rate. We expose all the required signal processing for information recovery out of a coherent receiver and mention those who will be assessed in this work, along with the reason of their selection. Subsequently, the metric to assess the different methods is introduced. The latter is twofold and consists of the computational complexity and the final bit error rate that each approach yields. The schematics of the test bed follows in parallel with the parameter space of our setup. The computational complexity and the bit error rate of ten different approaches are presented, and an optimal configuration of methods and parameters to use for such modulation and receiver is deduced.

Résumé

Dans ce travail, nous évaluons différentes approches de traitement de signaux numériques pour un récepteur cohérent optique dans le but de recouvrir l'information binaire d'un signal modulé sur double polarization et quatre niveaux de phase, ou « *Dual-Polarization QPSK* ». Nous expliquons en détail le fonctionnement d'un récepteur cohérent ainsi que les signaux optiques et électriques qui s'y propagent. Nous présentons les critères des deux lasers utilisés pour la modulation et la démodulation cohérente, i.e., les lasers *signal* et *oscillateur local*, en fonction du format de modulation utilisé et du taux binaire. Nous exposons tous les traitements de signaux numériques requis pour recouvrir l'information sortant d'un récepteur cohérent et mentionnons ceux qui seront évalués dans ce travail ainsi que les raisons de leur sélection. Par la suite, nous introduisons la métrique d'évaluation des différentes approches. Cette dernière comporte deux facettes, soit la complexité de calcul des différents algorithmes et paramètres utilisés ainsi que le taux d'erreur binaire final que l'ensemble des processus produisent lorsqu'une certaine approche est employée. La présentation schématique du banc de test suit de concert avec l'espace des paramètres du montage. La complexité de calcul et le taux d'erreur binaire de dix différentes approches sont présentés et une configuration optimale des paramètres et méthodes pour un tel format de modulation et receveur est déduite.

Acknowledgments

I would like to take the opportunity at the very beginning of this work to thank the persons who inspired and help me, directly or indirectly, in the completion of this two-year-long work that consist my Master's Thesis.

First of all, I'll like to warmly thank my Thesis supervisor, Professor David V. Plant. This man was a true inspiration and a model throughout my Master's degree. He provided me with fruitful comments and advises, shone light on what top tier university research is and put me in contact with worldwide renowned experts to work with. He was able to seize me and suggest a research topic of strong personal interest for me to work on to keep me motivated and involved throughout the project.

I would also like to thank Prof. Nicolas Godbout from the Engineering Physics Department at École Polytechnique de Montréal. Prof. Godbout had the teaching talent to contagiously give me his passion for photonics and is the reason why I started my Master's at McGill University with Prof. Plant.

I could not end my acknowledgments without mentioning my close family. I sincerely want to thank both my parents and my sister, whom I profoundly love. They pushed me to pursue my dreams, eased my way in life and taught me perseverance. I would also want to express gratitude to all my friends who, in the years, forged my opinions and pushed me to become the person I am today. Without you guys, I would very certainly not be the man I am.

Finally, thanks to all who surround me and have, in a certain way, positively and most of the time unconsciously influenced me.

My final comment: There is always something to learn from someone.

Table of Content

List of Figures

List of Acronyms

ADC : Analog to Digital Converter
AM : Amplitude Modulation
ASIC : Application Specific Integrated Circuit
AWGN : Additive White Gaussian Noise
BER : Bit Error Rate
BPSK : Binary Phase Shift Keying
C : Complex
CC : Computational Complexity
CD: Chromatic Dispersion
CD^{-1} : Chromatic Dispersion Compensation
CFO : Carrier Frequency Offset
CMA : Constant Modulus Algorithm
CMOS : Complementary Metal Oxyde Semiconductor
CPE : Carrier Phase Estimation
DAF : Delay and Add Filter
DC : Direct Current
DD : Direct Detection
DFT : Discrete Fourier Transform
DIT : Decimation In Time
DP: Dual Polarization
DP-QPSK : Dual Polarization Quadrature Phase Shift Keying
DSP : Digital Signal Processing
EDFA : Erbium Doped Fiber Amplifier
FFT : Fast Fourier Transform
FSE : Fractionally Spaced Equalizer
FWHM : Full Width at Half Maximum
GVD : Group Velocity Dispersion
I : In-phase
IM : Intensity Modulation
IP : Internet Protocal
I-Q : In-phase - Quadratic-phase
ISI : Intersymbol Interference
LO : Local Oscillator

MF : Matched Filter
MIMO : Multiple Input Multiple Output
M-PSK : Multiple Phase Shift Keying
NL : Nonlinear
OPT : Optimized pulse
OSNR : Optical Signal to Noise Ratio
PAR : Phase Ambiguity Resolver
PBS : Polarization Beam Splitter
PC : Polarization Controler
PDL : Polarization Dependent Loss
PLL : Phase Locked Loop
PM : Phase Modulation
PMD : Polarization Mode Dispersion
PMC : Polarization Maintaining Combiner
PMS : Polarization Maintaining Splitter
Pol.-XPM : Polarization Cross-Phase Modulation
PolMux : Polarization Mutliplex
PSD : Power Spectral Density
PSK : Phase Shift Keying
PSP : Principal State of Polarization
Q : Quadratic-phase
QAM : Quadrature Amplitude Modulation
QPSK : Quadrature Phase Shift Keying
R : Real
RA : Real addition
RC : Raised Cosine
RM : Real Multiplication
ROSNR : Required Optical Signal to Noise Ratio
RRC : Root Raised Cosine
SMF : Single Mode Fiber
SNR : Signal to Noise Ratio
SPM : Self-Phase Modulation
SSFM : Split-Step Fourier Method
TE : Transverse Electric
TM : Transverse Magnetic
XPM : Cross-Phase Modulation

> *"If we knew what it was we were doing, it wouldn't be called research, would it?"*
>
> - Albert Einstein

Chapter 1 : Introduction

1.1 – Motivation

The demand for increased bandwidth is ever present with the advent of new telecommunication services, intensive bit rate demanding applications, and the increase of internet subscribers worldwide. The need for increasing the bit rates of Ethernet has already been clearly voiced to keep pace with the overabundance of data services that drive the exponential network traffic growth between 40 and 90 percent per year, most notably with the increase of database-centric users and applications [1, 2]. The development of higher bit rate transponder technology is progressing rapidly to meet the needs of next-generation IP carrier networks. IP traffic growth continues together with the need for ever higher-speed ports on IP routers and Ethernet switches.

The optical fibre is known to be the transmission medium of excellence for large throughputs and long-haul transmissions. Several characteristics of the optical field travelling in a fibre can serve to modulate information. These parameters are the amplitude, the phase and the polarization. In fact, it is well known that the total bit rate carried within a fiber is a simple product of the symbol rate, the bits per symbol, the number of carrier and the number of orthogonal polarizations used [3]. Increasing needs for higher transmission rates push the need to come up with new ways to modulate and demodulate signals for telecommunication.

1.2 – Problem Statement

Up to recently, currently deployed fibre networks were capable to keep up with the burgeoning bandwidth demands by increasing the symbol rate of single bit per symbol intensity modulated (IM) systems. IM modulated signals use standard direct detection (DD) receivers, called IM-DD, where only the squared amplitude of the optical field is detected. The increase of the bit rate beyond 10 Gb/s using only this approach was proven to be problematic, as high-speed electronic components rapidly come to be a strong bottleneck for throughputs and their cost rapidly increases with bandwidth. Moreover, broader modulation spectra, from shorter time duration bits, increase the impact of fibre transmission impairments. As an example, a fourfold increase of the bit rate is 16 times less tolerant to fibre chromatic dispersion. Moreover, telecommunications operators have been discovering significant amounts of polarization dependant delay, also referred to as polarization mode dispersion (PMD), in many of their installed fibres. As PMD has a fixed distribution for a given fibre length, it has a detrimental effect on the signal to noise ratio that goes proportionally with the data rate, rapidly rendering symbols indifferentiable.

Coherent optical receivers allow access not to the power, but the real amplitude, phase and even polarization of an optical field. Such type of receiver makes possible the use of higher order modulations format, where both the amplitude and the phase bear information. Additionally, they allow recovering information imprinted on the two orthogonal polarizations of an optical fibre; a process called polarization multiplexing (PolMux). These three degrees of freedom allow the former 1 bit/symbol scheme to radically increase to $2\log(M)/\log(2)$ bits/symbol for M different amplitude and phase combinations on dual polarizations. Fig. 1 shows constellations for various modulation schemes where the **I** axis represent the in-phase information and the **Q** axis the quadratic-phase, i.e. the information shifted by 90° with respect to **I**.

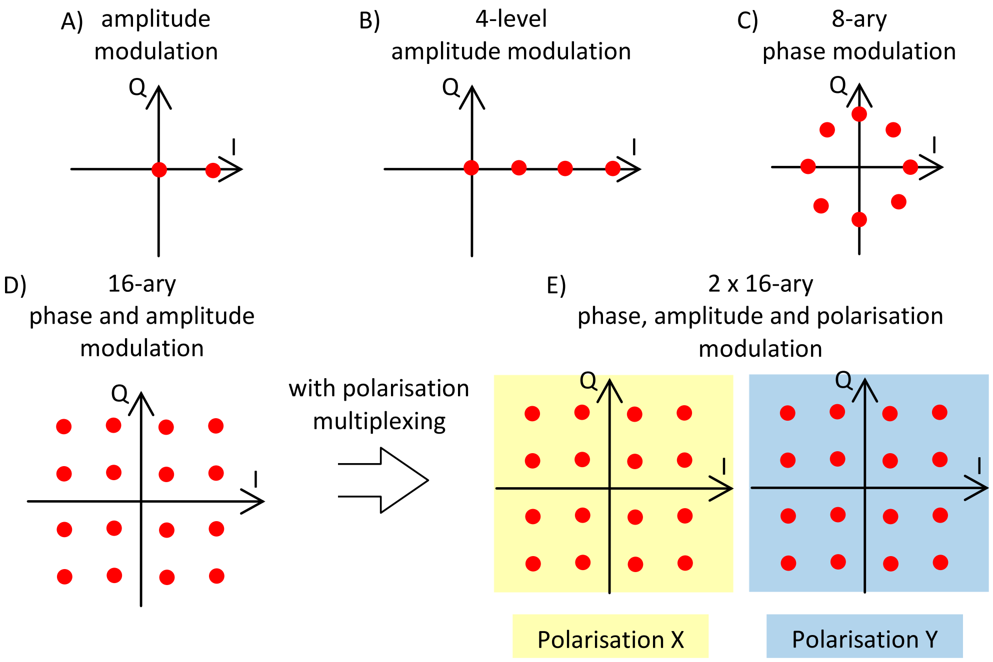

Fig. 1 – Constellations of various modulation constellations

It is interesting to compare modulation formats with the spectral efficiency they yield. The spectral efficiency is simply the bit rate divided by the required spectral width of a modulation format. As a mean of comparison, let's consider 3 modulation formats all operating on the same symbol rate of 10 Gsymbols/s, namely 1) the Non-Return-to-Zero Amplitude Shift Keying (NRZ-ASK) as depicted in Fig. 1-A, 2) the-Return-to-Zero Amplitude Shift Keying (RZ-ASK) at 50% duty cycle, also depicted in Fig. 1-A but where every "+1"s (furthest right dot) are always brought back to zero in the middle of the symbol duration, and finally 3) the Quadrature Phase Shift Keying (QPSK) which is a 4-ary phase modulation (refer to Fig. 1-C). The first thing to find to recover the spectral efficiency is the bit rate produced by the format. Both NRZ-ASK and RZ-ASK formats give 1 bit of information per symbol recovered whereas QPSK informs us of 2 bits per symbol. This gives bit rates of 10 Gb/s and 20 Gb/s respectively. The last required information is the full spectral width of the modulation scheme. This information depends on the type of pulse shape used, but we will assume a common pulse shape being a cardinal sine where the first null to appear after the central peak is located at a time equal to the symbol duration. In this case the

NRZ-ASK and the QPSK formats share the same full spectral (2-sided) width of 10 GHz while the RZ-ASK spreads over 20 GHz. Therefore, by dividing the bit rate with the spectral width we find the spectral efficiency of each format to be 1) 1 b/s/Hz for NRZ-ASK, 2) 0.5 b/s/Hz for RZ-ASK and 2 b/s/Hz for QPSK. Here we realize the increased efficiency and consequently the interest in using more complex modulation schemes like QPSK as they offer the possibility to send more binary information within a bandwidth. We will use the latter format in this thesis.

Coherent receivers use digital signal processing (DSP) to remove impairments and noise on the received signal in order to recover the information sent. Several different digital processes have to be applied to the collected signals for proper reconstruction of binary streams. Finding good ways to recover the information through DSP is now a sought after research topic

1.3 – Thesis Objective

The objective of this thesis is to analyze different approaches and various parameters embedded in the digital processes at the receiver for information recovery. We explain all the impairments we are facing at the receiver and detail different ways to mitigate them using digital signal processing. For some impairments mitigation processes, we will test completely different approaches while for others, we will vary parameters within the process that influence the final results. The metric we used to evaluate which method gives better results is twofold. First of all, we will calculate the final bit error rate (BER) that the overall recovery process yields when using a specific method. Secondly, we will count the total required number of real arithmetic operations of additions and multiplications for the entire information recovery required by each approach. For simplicity, we will name the sum of all real arithmetic operations the computer complexity (CC) of the approach. The lower the BER and the lower the CC give a better global digital signal process to apply for coherent receivers. With the plethora of modulation formats that an optical coherent receiver can recover, we will restrict ourselves only to Dual-Polarization Quadrature Phase Shift Keying, or DP-QPSK. Note that the terms “Dual-Polarization” and “Polarization Division Multiplexing” refer to the same principle.

1.4 – Thesis Organization

In Chapter 2, we will explain the use of direct detectors and of coherent receivers and will compare the two types of receivers. Will also lay out the basics of 90° optical hybrids and how they constitute the main part of a coherent receiver. We also introduce the mathematical representation of optical fields.

Required digital signal processing to recover the information sent on an optical link after a coherent receiver are presented in Chapter 3. All the impairments the processing has to deal with are introduced along with their origins and ways to mitigate them for proper information recovery.

In Chapter 4, we define which algorithms presented in the previous chapter and required for proper signal demodulation will be assessed in our study and we also present the metric we will use to compare different approaches.

Chapter 5 details the test bed used to collect the experimental data. We also unfold the characteristics we varied in the setup to accurately differentiate various DSP methods.

The sixth chapter exhibits the analysis of 10 different DSP approaches where either a DSP method or a parameter within a process is studied. Results are presented and a final DSP configuration for best information recovery of a DP-QPSK transmission is established.

Chapter 7 provides a summary of the work presented, as well as ideas for future work.

Chapter 2 : Coherent Receivers

2.1 – *Types of receivers*

Different types of receivers have to be used to demodulate specific formats. The more complex the modulation format, the more sophisticated the receiver will be. They are two main types of photoreceivers in optical communications: Direct-Detectors and Coherent Receivers.

2.1.1 – Direct-Detectors

The most basic type of receiver is the direct detector, where the power of light hitting a photodiode is proportionally converted into an electrical current. This type of detector, when used alone, can only demodulate amplitude modulation (AM), also called intensity modulation. This fundamental optical transmission scheme named Intensity Modulation with Direct Detection, or IM-DD is widely used in today's 10 Gbit/s optical transmissions, for both terrestrial and submarine systems [4]. Such a detector can be seen in the following Fig. 2-A, where E_s is the optical field at the receiver and $i(t)$ is the current after the photodetector. Sometimes, a low noise amplifier or a transimpedance amplifier is used to intensify the weak photocurrent due to the small incident optical power. The typical photodiode responsivity of $0.5\ \text{Amps/Watt}$. This type of detector can of course also be used for multi-level amplitude modulation, where a higher optical amplitude will directly result in a seemingly larger current.

Even if photodiodes are square-law detectors and recover the amplitude regardless of the phase, phase modulated (PM) signals can also be direct detected using such devices. In opposite to AM where the observed current directly represents the symbol transmitted, direct-detectors for phase modulated signals output a current that represent phase changes, or phase jumps of the optical signal and not the absolute value of the phase. Therefore, the bit stream has to be differentially encoded at the transmitter for the value of the photocurrent at the receiver to be representative of the initial information.

Fig. 2-B shows the general configuration of direct-detectors for Multiple Phase Shift Keying (M-PSK) modulated signals. The building block of such phase demodulators is the optical delay and add filter (DAF), more known as a Mach-Zehnder demodulator. A DAF consists of two branches into which the incoming signal equally separates in power. One branch delays the signal by the duration of the symbol, τ, while the other branch can delay or phase shift by constant value ϕ. For a binary phase shift keyed (BPSK) format, a single DAF filter is needed and $\phi = 0$. The more levels of phase used for modulation the more DAFs will be needed. For instance, a 4-phase modulation, called Quadrature Phase Shift Keying (QPSK), will require 2 DAFs with $\phi_1 = +\pi/4$ and $\phi_2 = -\pi/4$ and a signal modulated on 8 equally spaced phases as in Fig. 1-C will require 3 DAFs as shown in Fig. 2-B to properly recover phase jumps with constant phase shifts of $\phi_1 = +\pi/4$, $\phi_2 = -\pi/4$ and $\phi_3 = -\pi/8$. After each DAFs, a single-ended (see Fig. 2-A) or balanced photodetector is used before the optional amplifier [5]. When several DAFs are needed, the incoming optical signal E_s has to be equally split into each of them. For PolMux signals, two identical detectors are needed after a

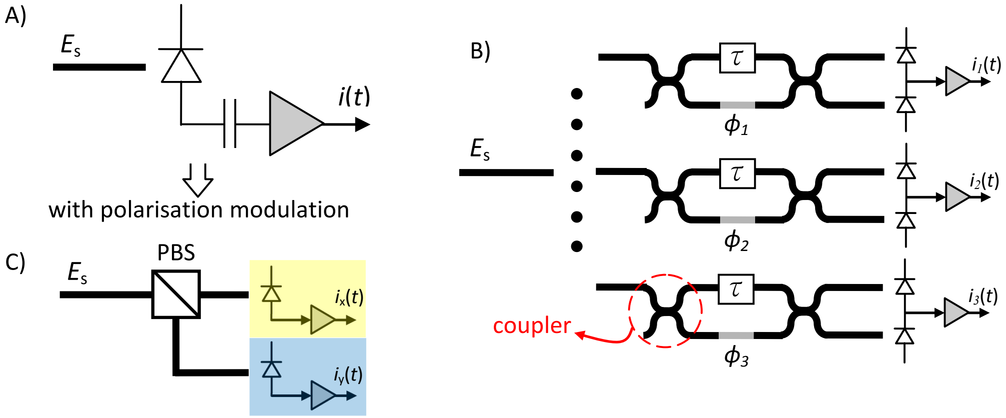

Fig. 2 - Amplitude (left) and Phase (right) detectors

Polarisation Beam Splitter (PBS), where each detector recovers the information on orthogonal polarisations. As an example, for an IM signal modulated on both polarisations, the detector would look in its simplest form like the one in Fig. 2-C, i.e., two replicas of a single DD detector for IM signals, preceded by a PBS.

2.1.2 – Coherent Receivers

The second type of receiver that is used in optical communications is the coherent receiver. A coherent receiver is used to recover the phase and amplitude of an incoming signal E_s using another signal E_{LO}. This second signal, E_{LO}, is utilized to downshift the central carrier frequency of E_s around which the information is modulated to a central frequency much closer to 0 Hz. In long-haul telecom the frequency of E_s lies in the vicinity of 194 THz. The down shifted frequency has to be within the bandwidth of the optical to electrical photodiodes in order for the latter to detect the signal. The amplitude and phase of E_s are recovered by digitally processing the received signals. In an optical system, the extra E_{LO} signal is a free running laser, called a local oscillator (LO). This LO has to have certain properties that we will detail later, but for now let's consider that E_{LO} has constant phase and amplitude and a frequency equal to that of E_s. By sending simultaneously the useful signal E_s and the local oscillator signal E_{LO} in a 90° optical hybrid as presented in Fig. 3, with $\phi_1 = 0$ and $\phi_2 = \pi/2$, we can extract two photocurrents corresponding to $i_1 \propto \mathrm{Re}\{E_S E_{LO}^*\}$ and $i_2 \propto \mathrm{Im}\{E_S E_{LO}^*\}$. Consequently, with a theoretical LO being a constantly rotating phasor, we exactly recover the real and imaginary part of E_s, therefore its complete complex value. We will see later on the impact on the recovery of E_s when LO has independent and varying phase with respect to E_s, and a slightly different frequency.

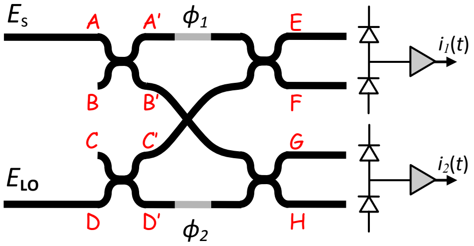

Fig. 3 – A 90° optical hybrid with 2 DC-coupled balanced photodetectors

The 90° optical hybrid used to mix the signal E_s with the LO is depicted above and is an all-optical passive device designed to specifically interact two optical signals together. They consist only of four couplers and some phase shifters. To be able to relate the outputs of the hybrid to its input, we have to look at the input-output relation of a single coupler, circled in Fig. 2-B, through its transfer matrix notation. The transfer matrix of a single 50-50 coupler is given by

$$\begin{bmatrix} A' \\ B' \end{bmatrix} = \frac{1}{\sqrt{2}} \begin{bmatrix} 1 & -j \\ -j & 1 \end{bmatrix} \begin{bmatrix} A \\ B \end{bmatrix} \tag{1}$$

where 50% of the incoming optical power goes to one branch and 50% goes to the other. Here A and B are the input E fields and A' and B' are the output fields. We can now relate the input A, B, C, D to the output A', B', C', D' of Fig. 3 with a 4x4 transfer matrix

$$\begin{bmatrix} A' \\ B' \\ C' \\ D' \end{bmatrix} = \frac{1}{\sqrt{2}} \begin{bmatrix} 1 & -j & 0 & 0 \\ -j & 1 & 0 & 0 \\ 0 & 0 & 1 & -j \\ 0 & 0 & -j & 1 \end{bmatrix} \begin{bmatrix} A \\ B \\ C \\ D \end{bmatrix} \tag{2}$$

This figure informs us that the second output B' goes down to the third output and conversely for the third output C'. Moreover we observe that the outputs A' and D' are respectively phase shifted by ϕ_1 and ϕ_2. Therefore, by doing the four transformations

$$\begin{aligned} A' &\rightarrow A' e^{j\phi_1} \\ B' &\rightarrow C' \\ C' &\rightarrow B' \\ D' &\rightarrow D' e^{j\phi_2} \end{aligned} \tag{3}$$

we obtain the transfer matrix of the 8-port 90° optical hybrid

$$\begin{aligned}\begin{bmatrix} E \\ F \\ G \\ H \end{bmatrix} &= \frac{1}{2}\begin{bmatrix} 1 & -j & 0 & 0 \\ -j & 1 & 0 & 0 \\ 0 & 0 & 1 & -j \\ 0 & 0 & -j & 1 \end{bmatrix}\begin{bmatrix} e^{j\phi_1} & 0 & 0 & 0 \\ 0 & 0 & 1 & 0 \\ 0 & 1 & 0 & 0 \\ 0 & 0 & 0 & e^{j\phi_2} \end{bmatrix}\begin{bmatrix} 1 & -j & 0 & 0 \\ -j & 1 & 0 & 0 \\ 0 & 0 & 1 & -j \\ 0 & 0 & -j & 1 \end{bmatrix}\begin{bmatrix} A \\ B \\ C \\ D \end{bmatrix} \\ &= \frac{1}{2}\begin{bmatrix} e^{j\phi_1} & -je^{j\phi_1} & -j & -1 \\ -je^{j\phi_1} & -e^{j\phi_1} & 1 & -j \\ -j & 1 & -e^{j\phi_2} & -je^{j\phi_2} \\ -1 & -j & -je^{j\phi_2} & e^{j\phi_2} \end{bmatrix}\begin{bmatrix} A \\ B \\ C \\ D \end{bmatrix}\end{aligned} \tag{4}$$

Now let us assume that input A is the useful signal E_S and input D is the local oscillator E_{LO} while there are no light shining on inputs B and C, so $A = E_S$, $B = 0$, $C = 0$ and $D = E_{LO}$. Let’s define the waveforms of E_S and E_{LO} as

$$\begin{aligned} E_S &= \sqrt{P_S(t)}e^{j\Phi_S(t)} \\ E_{LO} &= \sqrt{P_{LO}(t)}e^{j\Phi_{LO}(t)} \end{aligned} \tag{5}$$

where $P_S(t)$ and $\Phi_S(t)$ are respectively the power and the phase of the modulated signal and $P_{LO}(t)$ and $\Phi_{LO}(t)$ the power and phase of the local oscillator. We will use this notation to describe optical waveforms throughout this document for its simplicity and because it is a base reference in the literature [6]. As previously mentioned, if we set $\phi_1 = 0$ and $\phi_2 = \pi/2$, the optical power of the four outputs are

$$\begin{aligned} |E|^2 &= 1/4\left(P_S(t) + P_{LO}(t) - 2\,\mathrm{Re}\{E_S E_{LO}^*\}\right) \\ |F|^2 &= 1/4\left(P_S(t) + P_{LO}(t) + 2\,\mathrm{Re}\{E_S E_{LO}^*\}\right) \\ |G|^2 &= 1/4\left(P_S(t) + P_{LO}(t) + 2\,\mathrm{Im}\{E_S E_{LO}^*\}\right) \\ |H|^2 &= 1/4\left(P_S(t) + P_{LO}(t) - 2\,\mathrm{Im}\{E_S E_{LO}^*\}\right) \end{aligned} \tag{6}$$

where $E_S E_{LO}^* = \sqrt{P_S(t)P_{LO}(t)}e^{j(\Phi_S(t) - \Phi_{LO}(t))}$ and contains the useful information on E_S we want to recover at the receiver. In our notation, X^* is the complex conjugate of X. Looking at (6) we realize the tremendous potential for coherent receivers and the power of the 90° optical hybrid. If the receiver client knows all the parameters of its local oscillator signal E_{LO}, recovering $\mathrm{Re}\{E_S E_{LO}^*\}$ and $\mathrm{Im}\{E_S E_{LO}^*\}$ turns out to recovering $\mathrm{Re}\{E_S\}$ and $\mathrm{Im}\{E_S\}$, therefore obtaining all the information imprinted on E_S through any phase and/or amplitude modulation done at the transmitter. In comparison with direct-detectors presented in Fig. 2, the coherent receiver can do everything that the DD receivers can and more. Direct-detectors built for amplitude demodulation can only recover power changes and direct-detectors preceded by DAFs built for phase demodulation can only properly recover relative phase jumps. On the other hand, coherent receivers recover both the power and the actual phase as they give full access to the optical field E_s.

Looking at (6) we can understand the advantage of using balanced photodetectors to recover the real and imaginary part of $E_S E_{LO}^*$. Using a single photodetector after the outputs F and G, we recover photocurrents respectively proportional to $|F|^2$ and $|G|^2$ in (6). Single photodectors are normally immediately followed by a DC block (see Fig. 2-A) to get rid of constant photocurrents from the power of the local oscillator and possibly the signal. This action is called AC coupling. As mentioned in [7], in a receiver without a low-frequency cut-off, a DC offset sets an absolute minimum on the detectable signal, introduces pulse-width distortion into the signal, effectively decreasing the maximum symbol rate, and makes it difficult to implement high-gain post-amplification when needed. The latter arises because an amplified DC offset can shift certain signal states out of the linear region of operation of the amplifier. Alternatively to single-input photodetectors, balanced photodetectors as shown in Fig. 3 can be used. Balanced detectors have common mode rejection allowing two input electrical signals to be subtracted one another, resulting in removing the common components of said two signals. By launching $|E|^2$ and $|F|^2$ from (6) on a balanced photodetector and $|G|^2$ and $|H|^2$ on another, we get two photocurrents proportional to $1/4\left(4\,\mathrm{Re}\{E_S E_{LO}^*\}\right)$ and $1/4\left(4\,\mathrm{Im}\{E_S E_{LO}^*\}\right)$ respectively, where all the common terms $P_S(t) + P_{LO}(t)$ are removed. By subtracting, the magnitude of the output photocurrents are doubled, collecting $4\{E_S E_{LO}^*\}$ instead of $2\{E_S E_{LO}^*\}$. Therefore, the use of balanced photodetectors first rejects the need for DC blocks and second provides a significant gain of $10\log\left((4/2)^2\right) = 6$ dB on the electrical power of the collected signals. This 6-dB gain is of tremendous importance for improving the signal to noise ratio (SNR) at the receiver, a capital criterion to lower the mean bit error rate. This electrical gain can be enough not to have to use an electrical amplifier that inherently adds noise to the signal because of their non-zero noise figure. If an electrical amplifier is still needed, it will required less gain, where higher gains commonly bear a worst noise figure compared to low ones [8].

Balanced photodetectors can also be used in direct-detection phase demodulators as shown in Fig. 2-B for the same reason as for coherent receivers: no need to use a DC block and a gain of 6-dB on the electrical signal power [9].

The main difference between direct detectors and coherent receivers is the use of another laser, called the local oscillator, on the receiver side to mix with the incoming signal. For direct-detectors to properly recover polarization multiplexed signals, a polarisation controller followed by a polarisation beam splitter are needed. Polarisation beam splitters separate the incoming light onto two fixed orthogonal axis, that we can arbitrarily identify as $\hat{x}$ and $\hat{y}$. However, the polarisation of the signal arriving at the PBS is unknown and is changing in time in standard single mode fibres (SMF). This polarisation property of SMFs results in information cross-talk at the receiver. As an example, using the Jones matrix representation, for a signal arriving at polarisation θ with respect to the PBS's $\hat{x}$ axis the output on the $\hat{x}$ and $\hat{y}$ branches will be

$$\text{Output on } \hat{x}: \begin{bmatrix} 1 & 0 \\ 0 & 0 \end{bmatrix} \begin{bmatrix} \cos(\theta_t) & -\sin(\theta_t) \\ \sin(\theta_t) & \cos(\theta_t) \end{bmatrix} \begin{bmatrix} A_t^X \\ A_t^Y \end{bmatrix} = \hat{x}\left(A_t^X \cos(\theta_t) - A_t^Y \sin(\theta_t)\right) \quad (7)$$

$$\text{Output on } \hat{y}: \begin{bmatrix} 0 & 0 \\ 0 & 1 \end{bmatrix} \begin{bmatrix} \cos(\theta_t) & -\sin(\theta_t) \\ \sin(\theta_t) & \cos(\theta_t) \end{bmatrix} \begin{bmatrix} A_t^X \\ A_t^Y \end{bmatrix} = \hat{y}\left(A_t^Y \cos(\theta_t) + A_t^X \sin(\theta_t)\right) \quad (8)$$

where the first and second matrix in the middle part of Eq.(7) are respectively the linear $\hat{x}$ polarizer and the polarization rotator. Similarly, the output on $\hat{y}$ branch will be $\left(A_t^Y \cos(\theta_t) + A_t^X \sin(\theta_t)\right)$ when using a linear $\hat{y}$ polarizer. Here we assume that the X and Y signals arrive perfectly orthogonal: an assumption that is most of the time not true and that we will discuss later on. A_t^X and A_t^Y are the time varying complex signals modulated on the initial X and Y polarisations and θ_t is the time varying angle of the polarisation of the signal right before the PBS with respect to the PBS's principal axis $\hat{x}$. We can clearly see the polarisation cross-talk induced by varying polarisation θ_t. Therefore, a polarisation controller (PC) externally actuated would be needed to maintain θ_t at 0, allowing a proper demodulation of the PolMux signal. The block diagram of such receiver would look like the one in Fig. 2-C but with an actuated PC before the PBS. Tracking and actuating a polarisation controller is not easily implementable in practice and makes the receiver much bulkier and expensive. Polarisation diversity coherent receivers are exempt of this constraint.

2.1.3 – Polarisation Diversity Coherent Receivers

Polarisation-diversity coherent receivers offer an elegant solution to the problem of polarisation misalignment. Fig. 4 shows a block diagram of a polarisation-diversity coherent receiver. These devices consist of two 90° optical hybrids having inputs coming respectively from the $\hat{x}$ and $\hat{y}$ outputs of two identical polarisation maintaining splitters (PMS). The LO signal has to be aligned at 45° with the PMS's principal axis or polarized circularly in order to equally split its power into the two outputs. Fixing the LO polarization at 45° is readily done by using a fixed polarisation controller (PC) after the LO laser output, as the laser light is naturally polarized at a steady state [10]. We equally split the E_{LO} power to be able to keep track of polarisation dependant losses (PDL) on E_{S}. PDL is an important impairment on E_{S} when the signal is polarisation multiplexed. We will further detail the case of polarization multiplexed transmission but for now, we pursue studying the receiver with a signal having single polarisation.

As can be seen on Fig. 4, the top hybrid gives the in-phase (**I**) and quad-phase (**Q**) information of E_{S} when projected on the axis $\hat{x}$ of the PMS, namely $E_{\mathrm{S},\hat{x}}$, and the bottom hybrid gives the IQ information of E_{S} after its projection onto the PMS's $\hat{y}$ axis, namely $E_{\mathrm{S},\hat{y}}$. If the LO is not equally split in power, $|E_{\mathrm{LO},\hat{x}}| \neq |E_{\mathrm{LO},\hat{y}}|$ and all post equalization of $E_{\mathrm{S},\hat{x}}E^{*}_{\mathrm{LO},\hat{x}}$ with $E_{\mathrm{S},\hat{y}}E^{*}_{\mathrm{LO},\hat{y}}$ will be biased by the unequal magnitude of $E_{\mathrm{LO},\hat{x}}$ and $E_{\mathrm{LO},\hat{y}}$. For instance, in the particular case where the two states of polarisation of the signal E_S are aligned with $\hat{\mathrm{x}}$ and $\hat{\mathrm{y}}$ right before the PMSs, one would not differentiate a polarisation dependant loss on $E_{\mathrm{S},\hat{\mathrm{x}}}$ with respect to $E_{\mathrm{S},\hat{\mathrm{y}}}$ and a uneven separation of E_LO on $\hat{\mathrm{x}}$ and $\hat{\mathrm{y}}$.

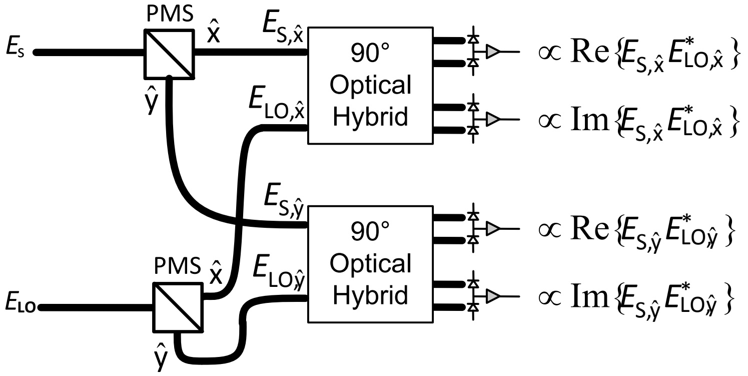

Fig. 4 – Dual Polarisation 90° Hybrid with 4 Balanced Photodetectors

Another advantage of the polarization diversity coherent receiver is its ability to recover all the information on the signal E_S , polarisation multiplexed or not, without any polarisation controller requiring feedback actuation. Direct-detectors cannot claim this property, as we explained earlier. One consequence of this property that no polarization actuation is required is that we initially don't know if what we receive in the $\hat{\mathrm{x}}$ and $\hat{\mathrm{y}}$ polarization are the signals on $\hat{X}_t$ and $\hat{Y}_t$. This characteristic is easily shown when we look at equation (7) and at the output signals on Fig. 4. Let's assume that E_S is not polarisation multiplexed and that its principal state of polarisation is at θ_t with respect to $\hat{\mathrm{x}}$ right before its PMS. The output at $\hat{\mathrm{x}}$ will be $E_{\mathrm{S},\hat{\mathrm{x}}} = E_\mathrm{S}\cos(\theta_t)$ and at $\hat{\mathrm{y}}$, $E_{\mathrm{S},\hat{\mathrm{y}}} = E_\mathrm{S}\sin(\theta_t)$ from Eqs. (7) and (8) by setting . $\mathrm{A}_t^\mathrm{Y} = 0$ and $\mathrm{A}_t^\mathrm{X} = E_\mathrm{S}$. If we would only use a single 90° optical hybrid, e.g. the top one, the signal $E_{\mathrm{S},\hat{\mathrm{y}}}$ would be lost and the recovered signal $E_{\mathrm{S},\hat{\mathrm{x}}}E^*_{\mathrm{LO},\hat{\mathrm{x}}}$ could sometimes equal zero and bear no information when $\theta_t = \pm 90°$. On the other hand, when two 90° optical hybrids are used as in a polarisation diversity coherent receiver, both $E_{\mathrm{S},\hat{\mathrm{x}}}$ and $E_{\mathrm{S},\hat{\mathrm{y}}}$ are used to recover E_S and there are no angle θ_t at which E_S is lost because the field is trigonometrically split among the top and bottom hybrids. Therefore, all the information on E_S is kept with this configuration.

This property is also true when E_{S} is polarisation multiplexed. To study this case, let's assume that the two polarisations on E_{S} are orthogonal before hitting the PBS and at an angle θ_t with respect to the PBS's $\hat{\mathrm{x}}$ axis. We define the waveform E_{S} in terms of its polarisations,

$$E_{\mathrm{S}} = E_{\mathrm{S}}^{\mathrm{X}}\hat{\mathrm{X}}_t + E_{\mathrm{S}}^{\mathrm{Y}}\hat{\mathrm{Y}}_t \tag{9}$$

It is important not to misinterpret $\hat{\mathrm{x}}$, $\hat{\mathrm{y}}$ with $\hat{\mathrm{X}}_t$, $\hat{\mathrm{Y}}_t$. Small letters $\hat{\mathrm{x}}$ and $\hat{\mathrm{y}}$ represent the orthogonal basis of the PBSs while $\hat{\mathrm{X}}_t$ and $\hat{\mathrm{Y}}_t$ represent the time varying states of polarisation of the polarisation multiplexed signal E_{S}. At the transmitter side, the X ($E_{\mathrm{S}}^{\mathrm{X}}$) and the Y ($E_{\mathrm{S}}^{\mathrm{Y}}$) signal are orthogonally modulated on $\hat{\mathrm{X}}_t$ and $\hat{\mathrm{Y}}_t$ respectively. As we know from single mode fibre, $\hat{\mathrm{X}}_t$ and $\hat{\mathrm{Y}}_t$ rotate as the field E_{S} propagates. Moreover, even if this is assumed in our current discussion, $\hat{\mathrm{X}}_t$ and $\hat{\mathrm{Y}}_t$ are not necessarily orthogonal: there can be a small deviation from 90° in the angle between $\hat{\mathrm{X}}_t$ and $\hat{\mathrm{Y}}_t$. As introduced in (7) and (8), the $\hat{\mathrm{x}}$ and $\hat{\mathrm{y}}$ outputs will respectively be

$$\begin{aligned} E_{\mathrm{S},\hat{\mathrm{x}}} &= E_{\mathrm{S}}^{\mathrm{X}}\cos(\theta_t) - E_{\mathrm{S}}^{\mathrm{Y}}\sin(\theta_t) \\ E_{\mathrm{S},\hat{\mathrm{y}}} &= E_{\mathrm{S}}^{\mathrm{Y}}\cos(\theta_t) + E_{\mathrm{S}}^{\mathrm{X}}\sin(\theta_t) \end{aligned} \tag{10}$$

Here we clearly see that $E_{\mathrm{S},\hat{\mathrm{x}}}$ will sometimes contain only the signal sent on X, sometimes only the signal sent on Y and most of the time a trigonometric mixture of X and Y signals. We can say the same for $E_{\mathrm{S},\hat{\mathrm{y}}}$ entering the bottom hybrid. From this point, using the hybrids outputs $E_{\mathrm{S},\hat{\mathrm{x}}}E_{\mathrm{LO},\hat{\mathrm{x}}}^{*}$ and $E_{\mathrm{S},\hat{\mathrm{y}}}E_{\mathrm{LO},\hat{\mathrm{y}}}^{*}$ and assuming that $\left|E_{\mathrm{LO},\hat{\mathrm{x}}}\right| = \left|E_{\mathrm{LO},\hat{\mathrm{y}}}\right|$, we can derive

$$\left|E_{\mathrm{S},\hat{\mathrm{x}}}E_{\mathrm{LO},\hat{\mathrm{x}}}^{*}\right|^2 + \left|E_{\mathrm{S},\hat{\mathrm{y}}}E_{\mathrm{LO},\hat{\mathrm{y}}}^{*}\right|^2 = P_{\mathrm{LO}}(t)\left(P_{\mathrm{S}}^{\mathrm{X}}(t) + P_{\mathrm{S}}^{\mathrm{Y}}(t)\right) \tag{11}$$

and find that the total electrical power from the polarisation diversity coherent receiver is independent of the entering angle θ_t and therefore, no signal power is lost using such receiver for both single polarisation and PolMux signals. We also show that no actuated polarisation controller is needed. However, post processing of $E_{\mathrm{S},\hat{\mathrm{x}}}$ and $E_{\mathrm{S},\hat{\mathrm{y}}}$ is required to keep track of rotations and to disentangle $E_{\mathrm{S}}^{\mathrm{X}}$ from $E_{\mathrm{S}}^{\mathrm{Y}}$.

Looking at Fig. 4, one could question the need for a PBS preceded by a PC simply for equalizing the LO power entering both hybrids. One could be interested in using two independent LO sources having the same power. There are two main reasons why the configuration in Fig. 4 is used. The first and most simple one is that good quality lasers are expensive and a single LO is sufficient in this application. The second reason, and the most important is found by looking at the phase relation of $E^*_{\mathrm{LO},\hat{x}}$ and $E^*_{\mathrm{LO},\hat{y}}$. Albeit their required equal magnitude, these two lightwaves naturally claim a common property after the PBS: they share the same waveform phase. This is of tremendous benefit for recovering $E_{\mathrm{s},\hat{x}}$ and $E_{\mathrm{s},\hat{y}}$ from the collected outputs $E_{\mathrm{S},\hat{x}}E^*_{\mathrm{LO},\hat{x}}$ and $E_{\mathrm{S},\hat{y}}E^*_{\mathrm{LO},\hat{y}}$ because it means that characterizing the complex waveform $E^*_{\mathrm{LO},\hat{x}}$ allowing the recovery of $E_{\mathrm{s},\hat{x}}$ disencumber at the same time $E_{\mathrm{s},\hat{y}}$ with no extra effort. If a certain processing power and time is required to disentangle $E_{\mathrm{S},\hat{x}}$ from $E_{\mathrm{S},\hat{x}}E^*_{\mathrm{LO},\hat{x}}$, the extra power and time are saved to find $E_{\mathrm{LO},\hat{y}}$ in $E_{\mathrm{S},\hat{y}}E^*_{\mathrm{LO},\hat{y}}$ when using a PC with PBS for the LO signal.

The observable quantities we collect are $E_{\mathrm{s},\hat{x}}$ and $E_{\mathrm{s},\hat{y}}$, projections of E_{S} on $\hat{x}$ and $\hat{y}$. Using a simple basis transformation shown below with the Jones matrix representation, we can retrieve the useful signals $E_{\mathrm{S}}^{\mathrm{X}}$ and $E_{\mathrm{S}}^{\mathrm{Y}}$ by applying the transfer matrix below to these observables.

$$\begin{bmatrix} E_{\mathrm{S}}^{\mathrm{X}} \\ E_{\mathrm{S}}^{\mathrm{Y}} \end{bmatrix} = \frac{1}{\cos(\Delta\theta_t)} \begin{bmatrix} \cos(\theta_t + \Delta\theta_t) & \sin(\theta_t + \Delta\theta_t) \\ -\sin(\theta_t) & \cos(\theta_t) \end{bmatrix} \begin{bmatrix} E_{\mathrm{S},\hat{x}} \\ E_{\mathrm{S},\hat{y}} \end{bmatrix} \tag{12}$$

$$\begin{bmatrix} E_{\mathrm{S},\hat{x}} \\ E_{\mathrm{S},\hat{y}} \end{bmatrix} = \begin{bmatrix} \cos(\theta_t) & -\sin(\theta_t + \Delta\theta_t) \\ \sin(\theta_t) & \cos(\theta_t + \Delta\theta_t) \end{bmatrix} \begin{bmatrix} E_{\mathrm{S}}^{\mathrm{X}} \\ E_{\mathrm{S}}^{\mathrm{Y}} \end{bmatrix} \tag{13}$$

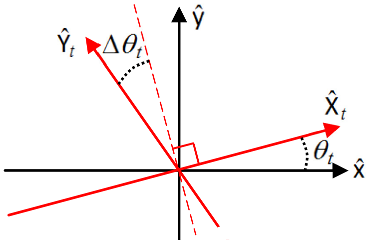

Fig. 5 – PBS axis (black) and E_s's principal state of polarisation axis (red)

The transfer matrix in (13) is the inverse of that in (12), allowing inverse basis switching from ($\hat{X}_t$, $\hat{Y}_t$) to ($\hat{x}$, $\hat{y}$). Basis transformations do not require any of the two bases to be orthonormal. The only property they both have to have is not to be a degenerate basis, i.e., where the constituting vectors point in the same direction. Although the information on E_S is imprinted on orthogonal axes at the transmitter, orthogonality is generally lost as the waveform propagates down the fibre due to impairments such as polarisation dependant loss [11, 12]. The difficult process to realize after this coherent receiver is to find the time varying angles θ_t and $\Delta\theta_t$ knowing only how $E_{s,\hat{x}}$ and $E_{s,\hat{y}}$ vary in time. Do to so, it is necessary to take advantage of the knowledge of the modulation format initially imprinted on E_s^X and E_s^Y to properly recover the useful information with a blind recovery approach. For instance, if we know that both E_s^X and E_s^Y signals that are phase modulated only, we can assume that the desired signals at the receiver have constant amplitude and derive E_s^X and E_s^Y from $E_{s,\hat{x}}$ and $E_{s,\hat{y}}$. We will detail later a way for such signal derotation.

2.2 – Modelling the lasers

We introduced in equation (5) the signal and the local oscillator's waveforms as complex numbers having an amplitude and an undefined phase. In this section we will detail how we model the lasers waveforms. It will provide a framework for future analysis and define how to recover the useful information on E_S.

We know from the theory of electromagnetism that light is a form of electromagnetic radiation and therefore can be represented by either its electric or magnetic field. The Poynting theorem [13] tells us that the power of a wave is proportional to the product of the amplitude of the electric and magnetic fields, which implies that these amplitudes are proportional to the square root of the power. Hence, we represent waveforms with amplitude in a square root of power form.

The phase of the waveform has to take into account all the properties of a laser beam. First of all, a lightwave oscillates at very high frequencies. In the telecommunication window of interest, signals have center frequencies in the vicinity of $f_o = 194$ THz. A lightwave is said to be monochromatic if a single frequency is coming out of the laser source. However, this concept is theoretical as no lasers can emit only a single wavelength due to the natural spontaneous emission of light from quantum origins. If we were to obtain a single tone laser, we would write its complex part as $e^{i(\omega_o t+\phi_o)}$ where $\omega_o = 2\pi f_o$, f_o would be a fix frequency at 194 THz and the relative phase of the waveform ϕ_o would also be fixed at an arbitrary value between 0 and 2π. For real lightwaves, however, the relative phase is not fixed but varies in time according to a Gaussian random process [14-16]. This time varying phase $\phi(t)$ is a stochastic process representing angular fluctuation in time. Frequency shifts are also taken into account in $\phi(t)$ as the instantaneous frequency is by definition the time derivative of the angle. This stationary Gaussian random process is assumed to have a time derivative that is zero-mean, so on average, the frequency deviation from f_o is zero. Taking into account this phase noise, the complex part of a waveform can be written as $e^{i(\omega_o t+\phi(t)+\phi_o)}$ and therefore the instantaneous frequency is $f(t) = f_o + (2\pi)^{-1} d\phi(t)/dt$. It is this time varying frequency in the last part of this equation that leads to the broadening of the single tone spectral line centered at f_o. Broadening of the emission frequency is an inevitable consequence of the spontaneous decay of population from excited levels: a more classical explanation. It has been shown in the literature that the shape of the emission linewidth is either Lorentzian or Gaussian [17]. This power spectral density shape has therefore a Full Width at Half Maximum (FWHM) varying from tens of kilohertz to tens of megahertz, depending on a multitude of factors like electron decay rate, temperature, average mass of atoms in lasing media and the structure of the laser cavity [14].

Laser phase noise $\phi(t)$ is known to be a random phase walk generated by the Weiner process. Random walks, or Brownian motions, are well known processes and it is not of our interest to explain them thoroughly. The laser phase noise process is commonly characterized by a Weiner process such that $\phi(t) \triangleq \int_0^t \phi'(\tau)d\tau$ [18], with $\phi(0)=0$, where its time derivative $\phi'(t)$ is a zero-mean white Gaussian process with a flat power spectral density of $2\pi\Delta v$, where Δv is the 3 dB laser linewidth in Hz. The randomly walking phase $\phi(t)$ then becomes a Gaussian random variable with variance $2\pi\Delta v\cdot t$. It is well know that for a Gaussian random variable Φ of mean R and variance σ^2, $\Phi \sim N(R,\sigma^2)$, the expected value of $e^{j\Phi}$ is

$$E\left[e^{j\Phi}\right]=\frac{1}{\sqrt{2\pi\sigma^2}}\int_{-\infty}^{\infty} e^{j\Phi}\cdot e^{\frac{-(\Phi-R)^2}{2\sigma^2}}\,d\Phi=e^{\frac{-\sigma^2}{2}+jR} \tag{14}$$

In our case, $\phi(t)$ has $\sigma^2=2\pi\Delta v\cdot|t|$. For further details on laser phase noise, we refer the reader to [18].

We are now in a position to expand the mathematical expressions of the signals collected after the polarisation diversity coherent receiver, i.e., of $E_{\mathrm{S},\hat{\mathrm{x}}}E^{*}_{\mathrm{LO},\hat{\mathrm{x}}}$ and $E_{\mathrm{S},\hat{\mathrm{y}}}E^{*}_{\mathrm{LO},\hat{\mathrm{y}}}$. Let's start by redescribing E_{S} in light of the waveform framework mentioned above and assuming a modulation in amplitude, phase and polarisation.

$$\begin{aligned} E_{\mathrm{S}} &= E_{\mathrm{S}}^{\mathrm{X}}\,\hat{\mathrm{X}}_t + E_{\mathrm{S}}^{\mathrm{Y}}\,\hat{\mathrm{Y}}_t \\ E_{\mathrm{S}} &= \sqrt{P_{\mathrm{S}}^{\mathrm{X}}(t)}e^{j\left(\omega_{\mathrm{S}}t+\phi_{\mathrm{S}}(t)+\Phi_{\mathrm{S}}^{\mathrm{X}}(t)+\phi_{o,\mathrm{s},\hat{\mathrm{X}}}\right)}\,\hat{\mathrm{X}}_t + \sqrt{P_{\mathrm{S}}^{\mathrm{Y}}(t)}e^{j\left(\omega_{\mathrm{S}}t+\phi_{\mathrm{S}}(t)+\Phi_{\mathrm{S}}^{\mathrm{Y}}(t)+\phi_{o,\mathrm{s},\hat{\mathrm{Y}}}\right)}\,\hat{\mathrm{Y}}_t \end{aligned} \tag{15}$$

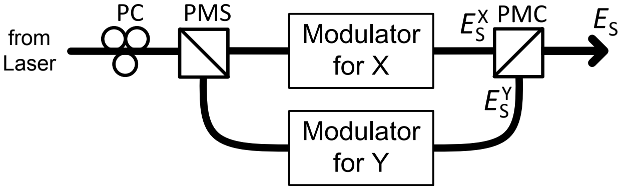

Fig. 6 – Simple representation of a dual polarisation transmitter

For similar reasons as previously mentioned about using a single or two LO lasers at the receiver, a single transmitter laser for polarisation multiplexed signals is used and split in polarisation. Each orthogonally polarised light is independently modulated in amplitude and/or phase before recombined with a Polarisation Maintaining Combiner (PMC). A PMS is used between the laser and the two modulator inputs. The three ports of the PMS are polarization maintaining fibres and are aligned on the slow axis. With the laser also aligned on the slow axis, we make sure that the power is equally split. Since the $E_{\mathrm{s}}^{\mathrm{X}}$ and $E_{\mathrm{s}}^{\mathrm{Y}}$ signals come from the same laser, they are characterized by the same central angular frequency ω_s and laser phase noise $\phi_\mathrm{s}(t)$. Each polarisation waveform has its own time-dependant phase modulation $\Phi_\mathrm{S}^\mathrm{X}(t)$ and $\Phi_\mathrm{S}^\mathrm{Y}(t)$ and its own time-varying amplitude $\sqrt{P_\mathrm{s}^\mathrm{X}(t)}$ and $\sqrt{P_\mathrm{s}^\mathrm{Y}(t)}$ from their respective phase and amplitude modulation. Finally, each polarisation waveform can have its own relative phase, identified as $\phi_{o,\mathrm{s},\hat{\mathrm{x}}}$ and $\phi_{o,\mathrm{s},\hat{\mathrm{y}}}$, imprinted by the components the X and Y signals traverse. Examples of such components are the PMS that can have a reflectance and transmittance coefficients with different phase response for TM and TE polarisations [19], or the two modulators having a different residual phase shift from their electrical driving signals.

We can also redescribe the local oscillator signal at the receiver after it passes through its PBS (see Fig. 4) as

$$\begin{aligned} E_\mathrm{LO} &= E_{\mathrm{LO},\hat{\mathrm{x}}}\,\hat{\mathrm{x}} + E_{\mathrm{LO},\hat{\mathrm{y}}}\,\hat{\mathrm{y}} \\ E_\mathrm{LO} &= \sqrt{P_{\mathrm{LO},\hat{\mathrm{x}}}(t)}e^{j\left(\omega_\mathrm{LO}t+\phi_\mathrm{LO}(t)+\phi_{o,\mathrm{LO},\hat{\mathrm{x}}}\right)}\,\hat{\mathrm{x}} + \sqrt{P_{\mathrm{LO},\hat{\mathrm{y}}}(t)}e^{j\left(\omega_\mathrm{LO}t+\phi_\mathrm{LO}(t)+\phi_{o,\mathrm{LO},\hat{\mathrm{y}}}\right)}\,\hat{\mathrm{y}} \end{aligned} \tag{16}$$

where ω_LO and $\phi_\mathrm{LO}(t)$ are the central angular frequency and the phase noise of the LO signal, and $\phi_{o,\mathrm{LO},\hat{\mathrm{x}}}$ and $\phi_{o,\mathrm{LO},\hat{\mathrm{y}}}$ are constant phase differences that we leave independent for the same reasons mentioned above. Ideally, the polarisation of the LO before the PBS is such that $P_{\mathrm{LO},\hat{\mathrm{x}}}(t) = P_{\mathrm{LO},\hat{\mathrm{y}}}(t)$ as previously mentioned. From this point, we can easily describe the signals we would collect if the signal alignment right before its PBS is such that $\hat{\mathrm{X}}_t = \hat{\mathrm{x}}$ and $\hat{\mathrm{Y}}_t = \hat{\mathrm{y}}$.

$$\begin{aligned} E_\mathrm{S}^\mathrm{X}E_{\mathrm{LO},\hat{\mathrm{x}}}^* &= \sqrt{P_\mathrm{S}^\mathrm{X}(t)P_{\mathrm{LO},\hat{\mathrm{x}}}(t)}e^{j\left(\omega_\mathrm{IF}t+\phi_\mathrm{IF}(t)+\Phi_\mathrm{S}^\mathrm{X}(t)+\phi_{o,\mathrm{S},\mathrm{X}_t}-\phi_{o,\mathrm{LO},\hat{\mathrm{x}}}\right)} \\ E_\mathrm{S}^\mathrm{Y}E_{\mathrm{LO},\hat{\mathrm{y}}}^* &= \sqrt{P_\mathrm{S}^\mathrm{Y}(t)P_{\mathrm{LO},\hat{\mathrm{y}}}(t)}e^{j\left(\omega_\mathrm{IF}t+\phi_\mathrm{IF}(t)+\Phi_\mathrm{S}^\mathrm{Y}(t)+\phi_{o,\mathrm{S},\mathrm{Y}_t}-\phi_{o,\mathrm{LO},\hat{\mathrm{y}}}\right)} \end{aligned} \tag{17}$$

where we define the new variables ω_IF, $\phi_\mathrm{IF}(t)$, $\phi_{o,\hat{\mathrm{x}}}$ and $\phi_{o,\hat{\mathrm{y}}}$. The difference in the angular frequencies of the LO and the useful signal E_S is replaced by ω_IF, which we call the intermediate frequency (IF), and is defined as $\omega_\mathrm{IF} = \omega_\mathrm{S} - \omega_\mathrm{LO}$. The difference in the phase noise of the two lasers is represented by the variable $\phi_\mathrm{IF}(t) = \phi_\mathrm{S}(t) - \phi_\mathrm{LO}(t)$. We know from previous study that the electrical power spectal density (PSD) of photocurrents after a photodiode located on one output port of an optical directional coupler with impinging light sources having Lorentzian line shapes also shows a Lorentzian shape with a full width at half maximum (FWHM) being the sum of the FWHM of the two ingress signals [18, 20-23]. In other words, since the transmitter and the local oscillator lasers have statistically independent phase noise processes, the resulting linewidth is the sum of the individual laser linewidths. Finally, a constant phase difference between the signal and the LO is taken into account in the last two arguments in (17).

What we define in (17) are not assuredly the signals we collect, as only rarely the principal states of polarisation (PSP) of E_S match those of the PBS. With the help of Eq. (13) to (16) and of Fig. 5, we can derive $E_{\mathrm{S},\hat{\mathrm{x}}}E^*_{\mathrm{LO},\hat{\mathrm{x}}}$ and $E_{\mathrm{S},\hat{\mathrm{y}}}E^*_{\mathrm{LO},\hat{\mathrm{y}}}$ with misalignments $\theta_t \neq 0$ and $\Delta\theta_t \neq 0$,

$$\begin{aligned} E_{\mathrm{S},\hat{\mathrm{x}}}E^*_{\mathrm{LO},\hat{\mathrm{x}}} = \sqrt{P_{\mathrm{LO},\hat{\mathrm{x}}}(t)}[\cos(\theta_t)\sqrt{\alpha_\mathrm{X} P^\mathrm{X}_\mathrm{S}(t)}e^{j(\omega_\mathrm{IF}t+\phi_\mathrm{IF}(t)+\Phi^\mathrm{X}_\mathrm{S}(t)+\phi_{o,\mathrm{S},\hat{\mathrm{X}}_t}-\phi_{o,\mathrm{LO},\hat{\mathrm{x}}})} \\ -\sin(\theta_t+\Delta\theta_t)\sqrt{\alpha_\mathrm{Y} P^\mathrm{Y}_\mathrm{S}(t)}e^{j(\omega_\mathrm{IF}t+\phi_\mathrm{IF}(t)+\Phi^\mathrm{Y}_\mathrm{S}(t)+\phi_{o,\mathrm{S},\hat{\mathrm{Y}}_t}-\phi_{o,\mathrm{LO},\hat{\mathrm{x}}})}] \end{aligned} \tag{18}$$

$$\begin{aligned} E_{\mathrm{S},\hat{\mathrm{y}}}E^*_{\mathrm{LO},\hat{\mathrm{y}}} = \sqrt{P_{\mathrm{LO},\hat{\mathrm{y}}}(t)}[\sin(\theta_t)\sqrt{\alpha_\mathrm{X} P^\mathrm{X}_\mathrm{S}(t)}e^{j(\omega_\mathrm{IF}t+\phi_\mathrm{IF}(t)+\Phi^\mathrm{X}_\mathrm{S}(t)+\phi_{o,\mathrm{S},\hat{\mathrm{X}}_t}-\phi_{o,\mathrm{LO},\hat{\mathrm{y}}})} \\ +\cos(\theta_t+\Delta\theta_t)\sqrt{\alpha_\mathrm{Y} P^\mathrm{Y}_\mathrm{S}(t)}e^{j(\omega_\mathrm{IF}t+\phi_\mathrm{IF}(t)+\Phi^\mathrm{Y}_\mathrm{S}(t)+\phi_{o,\mathrm{S},\hat{\mathrm{Y}}_t}-\phi_{o,\mathrm{LO},\hat{\mathrm{y}}})}] \end{aligned} \tag{19}$$

To properly recover E^X_s and E^Y_s, post processing of Eq. (18) and (19) should remove the intermediate frequency ω_IF, the sum of the transmitter and LO laser phase noise $\phi_\mathrm{IF}(t)$, all the dummy constant phase shifts, polarisation rotations θ_t and polarization unorthogonality $\Delta\theta_t$. Polarization dependant loss (PDL) is added in Eqs. (18) and (19) through α_X and α_Y and is also an impairment that will have to be removed. As PDL is the extra loss of power on one polarization with respect to the other, we set the attenuation coefficient of the highest signal power to zero, for instance $\alpha_\mathrm{X} = 0$ if $P^\mathrm{X}_\mathrm{S}(t) > P^\mathrm{Y}_\mathrm{S}(t)$ and set the other PDL attenuation coefficient to $\alpha_\mathrm{Y} = P^\mathrm{Y}_\mathrm{S}(t)/P^\mathrm{X}_\mathrm{S}(t)$.

2.3 – *Criteria for Proper Demodulation*

The four electrical signals that come out of the polarisation diversity coherent receiver are the real and imaginary parts of equations (18) and (19). These signals have a bandwidth that is function of the intermediate frequency ω_{IF} and of the symbol rate imprinted in the amplitude and/or phase of E_{S}. It is known from the Nyquist sampling theorem [24, 25] that every signal of finite energy and bandwidth W Hz may be completely recovered from the knowledge of its samples taken at the rate of 2W per second. This sampling theorem serves as basis for the interchangeability of analog signals and digital sequences. The corollary of this sampling theorem is that if the electronic sampling speed of the receiver is capped at a finite rate of S samples per seconds, the bandwidth of the signal has to be lower than S/2 Hz.

Therefore, to completely recover the signals $E_{\mathrm{S},\hat{x}}E^*_{\mathrm{LO},\hat{x}}$ and $E_{\mathrm{S},\hat{y}}E^*_{\mathrm{LO},\hat{y}}$ out of the polarisation diversity coherent receiver, the first criterion on the analog bandwidth of the analog to digital converters (ADC) is to be greater or equal to half their sampling rate. The following figure shows a global view of the complete conversion scheme from optical to analog electrical to digital signals.

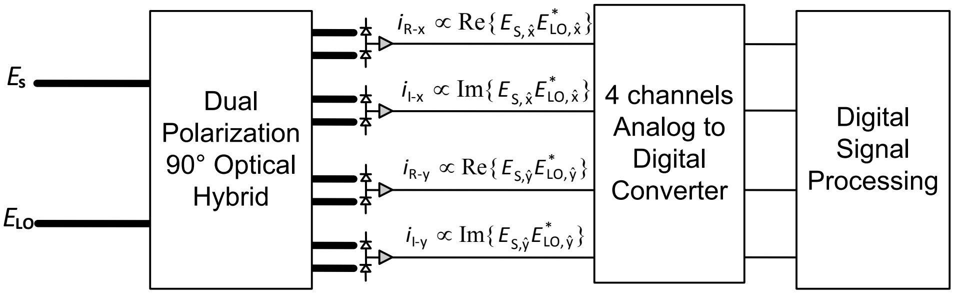

Fig. 7 – Complete block diagram of a coherent receiver with post DSP

The optical signals E_{S} and E_{LO} get converted to electrical signals after the dual polarisation 90° optical hybrid with the help of four balanced photodetectors. The four analog electrical currents get sampled by ADCs before being post processed by digital signal processing means. ADCs not only have a finite sampling rate, they also show a frequency response as they employ CMOS with inherent frequency characteristics. Consequently, a second criterion on the bandwidth of the ADC is to be at least that of the maximum bandwidth of the ingress signals to avoid signal impairments by the ADC. Normally, when the second condition of ADCs' 3-dB bandwidth is met for an ingress signal, the first condition on minimum sampling rate is satisfied, as ADCs producers normally honour the Nyquist sampling criterion with respect to the device's own maximum bandwidth. For fixed 3-dB bandwidth and a fixed sampling rate of the ADCs, the collected signals $E_{S,\hat{x}}E^*_{LO,\hat{x}}$ and $E_{S,\hat{y}}E^*_{LO,\hat{y}}$ have to have frequency components as depicted in the following figure:

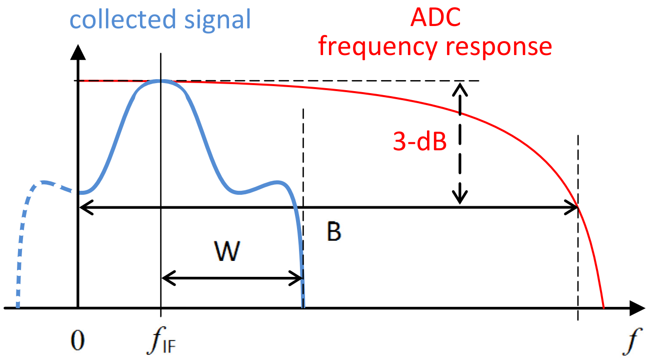

Fig. 8 – Frequency representation of collected signals and samplingh ADCs

Here, the bandwidth $W + f_{IF}$ Hz is the total bandwidth of $E_{S,\hat{x}}E^*_{LO,\hat{x}}$ and $E_{S,\hat{y}}E^*_{LO,\hat{y}}$. This means that W includes any modulation formats imprinted on E_S plus the sum of the transmitter and local oscillator lasers' phase noise. In other words, W is the bandwidth of the power spectral density of equations (18) and (19) when $\omega_{IF} = 0$. On the other hand, B is the ADCs 3-dB bandwidth. On this figure we clearly see the two requirements for ACDs, i.e., that $W + f_{IF} \leq B$ and that the sampling rate be greater than $2(W + f_{IF})$ samples per seconds.

We differentiate three types of coherent detections based on the location of the intermediate frequency f_{IF} with respect to the bandwidth of the baseband signal W. Before to start, it is useful to distinguish synchronous and asynchronous demodulation. Synchronous demodulation is in fact also called homodyne reception and it is achieved when the local oscillator that is mixed with the incoming signal has exactly the same frequency and phase as of the signal itself. This is realized using an external Phase Locked Loop (PLL) that adjusts the frequency and phase of LO to track those of the signal. Synchronous demodulation is readily done for electrical signals and LOs, but gets quite elaborated for optical signals. A synchronous demodulation would result in forcing $\omega_{\text{IF}} = 0$, $\phi_{\text{IF}}(t) = 0$ and all the constant phases to zero in (18) and (19), in which case LO cancels the slow varying arguments of the signal, leaving only the rapidly changing phase modulation.

Asynchronous demodulation can be separated in two subcategories, namely asynchronous intradyne and asynchronous heterodyne. Asynchronous demodulation mean that the LO's frequency and phase is not locked to that of the ingress signal and is free running. The simplicity of asynchronous demodulation over synchronous is what makes it so attractive for optical systems using a coherent receiver. By definition, intradyne demodulation is observed when the intermediate frequency f_{IF} is smaller than the signal's bandwidth W. When this happens, there is some spectral content overlapping on the frequency down shifted signal. Fig. 8 shows a good example of intradyne reception where some frequency content normally laying in the positive side spill over in the negative side. Finally, heterodyne reception happens when f_{IF} is bigger than W. In this scenario, there is no spectral content overlapping [26].

For a coherent detection system with asynchronous demodulation using ADCs having a finite bandwidth, it is most preferable to work in the intradyne regime with an intermediate frequency laying as close to zero as possible. In this case, no complex optical PLL is required and signals with large bandwidth W, as large as the ADC's, can be demodulated.

2.3.1 – Laser Criteria as a Function of the Modulation Format and Speed

What we presented above are criteria about the required sampling rate and bandwidth of the ADC to properly demodulate a signal who's frequency is downshifted at f_{IF} and with a bandwidth of W. The major part of the bandwidth W of said signal, described in (18) and (19), comes from the modulation format and the modulation rate imprinted on the transmitter laser. With today's optical transmission rate in the gigasamples per second, only a small fraction the total received bandwidth is due to the transmitter and local oscillator laser's phase noise.

There is another criterion concerning the LO's frequency compared to the signal's when phase modulation is employed. To explain this, let's take an example where the signal is modulated in 8-PSK, as depicted in Fig. 1-C, and where the symbol rate is 20 Gsymbol/s, meaning a symbol duration of 50 ps. This means that every 50 ps, the phase of the lightwave can jump by $n \cdot \pi/4$, where $n \in \{0,...,7\}$. At one sample per symbol the minimum sampling rate is 20 Gsamples/s. The effect of f_{IF} on the 8-PSK signal is a rotation of the signal constellation (Fig. 1-C) by f_{IF} complete rotations per second. Before pursuing, we should mention that any receiver has a slicer that associates received samples to the closest symbol in the constellation. In the 8-PSK case, eight phase-intervals are defined, each of which being $2\pi/8$ wide. Now we imagine that a symbol is perfectly sampled at $(1 + i \cdot 0)$ in the constellation and that the next symbol sent is the same. As our received symbol has a phase within $[-\pi/8, \pi/8]$ and is properly mapped in the constellation. We find that to properly distinguish a $2\pi/8$ phase jumps to a simple rotation due to the frequency offset f_{IF}, the intermediate frequency has to be such that the constellation rotates by less than $\pi/8$ in 50 ps, giving an extra criterion on $f_{\mathrm{IF}} \leq (\pi/8)/(2\pi)/50\,\mathrm{ps} = 1.25\,\mathrm{GHz}$ for this specific case of 8-PSK at 20 Gsymbols/s. Consequently, even if the bandwidth B and the sampling rate of the ADC are satisfied for the incoming signal of bandwidth $\mathrm{W} + f_{\mathrm{IF}}$, the LO's laser frequency as to be tuned within a certain bandwidth around the transmit laser's frequency. Generally speaking, this constraint applies whenever the signal is modulated in phase, and when it is the case, this criteria is the most constraining. On the other hand, when only amplitude modulation is employed as in Fig. 1-B, this extra constraint on f_{IF} is absent and f_{IF} can take any value from 0 to $\mathrm{B} - \mathrm{W}$.

Chapter 3 : Algorithms for signal recovery

In this chapter, we will talk about the required digital signal processing to recover the information sent on optical links. We will mainly introduce digital ways to remove impairments on the signal due to the transmission channel itself, i.e., the optical fibre, and due to the type of receiver employed, i.e., the coherent receiver. We will talk about ways to compensate for the fibre dispersion, how to remove the frequency offset between the signal E_{S} and the local oscillator E_{LO}, how to suppress the transmitter and LO phase noise and we will present a method to remove the polarisation cross-talk on the signal. Before beginning to describe the digital processings, we will discuss the effects of sampling at the minimal Nyquist rate and oversampling.

3.1 – Nyquist Sampling and Oversampling

As previously mentioned, the Nyquist-Shannon sampling theorem says that an analog signal having a maximum frequency of $\mathrm{Fs}/2$ Hz is fully represented in the digital domain if sampled at a rate of Fs samples/s. We could then ask our self what would be the benefits of sampling this analog signal at a rate higher then Fs. There are in fact many reasons to sample at a higher rate than the minimal predicted by Nyquist.

The very first reason is the increase of ADC resolution when oversampling is used. Indeed, it can be proven that sampling at N times the minimal rate followed by proper filtering of the digital signal and decimating by $1/\mathrm{N}$ gives a digitized signal that has a higher signal to quantization noise ratio ($\mathrm{SNR_Q}$) that can be translated to an increased bit resolution of the ADC. Actually, the ADC resolution is increased by $(0.602)^{-1}\log\left(\mathrm{F_{OS}}/\mathrm{F_{NS}}\right)$ bits when oversampling is done, where $\mathrm{F_{NS}}$

is the Nysquist sampling rate and F_{OS} is the oversampling rate [27, 28]. Therefore, a fourfold oversampling increases the SNR_Q by 6.02 dB and acts as if the ADC had an extra bit of resolution.

Processing or filtering a signal oversampled by an integer factor is called in digital communications a Fractionally Spaced Equalization (FSE) or a T/N-spaced equalizer, where T is the symbol duration and N is the oversampling factor. Filtering a digital signal sampled at Nyquist is called Synchronous Equalization or T-spaced equalization. A FSE has the capability of compensating for delay distortions more effectively than a conventional synchronous equalizer [29]. Another advantage of the FSE is the fact that data sampling may begin with an arbitrary sampling phase, compared to an equalizer working with T-spaced data that requires the sampler to sample right in the middle of the symbol duration, where the eye is the most open. We can easily visualize this sampler criterion for T-spaced sampling by imagining a pure sinusoidal signal of frequency f being sampled once every $1/(2f)$ seconds but exactly at the nulls. No information is recovered on the digitized signal even if sampling is at Nyquist, hence the name Synchronous Equalization for the need for phase synchronization of the sampler with respect to the incoming signal. However, the signal frequency f can be recovered with any phase when sampling is happening once every $1/2Nf$ seconds for $N > 1$. Moreover, in can be proven FSE have a minimum mean square error that is independent of the sampling epoch [30].

A last argument in favour of oversampling at an integer multiple of the Nyquist rate is understood by looking at the frequency response of digital filters. Digital post-processing of the acquired signal will be done using digital transversal filters. These filters take previous samples to process a current sample and output a filtered sample that can be utilized again for the filtering of the next sample. Such finite length filters have a separate magnitude and phase response and one cannot set both of them independently, i.e., a filter designed to have a desired magnitude response will inherently engender a phase response that is in most cases not desired, and vice versa for a filter designed for a specific phase-response. In most cases phase shifts is null at DC and monotonically increase with frequency. This results in more phase shift received by frequency components further away from DC, or in other words closest to the maximal frequency represented: half the sampling rate. If the signal is sampled at Nyquist, $f_s/2=f_{max}$, the high frequency content of the signal will receive a maximum amount of phase shift engendered by the T-spaced filter. However, if the signal is N-times oversampled, $f_s/2=Nf_{max}$. The equivalent T/N-spaced filter will have the same phase response, but now applied only from DC to $f_s/(2N)$, and undesired the phase shifts around $f_s/(2N)$ will be less than those around $f_s/2$.

In our processings, we will work with signals sampled at the Nyquist rate. We will see in a later section that this rate is equivalent to 2 samples per symbol duration, due to the type of pulse used. We work with such a type of pulse to benefit from the T/2 oversampling, and to be realistic with the finite sampling speed of ADCs. Of course, system performance would increase by sampling at 4 or 8 times the baud rate, but we limit ourselves to the minimum integer oversampling rate that is beneficial.

3.2 – Required Signal Processing

In this section we will lay the required digital processing to be done in the "Digital Signal Processing" box of Fig. 7. This section is not intended to provide ways to implement each processing numerically. We rather explain the origin of the impairments and mathematical methods to suppress or mitigate them. We will mention what operations ought to be applied to the 4 signals coming from the ADCs in order to recover the binary information sent. These operations arise from our knowledge of: 1) the shape of the signal sent, 2) the characteristics of the transmission channel, and 3) the type of receiver used. For certain processings that are modulation format sensitive, we will assume DP-QPSK, a modulation on 4 phases sent independently on two orthogonal polarisations. We will present the processing in the sequence they have to be applied to properly recover the information. The following figure shows the required operations to apply digitally when a coherent receiver is used. Some of these operations can be regrouped and be done simultaneously. We will discuss later on the different outcomes in the latter case.

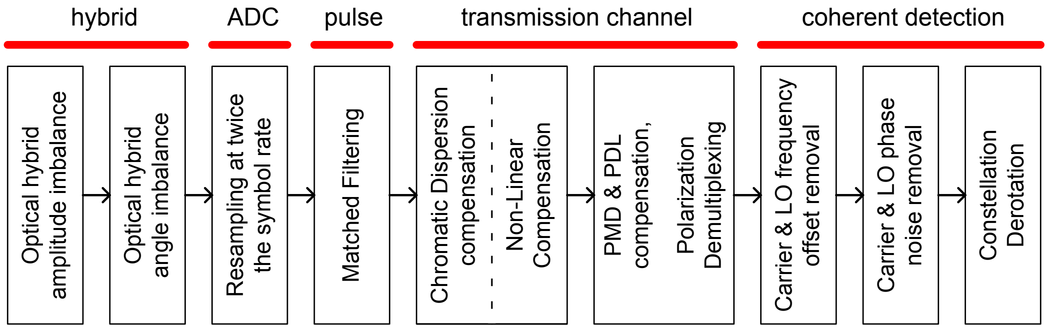

Fig. 9 – Sequence of Digital Signal Processings for Coherent Receivers

3.2.1 – Optical Hybrid Amplitude Imbalance

The very first process to apply to the four numerical signals is to remove any DC offset from the real and imaginary parts of both collected polarisations. By looking at Fig. 3 and Fig. 4, we realize that there could be an impact if the four directional couplers in each 90° optical hybrids are not perfect 50 % - 50 % couplers. Our simplified study in equation (4) detailing the outputs of each hybrids would then become more complicated if each coupler is assumed to have its own power transfer coefficient α different than $1/2$. We can study the effect of imperfect couplers for two cases. In the first case, let's assume that the four couplers are identical, but with $\alpha \neq 1/2$. It can be proven that the output electrical signals, after balanced photodetection, are described by

$$\begin{aligned} i_1 &\propto (1-\alpha)(2\alpha-1)\cdot P_S(t) - \alpha(2\alpha-1)\cdot P_{LO}(t) + 4\alpha(1-\alpha)\,\mathrm{Re}\{E_S E_{LO}^*\} \\ i_2 &\propto -\alpha(2\alpha-1)\cdot P_S(t) + (1-\alpha)(2\alpha-1)\cdot P_{LO}(t) + 4\alpha(1-\alpha)\,\mathrm{Im}\{E_S E_{LO}^*\} \end{aligned} \tag{20}$$

In this case, the amplitude of Re and Im of $\{E_S E_{LO}^*\}$ are the same. We are only interested in the last term in the previous equations and the different DC terms with $P_S(t)$ and $P_{LO}(t)$ on the left hand side are irrelevant and need to be removed.

We say that these terms are DC because for QPSK signals $P_{\mathrm{S}}(t)$ is theoretically constant and so is $P_{\mathrm{LO}}(t)$.

We subtract the DC sources by removing the mean value of each of the four acquired signals $V_{\text{R-x}}$, $V_{\text{I-x}}$, $V_{\text{R-y}}$ and $V_{\text{I-y}}$, referring to Fig. 7. We now speak in terms of voltages as the currents are converted into voltages right before the ADCs based on Ohm's Law, $V = \Re \cdot i$, with $\Re = 50$ Ohm resistors. For instance, the term $V_{\text{R-x}}$ is obtained from the uppermost output current $i_{\text{R-x}}$ in Fig. 7. With the means of $V_{\text{R-x}}$, $V_{\text{I-x}}$, $V_{\text{R-y}}$ and $V_{\text{I-y}}$ at zero, we now have to set their variance to be the same respectively for each polarization, and here comes the second case study.

Let's assume that the first two couplers to the left of the 90° optical hybrid on Fig. 3 are not identical anymore but have power transfer coefficients of α and β. These couplers' transfer matrix would then be

$$\begin{bmatrix} \sqrt{1-\alpha} & -j\sqrt{\alpha} \\ -j\sqrt{\alpha} & \sqrt{1-\alpha} \end{bmatrix} \text{ and } \begin{bmatrix} \sqrt{1-\beta} & -j\sqrt{\beta} \\ -j\sqrt{\beta} & \sqrt{1-\beta} \end{bmatrix} \tag{21}$$

For this case study, we can assume that the last two couplers to the right of Fig. 3 are perfect 50 % - 50 %. The signals out of this hybrid, after balanced photodection, would be

$$\begin{aligned} i_1 &\propto 2\sqrt{1-\alpha}\sqrt{\beta}\,\mathrm{Re}\{E_{\mathrm{S}}E_{\mathrm{LO}}^{*}\} \\ i_2 &\propto 2\sqrt{\alpha}\sqrt{1-\beta}\,\mathrm{Im}\{E_{\mathrm{S}}E_{\mathrm{LO}}^{*}\} \end{aligned} \tag{22}$$

In this case, we observe that there is no DC component (because the last two couplers are 50 % - 50 %) but the multipliers of the real and imaginary part of $\{E_{\mathrm{S}}E_{\mathrm{LO}}^{*}\}$ are different. This has a direct impact on their variances which is supposed to be equal. To compensate for this, we modify $V_{\text{I-x}}$ such that $V_{\text{I-x}} \rightarrow V_{\text{I-x}} \cdot (\sigma_{\text{R-x}}/\sigma_{\text{I-x}})$ and repeat the same for the y polarisation signals, represented by the -y subscript. Here $\sigma_{\text{R-x}}$ is the square root of the variance of $V_{\text{R-x}}$. This whole process of removing the mean (due to imperfect couplers) and equating the variances (due to different power splitting coefficients of the first two couplers) is called *I-Q* amplitude imbalance correction.

3.2.2 – Optical Hybrid Angle Imbalance

Another effect caused by the 90° optical hybrids is the phase mismatch of the output *I* and *Q* signals. We studied in Eq. (4) the four outputs in the general case where the phase retarders of upper and lower branch phase of the 90° optical hybrid (see Fig. 3) are ϕ_1 and ϕ_2 and ended up with the set of equations in (6) by setting ϕ_1 to 0 and ϕ_2 to $\pi/2$. Let's study the impact of a phase retarder ϕ_2 that is slightly off $\pi/2$, i.e., the case where $\phi_2 = \pi/2 + \delta$. To simplify this study, we consider that the four directional couplers are identical and evenly split inbound optical powers. By using the matrices in Eq. (4) with $\phi_2 = \pi/2 + \delta$ and $\phi_1 = 0$ we can prove that the two balanced photocurrents are now identified by

$$\begin{aligned} i_1 &\propto \mathrm{Re}\{E_S E_{LO}^*\} \\ i_2 &\propto \mathrm{Im}\{E_S E_{LO}^* e^{-j\delta}\} \end{aligned} \tag{23}$$

where δ is assumed to be small compared to $\pi/2$ and represents a deviation from the optimum optical path length. The consequence of such phase deviation is that the signal's constellation will be distorted and compressed in one direction. We can easily visualize this using the analogy of a perfectly circularly polarised light that suddenly experience a slight phase shift on one axis with respect to the other orthogonal axis. The perfectly circular polarisation will deform into an ellipsoid, i.e., a squeezed circle. The constellation is squeezed in the same manner when ϕ_2 is deviating from $\pi/2$. To rectify this impairment, one can simply remove the phase shift the imaginary part of $\{E_S E_{LO}^*\}$ before adding the real part to recover $\{E_S E_{LO}^*\}$. To explain in details how to recover $E_S E_{LO}^*$, let's simplify the study by saying that $E_S E_{LO}^* = a + j \cdot b$. We know that $\mathrm{Re}\{E_S E_{LO}^*\} = a$ and that $\mathrm{Im}\{E_S E_{LO}^* e^{-j\delta}\} = c = b \cdot \cos(\delta) - a \cdot \sin(\delta)$. We can then find *b* with our knowledge of a, c and δ. With *b* and *a*, we now recover $E_S E_{LO}^*$ with the following operation, using the definitions in Eq. (23),

$$E_S E_{LO}^{*} = \frac{1}{\cos(\delta)}\left(i_1 \cdot e^{j\delta} + j \cdot i_2\right) \tag{24}$$

As each 90° hybrid, receiving the $\hat{x}$ and $\hat{y}$ components, has its own small phase shift δ, the previous operation has to be applied to each of the two pair of signals $(I-Q)_{\hat{x}}$ and $(I-Q)_{\hat{y}}$ signals with their own phase mismatch $\delta_{\hat{x}}$ and $\delta_{\hat{y}}$. This phase mismatch does not vary in time and is an inherent impairment due to the finite fabrication precision of optical hybrids. This operation is called *I-Q* angle imbalance correction and is even more detailed in [21] and especially in [31]. Optical hybrid's amplitude and phase correction is applied to every *I* and *Q* samples, for each polarisations.

3.2.3 – Resampling at Twice the Baud Rate

The numerical operations we will apply to the acquired signals will be based on a twofold oversampling with respect to the baud rate, or $T/2$. We explained in the previous section the pros and cons of sampling two times per symbol duration. In our experimental setup, we will transmit at a symbol rate of 10 Gsymbols/s and use Analog to Digital Converters working at a fix sampling rate of 50 Gsamples/s, giving a five-fold oversampling factor with respect to the baud rate. Therefore, we need to downsample from 50 to 20, by a factor of 2.5. Downsampling by a factor that is not an integer is subtle and we will discuss of this in subsequent sections. In this section we lay out the basic methods of two different ways for downsampling by a factor of 2.5: one done in the frequency domain and the other done in the time domain.

3.2.3.1 –Frequency Domain Downsampling

The way to downsample by a non integer factor is easily done in the frequency domain. In fact, downsampling by any factor, rational or not, is straightforwardly achievable in the frequency domain. We know that the sampling rate of the ADCs is fixed at 50 GSa/s. At such a rate, the unaliased frequency content goes up to 25

GHz [25]. We know that our signal has a symbol rate of 10 GSym/s and we will see in a future section that our signal's single-side bandwidth is 10 GHz, or a full width of 20 GHz. The following figure describe the general view of how any downsampling is in done in the frequency domain.

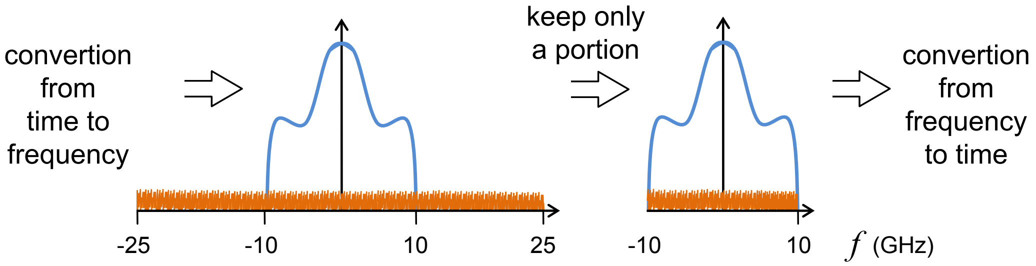

Fig. 10 – Downsampling method in the frequency domain

Each sample collected is spaced in time by $1/(50\,\text{GSa/s}) = 20\,\text{ps/Sa}$ and we collect for a certain amount of time, Δ seconds. Therefore, in Δ seconds we have $\Delta/(20\,\text{ps/Sa})$ samples. To diminish the number of samples but keep the same total time duration Δ, we have to increase the time between two samples. The schematic of such a process is depicted in Fig. 10. We convert our acquired signal into the frequency domain using the Fourier Transform. This gives a signal represented on the left-hand side of Fig. 10, consisting of the useful signal and noise spanning up to 25 GHz. By converting back in time only the central portion of interest, for instance the resulting frequencial signal spanning from -10 GHz to 10 GHz, we will obtain a temporal signal with $25/10 = 2.5$ times less samples but lasting the same duration in the time domain. Consequently, this decreases the sample rate. Actually we could downsample by any factor k from 1.0 to 2.5 by simply converting back to time the appropriate portion of the frequencial signal, namely from $-25/k$ GHz to $25/k$ GHz. In our case, we use $k = 2.5$.

3.2.3.2 – Time Domain Downsampling

The second way to downsample by a fractional factor is a process applied entirely in the time domain. This process can be summarized in three operations: upsampling, filtering and decimating. In fact, downsampling by a rational factor of M/N is very similar to simply decimating by N; it is only preceded by an upsampling process of a factor M. Therefore, we first study the process of decimating by a factor N. Let's imagine a numerical signal that has a frequency content going up to 25 GHz that we want to decimate by a factor of N. One could think of simply keeping 1 sample every N samples as a way to downsample. This simple operation doesn't decimate the sampling rate because the resulting signal would still have a frequency content up to 25 GHz. In other words, keeping a sample every N samples does not diminish the frequency content and simply result in signal aliasing. To avoid this aliasing, we need to filter in the first place the signal in time domain and then retain a sample every N samples. The temporal filter is the impulse response of a perfect low pass rectangular frequency domain filter which keeps intact $100\%/N$ of the frequency content and sets the remaining frequency content to zero. For instance, for $N=5$, the temporal filter is the impulse response of a frequency filter for which $H(f)=1$ for $|f|\leq(25\,\mathrm{GHz})/N=5\,\mathrm{GHz}$ and 0 elsewhere. Applying this filter assures that the resulting signal has frequency content bounded at 5 GHz, allowing us to retain without any aliasing one sample every $N=5$ samples for decimation.

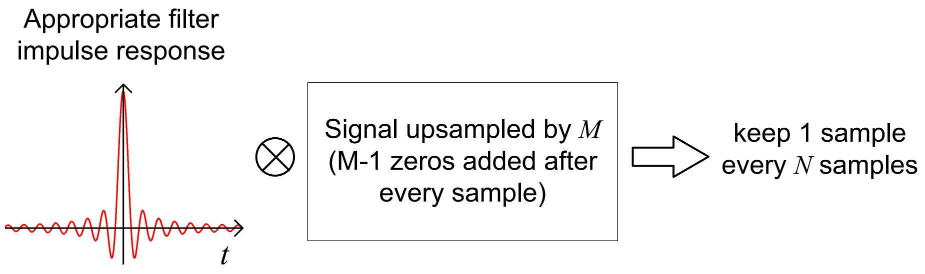

Fig. 11 – Downsampling method in the time domain

Now, imagine that we want to decimate by a factor $M/N=1/K$ a signal having frequency content up to 25 GHz. As an example, let's take $2/5=1/2.5$. The first step of the previous case where we filter by the impulse response of the filter $H(f)=1$ for $|f|\leq(25\,\mathrm{GHz})/K=10\,\mathrm{GHz}$ can still be applied with no problem. The only problem comes when we need to take a sample every $K=2.5$ samples, which is impossible. The way to realise this is to initially upsample the signal by a factor of $M=2$. Interpolation does not add any new frequency content to the signal, besides doubling the frequency span by padding zeros. The interpolated signal is then temporally filtered the same way as described above, with the appropriate filter removing content above $(25\,\text{GHz})/K = 10\,\text{GHz}$ and finally, 1 sample every $N = 5$ is retained to obtain the temporally downsampled signal by a factor of $K = 2.5$. Fig. 11 is a representation of how downsampling by a factorizable number is realized in the time domain, where $\otimes$ denotes convolution.

3.2.4 – Pulse Shaping and Matched Filtering

In this section, we will get familiar with pulse shaping at the transmitter and matched filters located at the receiver. Pulse shaping represents how the logical information will be imprinted in a temporal signal to be transported in the channel. For instance, if the modulation format used is BPSK and we have a sequence s_k , $k = 0, 1, 2, \ldots$ to send where each $s_i \in \{-1, 1\}$, the pulse shape will represent the temporal waveform onto which the information s_k is imprinted. A pulse shape has its frequency representation and both the frequency domain and time domain characteristics of the pulse are of tremendous importance. The maximum width of the pulse, when represented in the frequency domain, designates the signal's bandwidth. While propagating, pulses will be impaired and noise will be added. Consequently, the receiver always includes a filter suppressing noise from frequencies out of the useful signal's band, called out-of-band noise. Such receiver filter can also improve the receiver's response to the type of pulse used, named Matched Filters.

The most basic type of receiver filter for a signal of single-side bandwidth W is a rectangular filter with a frequency response of $R(f) = 1$ for $|f| \le W$ and 0 elsewhere. The information symbols to transmit are conveyed by the temporal pulses $p(t)$ created at the transmitter, where $p(t)$ is the inverse Fourier Transform of $P(f)$, which can also be considered as a pulse shaping filter, applied at the transmitter. We call a matched filter at the receiver a filter that is matched to the pulse shaping filter $P(f)$. Matched filter maximizes the signal to noise ratio (SNR) at its output when a signal passes through an additive white

Gaussian noise (AWGN) channel [32] as the optical fibre is [33]. A matched filter $H(f)$ at the receiver has an impulse response $h(t)$ that is a flipped version of the transmitter pulse shape, i.e., $h(t) = p(-t)$. There are lots of possible matched filters to use for the transmission of signals. The most common ones or called the Root-Raised Cosine (RRC) filters. RRC filters are defines such that two sequential RRC filter act as a single Raised Cosine (RC) filter, where a RRC filter is the square root of a RC filter. Raised Cosine filters are apodized rectangular filter that have an impulse response that is null at every T seconds, where T is the symbol duration. A RC pulse shape gives no intersymbol interference (ISI) when the receiver samples once every T seconds, at the center of pulses. Therefore, the presence of neighbouring symbols is seamless to the symbol of interest. A Root Raised Cosine filter has the following frequency response and impulse response

$$X_{RRC}(f) = \begin{cases} \sqrt{T} & 0 \le |f| \le \dfrac{(1-\alpha)}{2T} \\ \sqrt{\dfrac{T}{2}\left[1+\cos\left(\dfrac{\pi T}{\alpha}\left(|f| - \dfrac{(1-\alpha)}{2T}\right)\right)\right]} & \dfrac{(1-\alpha)}{2T} < |f| \le \dfrac{(1+\alpha)}{2T} \\ 0 & |f| > \dfrac{(1+\alpha)}{2T} \end{cases} \tag{25}$$

$$x_{RRC}(t) = \frac{\sin\left(\dfrac{\pi t}{T}(1-\alpha)\right) + \dfrac{4\alpha t}{T}\cos\left(\dfrac{\pi t}{T}(1+\alpha)\right)}{\dfrac{\pi t}{\sqrt{T}}\left(1-\left(\dfrac{4\alpha t}{T}\right)^2\right)} \tag{26}$$

As mentioned above, $X_{RRC}(f) = \sqrt{|X_{RC}(f)|}e^{-j2\pi f t_o}$ where t_o is some nominal delay required to ensure physical realizability of the filter. In the time domain, $x_{RC}(t) = x_{RRC}(t) \otimes x_{RRC}(t)$, where $\otimes$ denotes convolution. Here, we clearly see that if our pulse shape at the transmitter is $x_{RRC}(t)$ and we filter at the receiver with $h(t) = x_{RRC}(T-t)$ before sampling, we will benefit from matched filtering and synchronised sampling once every T seconds will show no ISI. In the equations above, α is called the *roll-off parameter* or the *excess bandwidth* and is a measure of percentage of excess bandwidth with respect to the minimum signal bandwidth of $f = 1/2T$ for rectangular filters (when $\alpha = 0$). The roll-off parameter α can vary from 0 to 1, where the signal's bandwidth is $f = 1/2T$ for $\alpha = 0$ and is $f = (1+\alpha)/2T$ for a specific excess bandwidth α. Here, we clearly realize that for $\alpha = 1$, the signal's bandwidth is twice the one for $\alpha = 0$ and consequently the required Nyquist sampling rate doubles at $2/T$. It is important to mention here that even if an excess bandwidth is used for pulse shaping at the transmitter, the symbol rate remains $1/T$. We therefore realize that for the specific case where $\alpha = 1$, Nyquist sampling at $2/T$ is not considered oversampling but our study on T/2-fractionally spaced equalizers applies because we still sample two times for each symbol.

There are some advantages and disadvantages of using a RRC pulse shape with a RRC matched filter of large excess bandwidth α. The main advantage is most clearly seen when we look at the $x_{RC}(t) = x_{RRC}(t) \otimes x_{RRC}(t)$ equation

$$x_{RC}(t) = \frac{\sin\left(\frac{\pi t}{T}\right)}{\frac{\pi t}{T}} \cdot \frac{\cos\left(\frac{\pi \alpha t}{T}\right)}{1 - \left(\frac{2\alpha t}{T}\right)^2} \tag{27}$$

Here, we notice that for $\alpha = 0$, there's no excess bandwidth and we find back the rectangular filter of $H(f) = T$ for $f \le 1/2T$ and 0 elsewhere. We observe that the tails of $x_{RC}(t)$ decay as $1/t$. Consequently, a small mistiming error $t = nT + \delta_o$ in sampling epoch at the receiver results in an infinite series of ISI components. Such a series is not absolutely summable because of the $1/t$ rate and does not converge. However, when a certain excess bandwidth $\alpha > 0$ is used, $x_{RC}(t)$ decay as $1/\alpha^2 t^3$ and a mistiming error in sampling leads to a series of ISI components that converges to a finite value, and converges faster and to a smaller value as α increases.

The drawback of using an excess bandwidth is first of all the necessity of sampling $(1+\alpha)$-times the required speed when $\alpha = 0$. Moreover, higher α exhibits a spectral efficiency loss of a factor $1/(1+\alpha)$. By spectral efficiency, we mean that if we were to concatenate several channels of information, each having a $X_{RRC}(f)$ pulse shaping filter and matched filter with maximum bandwidth $W=(1+\alpha)/2T$ and symbol rates of $1/T$ symbols/s, the closest apart two consecutive spectrum $X_{RRC}^{n}(f-nF)$, $n=\{k,k+1\}$, could be is $F=2W$ Hz away. As W increases with α, for the same symbol rate we get a spectral efficiency of $1/(TF)=1/(1+\alpha)$ symbols/s/Hz which decreases with increasing α.

It is worth mentioning that for non-coherent transmission of an *electrical* signal, the signal at the receiver can first enter the matched electrical filter $X_{RRC}(f)$ and is then be sampled every $T/(1+\alpha)$ seconds. In our case, with an optical coherent receiver like the one in Fig. 7, neither the optical signal nor the electrical signals after the balanced photodetectors are analogously match filtered. The filtering part is done after the ADCs, through digital signal processing. The following figure depicts the matched filtering that has to be applied at the receiver side for both temporal filters and frequencial filters. Just like the resampling process we previously introduced, matched filtering can be done in the time domain and in the frequency domain. The $x_{RRC}(t)$ pulse shape (to the left) or its equivalent pulse filter $X_{RRC}(f)$ (to the right) are specific representations for $\alpha=1$. Here, $\otimes$ denotes convolution and $\times$, multiplication.

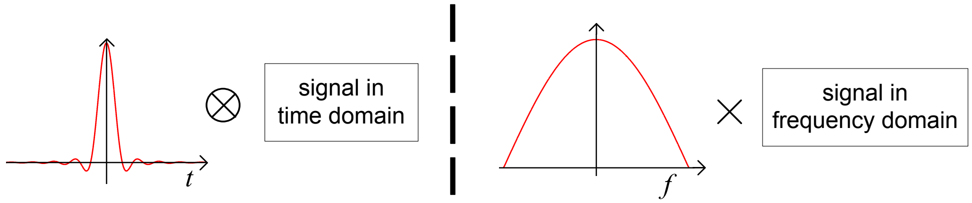

Fig. 12 – Matched Filtering at the receiver. Applied in (left) time or (right) frequency domain

3.2.5– Chromatic Dispersion Compensation

The optical fibre is a transmission channel that exhibits chromatic dispersion (CD), that is, where different optical frequencies travel at different speeds, or in other words, where the speed of light is frequency dependant. The transfer function of an optical fibre is well known to be

$$H(\omega)=e^{-j\frac{1}{2}\beta_2 L\omega^2} \quad \text{or} \quad h(t)=\frac{e^{j\frac{t^2}{2\beta_2 L}}}{\sqrt{j2\pi\beta_2 L}} \tag{28}$$

where $\beta_2 = d^2\beta/d\omega^2 = d(1/v_g)/d\omega$ is the group velocity dispersion (GVD) and determines how much an optical pulse will broaden while propagating inside the fibre and L is the length of the fibre. β is the propagation constant and is function of the frequency. It also defines the group velocity $v_g(\omega)=(d\beta/d\omega)^{-1}$ which represent the speed at which a specific spectral component at ω travels. In Eq. (28) we observe the transfer function of the optical fibre represented in the frequency domain (left hand side) and in the time domain (right hand side). We clearly see that the fibre transfer function acts an all-pass filter, meaning that it is an unbounded filter, and therefore its impulse response $h(t)$ is also a double-sided and infinitely long response. For standard Single Mode Fibre, the GVD parameter $\beta_2 = -21.87\,\text{ps}^2/\text{nm}$ at the wavelength $\lambda = 1547.5\,\text{nm}$. The GVD can also be expressed as a function of λ instead of ω, by defining a dispersion parameter $D=d(1/v_g)/d\lambda=-2\pi c\beta_2/\lambda^2$, where $D = 17.2\ \text{ps}/(\text{nm}\cdot\text{km})$ for SMF fibre.

To compensate for chromatic dispersion, we simply need to apply the inverse of the transfer function described in Eq. (28), by using the opposite group velocity dispersion of the fibre, i.e., $\beta_2 \to -\beta_2$. As for the matched filtering and the downsampling, chromatic dispersion compensation can be applied either in the time or in the frequency domain. We will study in a later section the advantages and disadvantages of choosing one approach or the other. Finally, Fig. 12 helps us understand how to apply chromatic dispersion compensation (CD^{-1}) in time and in frequency domain. CD^{-1} and matched filtering can be applied the same way.

3.2.6 – Non-linear impairment mitigation

On top of chromatic dispersion, the optical fibre also exhibits nonlinearity. Nonlinearity comes from the dependence of the refractive index of the material that consist the optical fibre on the intensity of the light travelling inside it. It is well known in the literature that for an optical wave on two polarizations $\vec{E}=E_x\hat{x}+E_y\hat{y}$, the Polarization Coupled Nonlinear Schrödinger's Equation is

$$\begin{aligned}\frac{\partial E_x}{\partial z}+\beta_{1x}\frac{\partial E_x}{\partial t}-j\frac{\beta_2}{2}\frac{\partial^2 Ex}{\partial t^2}+\frac{\alpha}{2}=-j\gamma\left(\left|E_x\right|^2+\frac{2}{3}\left|E_x\right|^2\right)E_x\\ \frac{\partial E_y}{\partial z}+\beta_{1y}\frac{\partial E_y}{\partial t}-j\frac{\beta_2}{2}\frac{\partial^2 Ey}{\partial t^2}+\frac{\alpha}{2}=-j\gamma\left(\left|E_y\right|^2+\frac{2}{3}\left|E_x\right|^2\right)E_y\end{aligned} \tag{29}$$

where E_x and E_y are complex fields [34] and γ is the nonlinear parameter defined as $\gamma=n_2(\omega_o)\cdot\omega_o/(c\cdot Ae_{ff})$. For a central wavelength of 1547.715 nm, the nonlinear (NL) refractive index n_2 is 2.56×10^{-20} m^2/W and the effective area is $A_{eff}=80\ \mu\mathrm{m}^2$ in a standard single mode fibre, giving a $\gamma=0.0013\ \mathrm{m}^{-1}\mathrm{W}^{-1}$. The first term of the right-hand side of Eq. (29) is responsible for a nonlinear impairment called Self-Phase Modulation (SPM) while the second term is responsible for the nonlinear impairment called Polarization Cross-Phase Modulation (Pol-XPM). SPM causes a nonlinear phase shift acquired by one polarization due to its own polarization component's power while Pol-XPM causes a nonlinear phase shift due to the other polarization component's power. As we will use a signal modulated on two orthogonal polarizations (see Eq. (15)), these nonlinear phase shifts apply to our signals. As we can observe in Eq. (29), the strength of the nonlinear phase shifts shown in parentheses are proportional to the power of the optical signal on the $\hat{x}$ and the $\hat{y}$ components. Therefore, for some low power, the nonlinear phase shifts are negligible. As the power increases, they become very important and a lot of NL phase shifts are imprinted on E_x and E_y.

The most common way to suppress nonlinear phase shifts are through the well-known Split-Step Fourier Method (SSFM) [34] in back propagation mode. This method is often used to solve nonlinear differential equations and is more precisely used for beam propagation. SSFM is a way to apply iteratively the linear and the nonlinear part of a differential equation like Eq. (29) as 2 independent linear operators over a short distance. Mathematically, if we cast Eq. (29) in the form $\partial E_i(z,t)/\partial z=(\hat{D}+\hat{N}_i)E_i(z,t)$ where $i\in\{x,y\}$, we can find the field at $z+\Delta z$ as $E_i(z+\Delta z,t)=e^{\Delta z\hat{D}}e^{\Delta z\hat{N}_i}E_i(z,t)$ for i representing either x or y with $\hat{N}_x=-j\gamma(\left|E_x(z,t)\right|^2+2\left|E_y(z,t)\right|^2/3)$ and $\hat{N}_y=-j\gamma(\left|E_y(z,t)\right|^2+2\left|E_x(z,t)\right|^2/3)$ as nonlinear operators and $\hat{D}=-j\beta_2\omega^2/2-\alpha/2$ as the linear operator taking both chromatic dispersion and attenuation into account when we assume that the mean group velocities of $\hat{x}$ and $\hat{y}$ are the same ($\beta_{1x}=\beta_{1y}$). This hypothesis is satisfied for long haul transmission as the states of polarization $\hat{X}_t$ and $\hat{Y}_t$ onto which E_x and E_y are modulated rotate while propagating and because the two signals come from the same laser at the transmitter and are therefore propagating at the same carrier frequency. The finer the distance Δz propagated each time the more realistic the approach is, at the expense of extra computation time requirements. One can find reliable results at a certain Δz that barely change when decreasing the step size, making the extra computational time useless. The $\hat{D}$ operator is normally applied in the frequency domain using the left-hand side of Eq. (28). The calculation of $\hat{N}_x$ and $\hat{N}_y$ is repeated for each Δz increment until the distance L is traveled. We will use the SSFM technique for nonlinear impairments mitigation.

When we mitigate nonlinear phase shifts using the SSFM, chromatic dispersion is compensated at the same time, and therefore does not need to be previously compensated for. That is the reason why we coupled chromatic dispersion compensation and nonlinear compensation in Fig. 9: if no NL compensation is applied, CD is applied alone, when NL is compensated, CD is simultaneously compensated.

3.2.7 – PMD and PDL Compensation, Polarisation Demultiplexing

The optical fibre can be represented by two orthogonal axes that can present slightly different refractive index and attenuation coefficient. The slight difference in refractive indices of the two orthogonal axes is called the birefringence of the fibre and cause polarized light to travel at different speeds. This property induces a temporal spreading of the light pulse as it propagates, because the portion of light in each orthogonal axis doesn't travel at the same speed. This phenomenon is called Polarization Mode Dispersion [35]. Moreover, a slight different attenuation coefficient on each axis leads to what is called Polarisation Dependent Loss. Even though silica fibres themselves have relatively little PDL, the signal passes through a variety of optical components in a transmission link such as modulators, isolators, amplifiers, filters and couplers, most of which exhibit loss (or gain in the case of optical amplifiers) whose magnitude depends on the state of polarizations of the signal. PDL leads to unequal signal power of E_x and E_y.

PDL can cause interaction between the two signal information originally imprinted on orthogonal, non cross-talking axes. This behaviour can reduce the extinction ratio of each signal on its polarized light. It can also induce inband crosstalks and vary the OSNR on each polarization with respect to the average OSNR [36]. The performance of a polarisation multiplexed data stream is determined not only by the average optical signal to noise ratio, but also by the optical signal to noise ratio of the two polarization tributaries. Although in most cases, a similar OSNR can be expected on both tributaries, this situation changes in the presence of PDL.

To demonstrate the impact of PDL, imagine two orthogonally polarized lightwaves E_X and E_Y entering a section at angle θ with respect to two orthogonal fibre axis $\hat{x}$ and $\hat{y}$, where the $\hat{x}$ axis has a power attenuation coefficient of β and the $\hat{y}$ axis is lossless. As depicted in the next figure, the polarization multiplexed signals E_X and E_Y are no longer orthogonal. The new

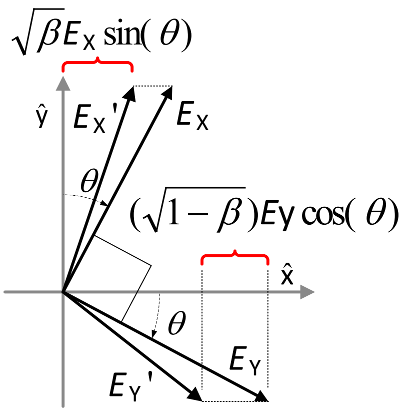

Fig. 13 – Impact of PDL on Pololarization Multiplexed Signals

signals E_X' and E_Y' will crosstalk after demultiplexing onto any orthogonal basis. Moreover, we can clearly see in Fig. 13 that the total power of E_X and E_Y has diminished, which directly leads to a smaller OSNR for signals E_X' and E_Y'. It is important to mention that the principal fibre axis change in space along the fibre, mainly because continuous sections of fibre are not flawless, perfectly cylindrical fibre and can contain mechanical stress. Slight temperature variations throughout the fibre length can also cause small refractive index and power attenuation coefficient variations.

As introduced in Eq. (12) and (13), the required processing for a coherent receiver to properly recover E_X and E_Y when it receives $E_{S,\hat{x}}E^*_{LO,\hat{x}}$ and $E_{S,\hat{y}}E^*_{LO,\hat{y}}$ has to include cancelling of PMD, PDL and to properly demultiplex the two Pol-Mux information streams. The information we receive E_X' and E_Y' (see Fig. 13) right before the coherent receiver front end is likely not orthogonal, has suffered from PMD and has unequal average optical power. In order to extract E_X and E_Y from E_X' and E_Y', a multiple-input–multiple-output (MIMO) equalizer is used. In fact, because of PDL and PMD the optical channel is itself a MIMO system. Polarization demultiplexing is one of the most interesting problems of coherent receiver design [37] and we have to tackle it. We will detail in the next section how to numerically implement the issues due to polarizations but for now we will only present an overview of the required compensations

We use a MIMO filter that is called in the scientific community a "Butterfly Filter". It has two complex inputs and two complex outputs that consist of the sum of the two inputs independently filtered, and that, respectively for the two polarizations. The filter is depicted in Fig. 14. It consist of 4 complex valued Finite Impulse Response filters $\vec{h}_{xx}$, $\vec{h}_{xy}$, $\vec{h}_{yx}$ and $\vec{h}_{yy}$ each having a certain length *N*. This type of MIMO filter can be represented with the Jones transformation matrix [38, 39] where the input-output relation is dictated by Eq. (30) [40]. Each element $\vec{h}_{ij}$ of this matrix is in fact a vector of length *N* to apply to *N* sequential samples in E_X' and E_Y' in a dot-product from in order to create a pair of scalar outputs E_X and E_Y. The vectors $\vec{h}_{ij}$ of the filters can be updated with the known Constant Modulus Algorithm [41-43] (CMA), which goes as follows

$$\begin{bmatrix} E_x \\ E_y \end{bmatrix} \left(= \begin{bmatrix} x_{out} \\ y_{out} \end{bmatrix} \right) = \begin{bmatrix} \vec{h}_{xx} & \vec{h}_{yx} \\ \vec{h}_{xy} & \vec{h}_{yy} \end{bmatrix} \begin{bmatrix} \vec{E}_x' \\ \vec{E}_y' \end{bmatrix} = \mathbf{H} \begin{bmatrix} \vec{E}_x' \\ \vec{E}_y' \end{bmatrix} \left(= \mathbf{H} \begin{bmatrix} \vec{x}_{in} \\ \vec{y}_{in} \end{bmatrix} \right) \tag{30}$$

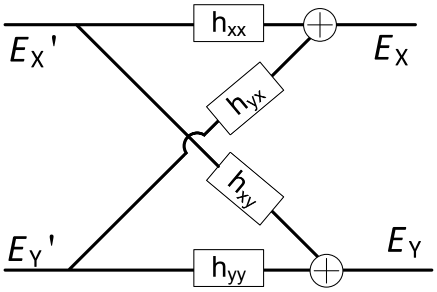

Fig. 14 – 2 X 2 Multiple-Input-Multiple-Output Filter for Polarization Related Impairments

$$\begin{aligned}
\vec{h}_{xx}^{i+1} &= \vec{h}_{xx}^{i} + \mu\,(1-|x_{out}|^2)\,x_{out}\cdot\vec{x}_{in}^{*} \\
\vec{h}_{yx}^{i+1} &= \vec{h}_{yx}^{i} + \mu\,(1-|x_{out}|^2)\,x_{out}\cdot\vec{y}_{in}^{*} \\
\vec{h}_{xy}^{i+1} &= \vec{h}_{xy}^{i} + \mu\,(1-|y_{out}|^2)\,y_{out}\cdot\vec{x}_{in}^{*} \\
\vec{h}_{yy}^{i+1} &= \vec{h}_{yy}^{i} + \mu\,(1-|y_{out}|^2)\,y_{out}\cdot\vec{y}_{in}^{*}
\end{aligned} \tag{31}$$

where $x_{out} = \vec{h}_{xx}^{\dagger}\cdot\vec{x}_{in} + \vec{h}_{yx}^{\dagger}\cdot\vec{y}_{in}$ and $y_{out} = \vec{h}_{xy}^{\dagger}\cdot\vec{x}_{in} + \vec{h}_{yy}^{\dagger}\cdot\vec{y}_{in}$, * denotes complex conjugate, † denotes the transpose of the complex conjugate and $0 < \mu < 1$ is a small step size factor. We will use this CMA adaptation for our MIMO filter. The 4 coefficients are updated at the symbol rate and the input vectors $\vec{x}_{in}$ and $\vec{y}_{in}$ are

$T/2$-spaced. Processing a twofold oversampled input with respect the baud rate gives the ability to this filter for retiming of the input signals [44].

The reason why we use the CMA algorithm as the method for updating the coefficients in each $\vec{h}_{ij}$ are many-fold: First of all, it can mitigate simultaneously the impact of cross-talk, PMD, PDL and small residual Chromatic Dispersion [45]. It also offers a relative simple complexity and easy hardware implementation, it blindly equalizes the input signal without requiring the knowledge of the desired symbols for updating (no training sequence necessary) and finally it takes into account the type of modulation format used for transmission, i.e., QPSK in our case. The 4-ary Quadrature and Amplitude Modulation scheme has a constant amplitude and a phase varying on 4 different states, all equally spaced. The Constant Modulus Algorithm updates the coefficients such that they minimize the square error $\varepsilon^2 = (1-|y|^2)^2$, where $y = \vec{w}^{\dagger} \cdot \vec{x}$ is, in the general case, the complex output value where the filter $\vec{w}$ is applied to the input $\vec{x}$. We clearly observe that the minimisation is solely based on the magnitude of the output value y and not on any desired or decided value. Updating the coefficients such that ε^2 is minimized directly leads to updating such that $|y|^2$ tends towards 1. This is exactly what we need, as we know that we want our output signals to have constant magnitude, the property of QPSK modulation. Fig. 13 gives the visual representation of what the CMA equalizer does: if E_X and E_Y have equal and constant amplitude, $E_X{}'$ and $E_Y{}'$ don't and the equalizer serves to push to unity the square magnitude of the orthogonally collected signals, $|E_{S,\hat{x}}|^2$ and $|E_{S,\hat{y}}|^2$ which eliminates cross talk, PDL and PMD.

If the fibre would present no Polarization Dependent Loss, the **H** matrix in (30) would be a unitary matrix, with the property that $\vec{h}_{yy} = \vec{h}_{xx}^*$ and $\vec{h}_{xy} = -\vec{h}_{yx}^*$ and therefore where $|\vec{h}_{xx}|^2 + |\vec{h}_{yx}|^2 = 1$ [40]. This property will not hold in a real system because of PDL and hence we cannot obtain a coefficient $\vec{h}_{ij}$ from its diagonal opposite $\vec{h}_{ji}$: we have to calculate the 4 coefficients $\vec{h}_{ij}$ independently as dictated in Eq. (31).

3.2.8 – Carrier and LO Frequency Offset Removal

In this section, we describe how to remove the frequency offset between the light received and the light from the local oscillator. As mentioned earlier, a coherent receiver mixes the light of a local oscillator with that of the signal. Even with today's fine tunable local oscillators, it is very difficult, not to say impossible, to tune the free running LO exactly to the frequency of the signal. The first reason is because of the finite resolution of tunable lasers. Around 193.7 THz where the frequency of the transmitting laser sits, tuning another laser at a frequency within 100 KHz requires a wavelength precision smaller than the femtometer, which is practically impossible to obtain. However, tunable lasers with a wavelength accuracy smaller or equal to $\pm 1\,\text{pm}$ are commercially available [46]. Such a wavelength precision converts into a frequency precision smaller than 125 MHz around 1547.715 nm. The second reason why the received light and the LO have variable frequencies is because of their respective independent phase noise. Phase noise is summarized as a random walk of the phase in time, which gives two independent instantaneous frequencies that will not match. Matching the LO frequency with that of the signal could be done in an optical phase locked loop, but adds a lot of undesired complexity to the receiver and is out of our interest.

To find the frequency offset between the Signal and the LO, we have to remove the modulated information imprinted in the phase of Signal. Each polarisation signals E_S^X and E_S^Y is modulated onto 4 phases. Taking the fourth power of a QPSK signal, for instance $\left(E_S^X\right)^4$ and $\left(E_S^Y\right)^4$, will remove the phase information and will bring all the possible states in the constellation to a unique state. . The constellation we observe at the receiver is rotating at an angular speed of $\omega_{IF} = \omega_S - \omega_{LO}$ [47]. Now taking the fourth power of each rotating point in the constellation will give a single point rotating 4 times faster than the intermediate frequency ω_{IF}. The following figure depicts this situation.

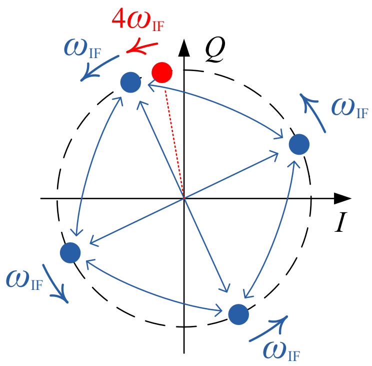

Fig. 15 – Removing the Phase Information on a Rotating QPSK Signal by Taking the 4th Power

There are two ways to find the intermediate frequency $f_{\mathrm{IF}} = \omega_{\mathrm{IF}} / 2\pi$: a time domain approach and a frequency domain approach. In order to find $4\omega_{\mathrm{IF}}$ using a frequency domain approach, we have to compute the Fourier transform of the 4th power of a sequence of symbols of length N. We then calculate the magnitude of this Fourier transform and the frequency at which the transform has the highest power spectral density represents $4\omega_{\mathrm{IF}}$. Having found ω_{IF}, we can remove it from the signal by applying $E = Ee^{-j\omega_{\mathrm{IF}} t}$. In a time domain approach, we don't need the Fourier transform for processing. The method is well explained in [47] and requires each sampled symbol to be multiplied by the complex conjugate of the previous one. The result is put to the 4th power, again to remove the QPSK modulation information and deal only with phase drifts. Multiple results of this operation are summed. Finally, the angle of this sum represents $4\omega_{\mathrm{IF}}$ and we remove this mean frequency deviation again by applying $E = Ee^{-j\omega_{\mathrm{IF}} t}$ to the signal E . Lets explain this temporal approach visually and consider that we have a sequence of digitized symbols $[e^{j\varphi_k}, e^{j\varphi_{k+1}}, e^{j\varphi_{k+2}}, e^{j\varphi_{k+3}}, e^{j\varphi_{k+4}}, ...]$. Here we assume unit amplitude for simplicity of writing and because we are only interested in the phase components but this assumption is not required and the results still valid for small amplitude deviation from unity. This process takes the sum of the elements in $[e^{4j(\varphi_{k+1}-\varphi_k)}, e^{4j(\varphi_{k+2}-\varphi_{k+1})}, e^{4j(\varphi_{k+3}-\varphi_{k+2})}, ...]$ and compute the angle of this sum. By considering that $\varphi_k \approx k \cdot \omega_{\mathrm{IF}}$, the resulting angle is in fact an averaged value of $4\omega_{\mathrm{IF}}$.

Both approaches are coarse as they only remove the average frequency difference between Signal and LO. Its goal is in fact to remove the bulk frequency offset and not the phase noise. For simplicity, if we assume that we receive a perfectly polarized signal, the signals we obtain are dictated by Eq. (17). The above process removes ω_{IF} but leaves untouched the difference of the phase noises $\phi_{\mathrm{IF}}(t) = \phi_{\mathrm{S}}(t) - \phi_{\mathrm{LO}}(t)$. As seen in Eq. (17), the bulk frequency offset ω_{IF} is the same for both signals, i.e., for both polarisations. Therefore, even if we only use the signal from one polarisation to find ω_{IF}, we can use the same result for intermediate frequency offset removal on both polarizations which inherently reduces the computational complexity.

3.2.9 – Carrier and LO Phase Noise Removal

This operation is intended to remove 3 angular components that the bulk frequency offset removal operation could not do. These components are 1) the remaining frequency offset, 2) the lasers phase noise and 3) the relative phase on the signal from each polarisation. It can be seen as a fine tuning of the previous operation (§ 3.2.8), but is applied in a totally different way. As mentioned above, the previous operation removes ω_{IF} but leaves $\phi_{\mathrm{IF}}(t)$ and the relative phases $\phi_{o,\mathrm{S},\hat{\mathrm{x}}_t}$, $\phi_{o,\mathrm{S},\hat{\mathrm{y}}_t}$, $\phi_{o,\mathrm{LO},\hat{\mathrm{x}}}$ and $\phi_{o,\mathrm{LO},\hat{\mathrm{y}}}$ intact. This operation completely removes these phases, and is applied independently for each polarization. As we did for the coarse frequency removal, this phase removal also works with the fourth power of each sample to remove the QPSK modulation and read only frequency and phase noise drifts.

We will explain how we remove phase noise and relative phases by defining the type of phase we deal with: randomly walking phase drifts. We explained in section 2.2 that the laser phase noise is described by a Wiener process as a randomly walking phase, starting at $\phi(t=0)=0$ and where the phase $\phi(t_o)$ at time $t=t_o$ as an integral from $t=0$ to t_o of Gaussian random variables. When working with discretized signals as we do with the coherent receiver, the integral naturally becomes a summation a Gaussian random variables, and we define $\phi_n \triangleq \phi(t=nT)$, where nT are sampled symbol and $\phi_0 = 0$. Each ϕ_n can be represented as a Gaussian variables distributed as $\phi_n \sim N(\hat{\phi}_{n-1}, 2\pi\varDelta vT)$, where $\hat{\phi}_{n-1}$ is the realization of the random variable ϕ_{n-1} and $\varDelta v$ is called the 3-dB linewidth of the laser phase noise. This previous equation gives us the flavour of how the summation comes into play. An ensemble of M realizations $\hat{\phi}_n$, $n=k,...,M+k-1$, of phase noises will therefore most likely not have a zero-mean, as the mean of the distribution of each phase ϕ_n is the value of the previous realization $\hat{\phi}_{n-1}$. We know from theory that the summation of two Gaussian random variables $N(\mu_1,\sigma_1^2)$ and $N(\mu_2,\sigma_2^2)$ gives a Gaussian variable of distribution $N(\mu_1+\mu_2,\sigma_1^2+\sigma_2^2)$. This means that the phase $\hat{\phi}_n$ at time $t=nT$ has a global variance of $2\pi\varDelta vnT$. Good lasers can have a linewidths as low as 100 KHz and we assume that the symbol rate is 10 Gsymbol/s, with T = 100 ps. If both the signal laser and the LO laser have linewiths of 100 KHz, the total linewidth when the two mix is summed at $\varDelta v = \varDelta v_{\text{SIG}} + \varDelta v_{\text{LO}} = 200$ KHz. However, as each sample $e^{j\hat{\varphi}_k}$ is put to the 4th power, $e^{j4\hat{\varphi}_k}$ exhibit a phase noise four times that of the real signal+LO phase noise. As we know, the variance of a Gaussian variable multiplied by four, $4N(\mu_1,\sigma_1^2)$, is 4^2=16 times greater, at $16\sigma_1^2$. Therefore, the variance between two consecutive samples in this phase noise removal process is $16\cdot 2\pi\varDelta vT \approx 2\times 10^{-3}$. If we take an ensemble of M samples $e^{j4\hat{\varphi}_n}$ where $\hat{\phi}_n$, $n=k,...,M+k-1$, the variance of the last phase $\hat{\phi}_{M+k-1}$ with respect to the first phase $\hat{\phi}_k$ will be $(M-1)32\pi\varDelta vT$ with $\hat{\phi}_{k=0} = 0$. To find an approximate maximal value for M for which the variance is considered small, we define that a small variance Φ in radian is such that $\cos(\Phi) = 0.95$ in order to approximate $\cos(\Phi) \approx 1$ and $\sin(\Phi) \approx \Phi$ with a maximal error of 5%. This gives a maximal variance of $\Phi = 0.317$ rad. We find we can sum up to a maximum of $M \approx 151$ phase noise random variables before reaching a phase noise that has a variance greater than 0.317.

What we collect at the receiver are $e^{j\hat{\phi}_k}$ and not $\hat{\phi}_k$. In order to apply our study on summation of Gaussian variables ϕ_k, we need to map $e^{j\hat{\phi}_k}$ to $\hat{\phi}_k$. As we know, $e^{j\hat{\phi}_k} = \cos(\hat{\phi}_k) + j\sin(\hat{\phi}_k)$. The only way $e^{j\hat{\phi}_k}$ can be approximated using $\hat{\phi}_k$ is if $\hat{\phi}_k$ is small. As $4\phi_1$ has a zero mean and a variance of $16 \cdot 2\pi\Delta\nu T \approx 2\times10^{-3}$, the assumption that $\hat{\phi}_k$'s are small is justified up to $k = M-1$ and $e^{j4\hat{\phi}_k}$ can be cast as $e^{j4\hat{\phi}_k} = (1 + j4\hat{\phi}_k)$ for $k = 0,...,M-1$ with a 5% accuracy. Now summing M terms of $e^{j4\hat{\phi}_k}$ turns to summing $(1 + j4\hat{\phi}_k)$ which is effectively $M(1 + j \cdot 1/M \sum_{k=0}^{M-1} 4\hat{\phi}_k)$. We observe that the imaginary term in this equation is the mean of the phase noise for acquisitions spanning from $k = 0$ to $k = M-1$, which is what we want to recover. This mean can be extracted from the summation $\zeta = 1/M \sum_{k=0}^{M-1} 4\hat{\phi}_k$ by taking the angle of the summation, as $\angle(1 + j\zeta) = \tan^{-1}(\zeta/1) \approx \zeta$ for small ζ. This technique is in fact known as the Viterbi and Viterbi feedforward carrier phase estimation algorithm for MPSK [48, 49]. As we proved earlier that the variance of the $M-1^{\text{th}}$ term $4\hat{\phi}_{M-1}$ is the greatest at $(M-1)32\pi\Delta\nu T \approx 0.317$, we can assume with confidence that the mean of the angles is small enough, knowing that $1/M \sum_{i=0}^{M-1} i = (M-1)/2$, and find the mean phase noise with the angle of the sum of $e^{j4\hat{\phi}_k}$.

Now let's study the case when a small residual frequency offset is added to the phase noise $\hat{\phi}_k$. We define a vector V that shows all the three angular components our algorithm has to remove, i.e., 1) the remaining frequency offset, 2) the lasers phase noise and 3) a relative phase. Let V be

$$V = e^{j4\Phi_o}\left[e^{j4\hat{\phi}_0}, e^{j4(\psi+\hat{\phi}_1)}, e^{j4(2\psi+j\hat{\phi}_2)}, e^{j4(3\psi+\hat{\phi}_3)}, e^{j4(4\psi+\hat{\phi}_4)}\right] \tag{32}$$

For visual simplicity, we use a short length for V, namely $M = 5$. We observe that V has a relative phase $4\Phi_o$, a frequency dependence $\psi = 2\pi fT$ and phase noises imprinted in the $\hat{\phi}_k$'s. We observe in Eq. (32) that the angular components can now be described by summations of Gaussian random variables, each distributed as

$$\angle_n \sim N(\hat{\angle}_{n-1} + 4\psi, 16 \cdot 2\pi\Delta\nu T) + 4\Phi_o \tag{33}$$

where $\hat{\angle}_k$ is the realization of the variable $\angle_k$. This distribution is an altered version of our previous distribution $\angle_n \sim N(\hat{\angle}_{n-1}, 16 \cdot 2\pi\Delta\nu T)$ for Wiener phase noise. The only difference is an inclusion of a frequency shift which constantly adds an offset of 4ψ to the mean of the distribution of each angular component, summing up and acting as an angular frequency. The relative phase Φ_o can be set to zero for simplicity of comparison. To see the impact of the frequency shift to the computation suggested above, allowing us to find the mean of the angles by the angle of the mean, let's compute the angle of the mean for angles distributed as in Eq. (33) but with a null linewidth, i.e., with $\Delta v = 0$. By taking V as example, we find that the angle of the mean of V is $4\Phi_o + (M-1)4\psi/2$. This value can readily be found with a drawing of M phasors, each of which is juxtaposed to the previous and rotated by 4ψ, where the first phasor is at angle of $4\Phi_o$. Moreover, the mean of the angle in V is $\overline{\{0+4\Phi_o, 4\psi+4\Phi_o, ..., (M-1)4\psi+4\Phi_o\}} = 4\Phi_o + (M-1)4\psi/2$, where $\overline{\{\}}$ denotes the mean of $\{\}$. We realize that both results also match even when only the frequency offset and the relative phase are considered. The component in V that is closest to this value of $4\Phi_o + (M-1)4\psi/2$ is always the central component, that is, the $(M+1)/2$ th component [49]. For this reason, the length of V should be an odd number, so that the angular component of its central component is represented with the least bias by the angle of the mean of V.

A sum of phasors with linearly increasing angle engenders a circular rotation in the Argand plane. In fact, adding the remaining frequency to the phase noise wraps the summation of phase noise represented by unitary phasors pointing East in the Argand plane into a circle or radius $R = 1/(2\tan(4\psi/2))$. To obtain the mean of the angles using the angle of the mean, the circular rotation cannot exceed a complete revolution. To honour this criterion, we state that the maximal revolution allowed is half a complete circle. This constraint is mathematically interpreted as $4 f_{\text{IF}} T(M-1) \leq 1/2$ [47]. This equation dictates the relation between the maximal frequency offset f_{IF} and the number of samples considered M. With our previous $M \approx 151$, this mean phase removal technique also works with a remaining intermediate frequency of $f_{\text{IF}} \approx 8$ MHz and increases for a smaller sum. This process is called Carrier Phase Estimation (CPE) [49].

3.2.10 – Constellation Derotation

Finally, the last process to apply to our signals is the final constellation derotation. The previous steps helped us getting rid of all the unwanted phases and leave us with a QPSK constellation unrotated, aligned with the axis of the Argand plane. This means that we end up with clouds of symbols around the points 1, *j*, -1 and -*j*. QPSK signals are modulated from a real signal of phase zero superimposed by an imaginary signal of phase $\pi/2$. Extracting the real and imaginary part of symbols wandering around these four points would not give us back the information we initially sent: we have to rotate the clouds of symbols by a value around $\pi/4$. To find the exact value, we find the mean of the angle deviation of each symbol with respect to its nearest point 1, *j*, -1 or -*j* and we finally rotate the symbols in the constellation by $\pi/4$ minus this mean angle deviation. We repeat for the signal of each polarization.

3.2.11– Symbol and Bit Decision

We decide which symbol we receive by looking at which quadrant of the Argand plane the symbol belong to. As an example, if we detect a symbol with a positive real component and a negative imaginary component, we decide that this symbol is $d_k = e^{-j\pi/4}$. To convert from symbols to bits, we use the Gray coding that allows most adjacent symbols to differ by a single bit, minimizing the number of bits in error for the same number of symbols in error. Fig. 16 depicts this slicer.

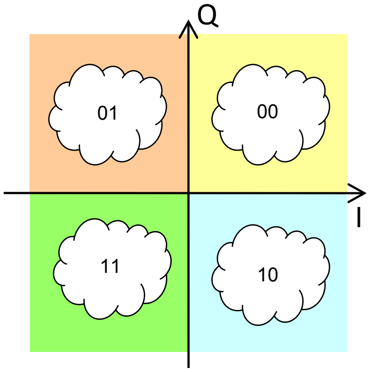

Fig. 16 – Symbol and Bit Decision Slicer using Gray Coding

Chapter 4 : Algorithms Assessment

In this chapter, we define which algorithms presented in Fig. 9 and detailed in Chapter 3 will be assessed and how. Moreover, we explain why some algorithms are not assessed.

The sequence of operations presented in the chapters above allows us to recover the symbols sent in a Dual-Polarization-QPSK transmission and consequently recover the bits of information transmitted. We will apply our algorithms to different optical launch powers and optical signal to noise ratios. Algorithms can be distinguished based on the final bit error rate (BER) they yield when applied to different sets acquisitions and on their computational complexity. Therefore, there are chances to obtain sequences of algorithms that give a lower BER, but at the cost of a higher complexity. The trade-offs of the two will we analysed. We will find the final BER first by comparing the symbol detected and the symbol sent. If the two don't match, the amount of bits in error will be counted based on a Gray coding for QAM, i.e., strictly adjacent symbols have only one bit different and symbols touching diagonally have two bits different. So, a symbol in error found in a strictly adjacent decision region counts for 1 bit in error and a symbol in error in a touching diagonally adjacent decision region counts for 2 errors.

We will analyze sequences of algorithms graphically though different kinds of plots. First of all, the BER that each sequence of algorithms gives will be plotted against variable OSNRs and that for different optical launch powers. Subsequently, we will use the latter plots to calculate the required OSNR (ROSNR) for a bit error rate of 3.8×10^{-3} as a function of the launch power. This type of plot is also used in the literature to compare the performance of different approaches [50]. We chose the BER value of 3.8×10^{-3} first of all because it is the limit for uncorrected errors available in production hardware, but also because forward error correction (FEC) delivers corrected $\text{BER} < 10^{-15}$ from raw BER $\leq 3.8\times10^{-3}$ [51]. This will allow us to compare all the sequences of algorithms on a single graph. With this graph in hand we will be able to ponder each performance curve with their relative computation requirements.

4.1 – The Computational Complexity and Bit Error Rate

Digital signal processing is a vast term meaning that a discretized input signal will be processed by means of elementary operations to output a modified signal. Most of the time, this process is done in order to remove impairments on the input signal and obtain a clearer signal. Any numerical process done to a signal boils down to applying sequences of multiplications and additions. We will use the sum of the required number of Real Multiplications (RM) and Real Additions (RA) to assess different numerical processing. The software we will use to operate on our discritized signals is MATLAB©. We decide to sum the numbers of RM and RA instead of evaluating them separately for simplicity of comparison. It would mean that we assume that it takes as much effort for a processor to process a real multiplication and a real addition.

The following table defines the general functions we will use and their respective required number of RA and RM. We consider that the input vector has a length of *N*. We use a simplified notation to identify “Real” with `R` and Complex with `C`. For example, the specification “`R with C`” for the process “Convolution” means that one vector utilized has real content and the other has complex. For the specials functions processing *N* complex numbers, we represent a single number *x* as $x = (a + jb)$. By “complex” number we mean that the number has both real and imaginary components. We assume that a purely real or a purely imaginary number are as sophisticated to process and are categorized under “real” number. We assume that a real division and real multiplication as well as real subtraction and real addition bear respectively the same computational intensity.

Table 1 - Computational Complexity of Numerical Operations Applied to a Vector of Length *N*

	Specification	# of real multiplications	# of real additions
Addition/Subtraction	R with R	0	*N*
	R with C	0	*N*
	C with C	0	2 *N*
Multiplication	R with R	*N*	0
	R with C	2 *N*	0
	C with C	4 *N*	2 *N*
Division	R with R	*N*	0
	R with C	6 *N*	*N*
	C with C	8 *N*	3 *N*
Mean	R input	1	*N*-1
	C input	2	2(*N*-1)
Convolution with a vector of length M	R with R	$NM-(M^2-1)/4$	$N(M-1)-(M^2-1)/4$
	R with C	$2NM-(M^2-1)/2$	$2N(M-1)-(M^2-1)/2$
	C with C	$4NM-(M^2-1)$	$4NM-(M^2-1)-2N$
FFT	R input	$N/2(\log_2 N-3)+2$	$N/2(3\log_2 N-5)+4$
	C input	$N(\log_2 N-3)+4$	$3N(\log_2 N-1)+4$
Special Cases for Complex Numbers	$\frac{x}{x^*}$	5 *N*	2 *N*
	$\lvert x\rvert^2$	2 *N*	1 *N*
	$\lvert x\rvert^4$	3 *N*	1 *N*
	x^2	3 *N*	1 *N*
	x^4	6 *N*	2 *N*

For example, a complex multiplication of $x=(a+jb)$ with $y=(c+jd)$ requires 4 RM and 2 RA, detailed as $(a+jb)\cdot(c+jd)=(ac-bd)+j(bc+ad)$. In the same vein, a complex division of x/y is assumed to require 8 RM and 3 RA in is detailed as $(a+jb)/(c+jd)=((ac+bd)+j(bc-ad))/(cc+dd)$. We only observe 6 direct RM, but we have to consider dividing the real and imaginary part of the numerator by the denominator, adding 2 extra RM.

For every convolution, we want the vector of length *N* to conserve its length in the process. We impose this criterion because we simply do not want to add components to the vector during convolution. For a convolution involving the vector to process of length *N*, named for simplicity *V*, with one of length *M*, we find that the number of RM and RA per element in *V* is respectively *M* and (*M*-1), except for the elements at the beginning and end of *V*. By computing this we find the numbers in the previous table.

For the Fast Fourier Transform, we assume that *N* is a power of 2. When $N = 2^m$ where *m* is an integer, we can use the split-radix or radix-2 Discrete Fourier Transform (DFT) decimation-in-time (DIT) computation simplification to decrease the required number of multiplication and addition. Discrete Fourier Transforms using fast algorithms like the radix-2 DIT are called Fast Fourier Transforms. The required number of real multiplications and real additions come from the text book referred here [52] and from the paper [53], references we recommend to the reader for further details on radix-2 DFT.

There is another way we can assess a complex multiplication in terms of real multiplications and additions. Let consider again that $x = (a + jb)$ and $y = (c + jd)$ and let's define the variables $k_1 = a(c + d)$, $k_2 = b(c - d)$ and $k_3 = d(a + b)$. We can easily show that $x \cdot y = (k_1 - k_3) + j(k_2 + k_3)$. Therefore, we multiply 2 complex numbers by computing 3 real multiplications and 5 real additions. Compared to the previous method where 4 RM and 2 RA are required, this technique trades 1 RM for 3 RA. In the event that the hardware uses fewer clock cycles to perform 3 additions than a single multiplication, we gain overall processing speed by using this technique [28]. For the particular operation of FFTs, one of the two terms in the complex multiplication is the twiddle factor at a power *m*, identified by $y = w_N^m = e^{-i2\pi m/N}$ for a FFT of length *N*. This twiddle factor can be precomputed before the FFT of x . In other words, $y = \cos(m\theta) + j\sin(m\theta)$ can be mapped in a lookup table to their counter parts $\cos(m\theta) + \sin(m\theta)$ and $\cos(m\theta) - \sin(m\theta)$, saving 2 real additions per complex multiplication during the FFT. Therefore, FFTs of complex sequences can require 3 RM and 3 RA per symbol, using the k_1, k_2 and k_3 variables [54]. This motivates our decision to assess the computational complexity by summing the RM and RA, as fast algorithms like the FFT realize a complex multiplication in a 3/3 or 4/2 real multiplication/addition approach, both giving a total of 6 operations.

For FFTs of real inputs, the number of multiplications needed is half of that for a complex input, because real input sequences have the property $X(k) = X^*(N-k)$ where * denotes conjugate and X is the Fourier transform of x of length N [52].

In our processings, we sometimes compute transcendental operations applied on vectors, element by element. These operations like $\sqrt{\vec{x}}$, $e^{\vec{x}}$ and $\operatorname{atan}(\vec{x})$ will not be taken into account in the calculus of the number of RM and RA because their computer implementation efficiency can only be accounted for by counting cycles for a convergence up to a specific error using for instance the Newton's method. Moreover, cycle counts vary with the computer architecture and most importantly with the Math Library used for processing the operation. We refer the reader to Intel©'s Vector Math Library (VML) for a table of performance and accuracy of all the functions included in their library [55]. It can be relevant to the reader to know that the math library used for processing our data is Intel® MKL (Math Kernel Library).

4.2 – Algorithms to Assess and Ways of Variation

In our procedure of assessing sequences of algorithms, we will not analyze every algorithms presented in Fig. 9. In this section we describe which algorithm will get assessed and which will not, as well as some explanations as why some algorithms are not appraised. Moreover, for the ones we will study, we will explain what parameters will be varied or what methods will be tested. To have a clear view of what algorithms will be studied, we reprint Fig. 9 where algorithms under study are circled in green and algorithm to leave aside are crossed out in red.

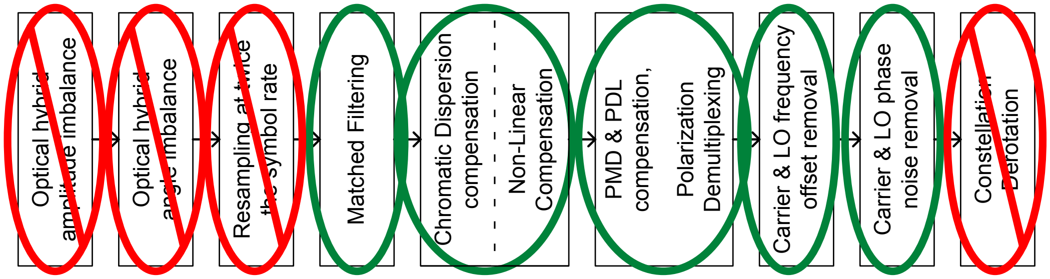

Fig. 17 – Algorithms to be Assessed

We will give ourselves the latitude to vary multiple parameters and use different approaches for each algorithm. It would be absolutely tedious to make them all vary linearly in a range and to map the complete ensemble of all the possible values and results they yield in a multidimensional plot. Instead, we compare a single parameter or method at a time, leaving all the others fixed and we study solely the impact of this parameter or method. We repeat for each parameter or method we want to assess.

To start with, the optical hybrid amplitude imbalance and angle imbalance will not be assessed because, as we saw in § 3.2.1 and § 3.2.2, they are impairments that are due to physical manufacturing challenges of making 90° optical hybrids. Moreover, they are fixed impairments that do not depend on the optical link at all. We described in these two subsections how to compensate for the hybrids imperfection and we will simply do so for every processing.

The process of resampling at twice the symbol rate will also not be studied. Resampling a sequence of acquisitions is a field of study itself where many different approaches and ways can be used, most especially for fractional resampling as we do. We decided not to investigate on ways to resample because in a real system, if one wants to process samples at twice at the baud rate, the ADCs will be set to sample at this specific rate. This is even truer in a high symbol rate system where it is the maximal sampling rate and the analog bandwidth of ADCs that are the bottlenecks for high baud rate optical transmissions employing a coherent receiver where we don't have the luxury to sample at high multiples of the symbol rate.

Matched filtering, explained in § 3.2.4, and chromatic dispersion, explained in § 3.2.5, are processes that will be investigated. We discuss these two processes in the same paragraph because they can be applied to the signal in the same way, both acting as regular filters applied either sequentially or simultaneously. We will try to eliminate chromatic dispersion and to match filter (MF) by operating both process in the time domain and in the frequency domain representation. When both processes are applied in the same domain, they will be applied simultaneously using a single filter. Therefore we will operate in four different ways: 1) apply simultaneously MF and CD^{-1} in the frequency domain, 2) apply independently MF in frequency and CD^{-1} in time, 3) apply independently MF in time and CD^{-1} in frequency and finally 4) apply simultaneously MF and CD^{-1} in the time domain. We know from mathematics that the convolution of three functions, f, g and h, can be applied in any sequence. If f is our function of interest and g and h are the MF and CD^{-1} time responses respectively, we can apply the two filters in a single convolution as $f \otimes (g \otimes h)$. This possibly reduces the computational complexity of the time domain approach while providing the same result as for separate filter application. The same simplification is done for the multiplication of filters in the frequency domain. We will differentiate each 4 cases by observing the impact on the final BER and their total number of required real multiplications and real additions.

Nonlinear phase shifts will not always be taken into account and therefore will not always be assessed. However, NL mitigation will be through the method described in § 3.2.6 when applied. Its total computational complexity will be assessed by summing the total number of RM and RA using the numbers in Table 1. As chromatic dispersion compensation is applied within the algorithm of nonlinear compensation, its complexity will be taken into account within the NL compensation process when activated and as a standalone algorithm otherwise. Of course, applying nonlinear compensation will also affect the final BER that we will monitor. We will vary the step size parameters within the NL mitigation algorithm. The Split-Step-Fourier-Method we use works well for nonlinear compensation but is absolutely not computationally efficient. Our goal is not to thoroughly study different digital NL compensation approaches, but to use only the SSFM method and to vary its computer complexity, most probably altering the final BER, by varying the propagation step size Δz. However, efficient digital mitigation of nonlinear effects is an attractive and promising research topic [3]. We will not only study the impact of changing Δz when we activate the nonlinear compensation algorithm but also compare results with and without NL mitigation. The step size we will take for the SSFM method will be of 5, 10 and 20 km.

The process that compensates for polarization mode dispersion and polarization dependent loss, and that demultiplexes polarization multiplexed signals will be thoroughly studied. These processes, explained in § 3.2.7, are crucial for a transmission scheme like the one we study, i.e., Dual Polarization-QPSK. The three dimensional MIMO matrix $\mathbf{H}$ introduced in Eqs. (30) and (31) does at the same time PMD and PDL compensation and polarization demultiplexing. The parameters we will have the freedom to vary in this Constant Modulus Algorithm equalizer are 1) the third dimension of $\mathbf{H}$, i.e., its length, 2) the method for updating $\mathbf{H}$ and also 3) the impact of the strength of the adaptive parameter μ in Eq. (31). All the three above variations will influence the final BER, but only the method of adaption of $\mathbf{H}$ and its length will influence the process's computational complexity. For the method of adaptation of $\mathbf{H}$, we want to know if it is better to update continuously, once every symbol, or to update for N symbols for filter adaptation and then apply a fixed matrix $\mathbf{H}$ for a duration of $M-N$ symbols and repeat every M symbols. The latter is obviously less computationally intense than always updating $\mathbf{H}$. Additionally, increasing the length will let the algorithm take more neighbouring bits into account for processing, assuredly requiring more computations per sample, but could be detrimental for very noisy signals. Finally, the adaptive parameter μ will be tested for the four values of 0.001, 0.002, 0.003 and 0.005

For the carrier and LO frequency offset removal, we will study the two methods described in § 3.2.8, namely the time domain and the frequency domain approaches. The sum of the total required RM and RA and each method's resulting BER will be used to assess the two methods.

Finally, the carrier and LO phase noise removal (§ 3.2.9) will be assessed by varying the amount of elements to take in the computation of the mean of phasors. This will impact solely the final BER. The computational complexity doesn't change by changing the number of element accounted for in the mean because of the way we process the moving mean. For a simple explanation, our process of phase noise removal can be seen as a moving average window, repeatedly moving by one sample and applying the output of a filter to a single element. The way we compute the sum of elements inside a new shifted window is simply by subtracting the element that left the window form the previous sum and adding the newly included element in the sum. With this efficient technique, the length of the window does not change the computational complexity. Only the sum of the initial M elements has to be computed on system startup and will be neglected in the calculation. The computational complexity of phase noise removal can already be accounted for as being two required complex additions per symbol. We use summation instead of mean because the angle of the mean equals that of the sum.

Chapter 5 : Experimental Setup

In this chapter, we will present the test bed we worked on to collect the experimental data and unfold the parameter space we worked with. The optical test bed is depicted in the block diagram below.

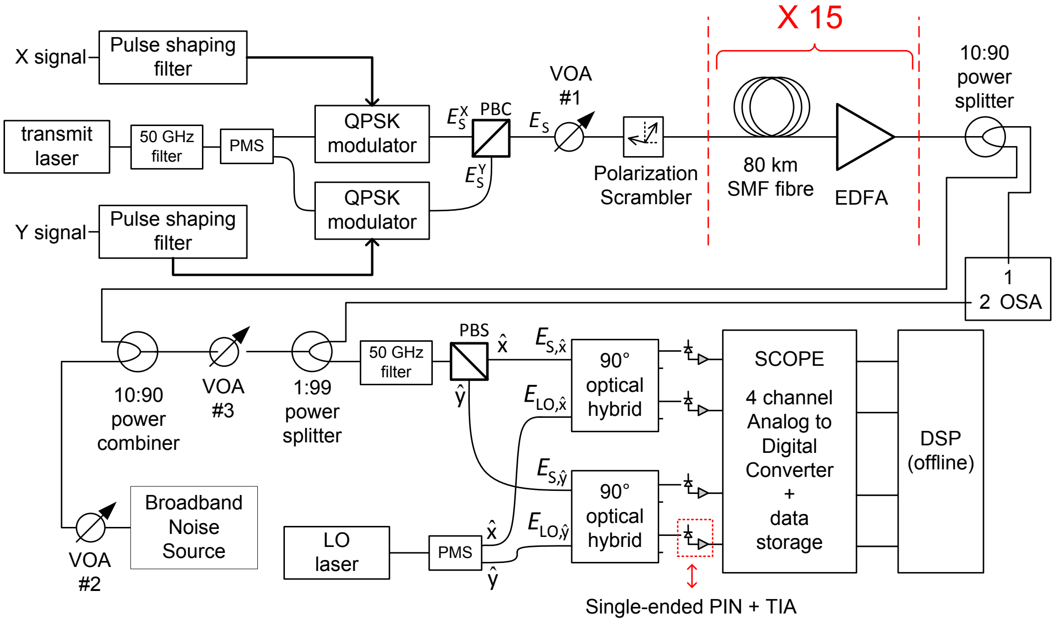

Fig. 18 – Block Schematic of Optical Test Bed

The experiments were realized at Nortel Networks$^{©}$ in Ottawa, CANADA, in December 2009, in the Metro Ethernet Networking Solutions laboratory. Some of the equipments we used are the following:

- The transmit and LO lasers: Emcore$^{©}$ ITLA TTX1994x
- Optical fibre: Corning$^{©}$ SMF-28$^{\text{TM}}$ (ITU-T G.652 compliant)
- Single-ended PIN + TIA: Discovery Semiconductors$^{©}$ DSC-R401HG
- Scope: Tektronix$^{©}$ DPO71604
- Polarization Scrambler : Agilent$^{©}$ 11896A Polarization Controller

The “X signal” and “Y signal” are repeated known De Bruijn sequences of length

2^{14} varying at a speed of 10 Gsymbols/sec. The transmit laser emits at $\lambda = 1547.715$ nm with a 3 dB linewidth smaller than 100 KHz. The "LO laser" is tuned to emit within 200 MHz of the transmit laser and has the same linewidth. The other parts in the setup are not mentioned either because they are proprietary Nortel©'s parts or are generic, commonly used optical parts. Again, the software utilized to process offline the acquired data is MATLAB©.

The first parameter in our parameter space is the pulse type. We used two different types of pulse shaping filter at the transmitter: the Root-Raised Cosine filter (Eqs. (25), (26)) with roll-off factor $\alpha = 1$ and another pulse shape developed by Ph.D. candidate Benoît Châtelain at McGill University, Montreal, CANADA [56, 57]. This optimized pulse shape is intended to mitigate the nonlinear effects when propagating in an optical fibre. We will refer to the first pulse as the "RRC" pulse and to the optimized pulse as the "OPT" pulse. Both pulses occupy the same bandwidth, i.e., for a symbol duration of $T = 100$ ps they occupy a single-side bandwidth of $W = 1/T = 10$ GHz or a full width bandwidth of $2/T = 20$ GHz (see § 3.2.4). The pulse shaping filter are made to be applied in a matched filtering way, i.e., that the same filter is applied at the transmitter and receiver. Consequently the MF at the receiver will be the same as the pulse shaping filter.

For each pulse shape we vary the launch power P_{launch} of the signal as it enters each fibre span through the variable optical attenuator VOA #1 and the 15 Erbium Doped Fibre Amplifiers (EDFA) such that the total signal power+in-band noise power after each span of 80 kilometres is brought back to P_{launch}. This launch power variation is our second parameter in the parameter space. The power of the signal launched was varied to the values of -4, -2, 0, 2, 3, 4, 5 and 6 dBm and the total propagated distance is 1200 km. As a reminder, dBm and milliWatts (mW) are power related as $[\text{dBm}] = 10 \cdot \log_{10}([\text{mW}])$. The previous power values are accounting for the total optical power entering the optical fibre, meaning that for a polarization multiplexed signal, P_{launch} is the sum of the powers of both polarizations. A single carrier at wavelength of $\lambda_o = 1547.715$ nm was used to transport the binary stream. Two idle wavelengths far from λ_o, located at the extremity of the gain spectrum of the EDFAs were used to flatten the EDFA gain around λ_o, called gain balancing, and are considered not influent on λ_o.

Moreover, for each launch power for each pulse shape, the OSNR was varied at the receiver using a broadband source. The OSNR, our third and last parameter, was changed by varying the noise floor through VOA #2 in the previous figure. The OSNR was varied from around 6 dB to around 18 dB by incremental steps of roughly 1 dB. The optical signal to noise ratio is found using port 2 of the optical spectrum analyzer (OSA) with a resolution bandwidth much higher than the useful signal's total bandwidth. As the total two-sided bandwidth of our signal is 20 GHz (0.16 nm around 1547.715 nm), we choose a resolution bandwidth of 0.5 nm, equivalent to 75 GHz. With an OSA of finite resolution of 0.003 nm, setting the resolution bandwidth to 0.5 nm lets the OSA output window averages of approximately 167 spectral powers, applied for the entire frequency display of the OSA. As an example, we plotted in Fig. 19 an acquired optical spectrum at the receiver after 1200 km with a resolution bandwidth of 0.5 nm for which the OSNR in 0.5 nm is found to be 7 dB or of a ratio of 5. The OSNR in 0.5 nm and in 0.1 nm are known to be dictated by Eqs. (34) and (35). The middle green dot is a linear interpolation of the power of the noise residing inside the bandwidth of

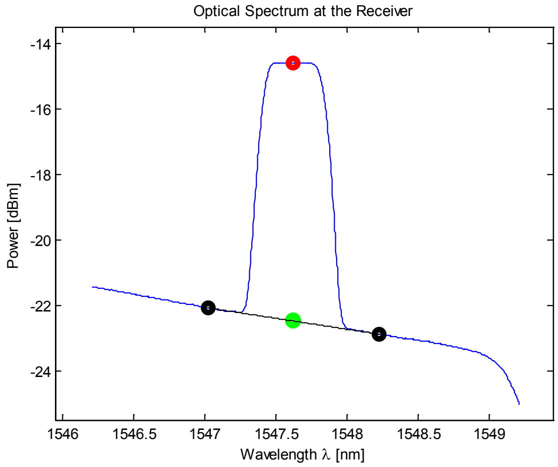

Fig. 19 – Optical Spectrum at the receiver: Resolution bandwidth of 0.5 nm

$$OSNR_{0.5\text{nm}} = \frac{P_{\text{SIG+NOISE}} - P_{\text{NOISE}}}{P_{\text{NOISE}}} = \frac{\text{🔴} - \text{🟢}}{\text{🟢}} \tag{34}$$

$$OSNR_{0.1\text{nm}} = OSNR_{0.5\text{nm}} + 10\log\left(\frac{0.5}{0.1}\right) \tag{35}$$

the signal. By calculating the OSNR in 0.5 nm, we take into account all the optical noise in 0.5 nm. Eq. (35) allows us to find the in OSNR in 0.1 nm by simply assuming that there is 5 times less noise in a bandwidth of 0.1 nm than in 0.5 nm. The black dots serve as the extremes for linear interpolation and are assumed to be located where there is solely noise. (35)

The power ratio between the Local Oscillator P_{LO} and the signal P_{SIG} at the receiver, before entering the Dual-Polarization 90° Optical Hybrid (see Fig. 4), was kept at around $P_{\text{LO}}/P_{\text{SIG}} = 100$. We chose this value, used in the literature, because high local-oscillator-to-signal power ratio minimises the distortion caused by the direct square-law detection of photodetectors. Such distortion may severely degrade the performance of DSP-based CD/PDM compensation and polarization recovery [58, 59]. The $P_{\text{LO}}/P_{\text{SIG}}$ ratio was kept constant using VOA #3. It is worth noting that the input polarisation state of the signal was not controlled, and an arbitrary mix of each transmitted polarisation state was incident on the photodetectors [58].

For each pulse shape, launch power and OSNR, we collected 10 million samples at a rate of 50 Gsamples per second, giving a collection time of roughly 0.2 millisecond. As our symbol rate was fixed at 10 Gsymbols per second, each acquisition encompassed 2 million symbols' worth of time. We decided to process for only roughly one fourth of this time, or for exactly $2^{19} = 524288$ symbols' worth of time, because otherwise the required processing time was too long. In fact, as we processing at 2 samples per symbol, 2^{20} samples we used for each of the 4 channels, making a total of 4.2 million samples to proceed for every sequence of algorithms to study.

Chapter 6 : Analysis of Processes and Results

In this chapter we present the BER and the total amount of real multiplications and real additions that all DSP processes yield when applied after the analog to digital conversion in the optical coherent receiver. We compare the results for all pulses, launch powers and OSNRs for a single parameter or method under study at a time, while leaving the other parameters fixed. This way to present results allows us to point out the impact of a single approach or of tuning a parameter.

We compare 10 different parameters or methods in order to give us a broad view of the impact of several aspects in the digital process of a coherent receiver. The 10 comparisons are the following:

1. Vary the length of $\mathbf{H}$ in Eqs. (30) and (31) in the polarization demultiplexing process without any nonlinear compensation: 9 and 5 taps
2. Change the method of adaptation of $\mathbf{H}$: always adaptive versus adaptive for 2048 symbols and fixed for 6144, repeated every 8192 symbols
3. Include or exclude the nonlinear impairment compensation through the SSFM method using a length of $\mathbf{H}$ of 5 taps
4. Vary the length of $\mathbf{H}$ in the polarization demultiplexing process when nonlinearities are compensated: length of 9 versus length of 5 taps
5. Compare all the possible methods to match filter and to apply chromatic dispersion compensation either in time or in frequency domain. The following summarizes the possible methods:

	MF	CD^{-1}
in Frequency	A B	A C
in Time	C D	B D

where the four different approaches are letter tagged A, B, C, and D. For instance, process B applies the match filter in the frequency domain and the CD compensation (CD^{-1}) independently in the time domain. Processes A and D are applied simultaneously as they are applied in the same domain.

6. Vary the duration of the fixed coefficients in **H** when adaptive for 2048 symbols: fixed for 6144 and repeated every 8192 symbol or fixed for 18432 and repeated every 20480
7. Vary the strength of the step size parameter μ in the adaptation of $\mathbf{H}$:
   $\mu = 0.001,\ 0.002,\ 0.003,\ \text{or}\ 0.005$
8. Vary the amount of elements to take in the computation of the mean in the carrier phase estimation: 71 versus 101 elements
9. Change the method to remove the carrier frequency offset: using the frequency domain versus the time domain approach
10. Vary the propagation distance steps Δz in the SSFM method:
    $\Delta z = 5\ \text{km},\ 10\ \text{km}\ \text{or}\ 20\ \text{km}$

To compare all our results, we will plot "BER vs OSNR in 0.1 nm" showing results for a specific type of pulse and a specific method or parameter under study. These plots will show the results for each launch powers. Additionally, in order to synthesise the results for the parameter under study, we will construct a "Required OSNR vs Launch power" figure obtained by finding the points where all the curves in the previous "BER vs OSNR" plots cross the BER threshold of 3.8×10^{-3}. These points are circled in black in these plots.

6.1 – Study of Comparison 1

For comparison #1, we compare the impact on the BER against OSNR and on the computational complexity when we vary the number of taps in the polarization demultiplexing process from 9 to 5. The plots on next page are detailed as follow:

Comparison 1 Figures

Length of **H** is 9:

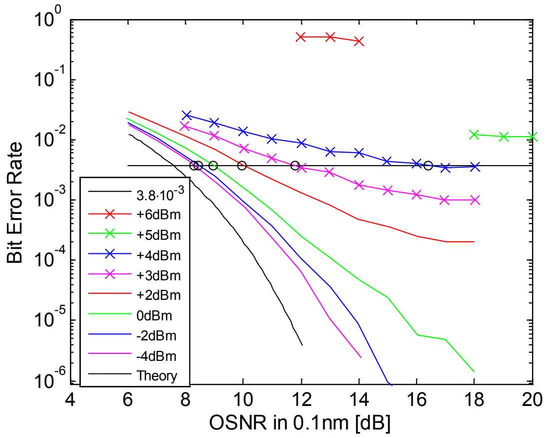

Fig. 20 – 1) BER vs OSNR: RRC - H has 9 taps

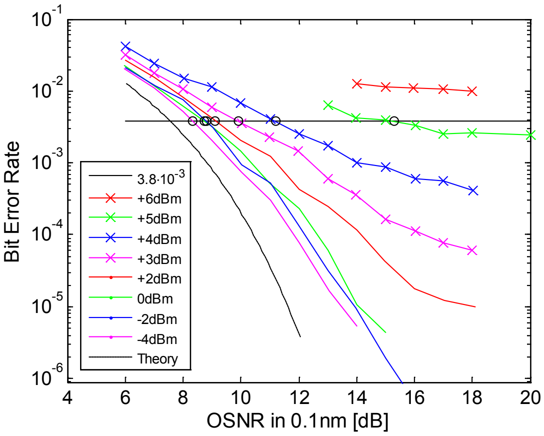

Fig. 21 – 1) BER vs OSNR: OPT - H has 9 taps

Length of **H** is 5 :

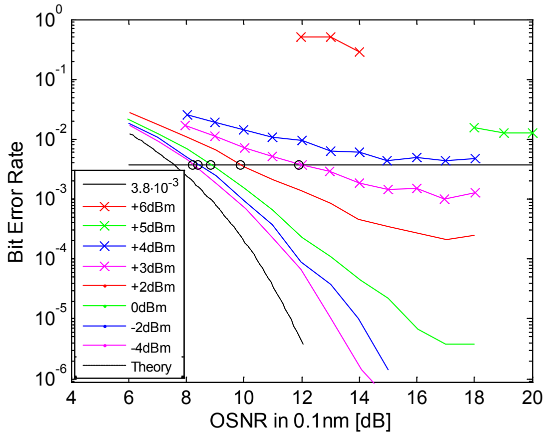

Fig. 22 – 1) BER vs OSNR: RRC - H has 5 taps

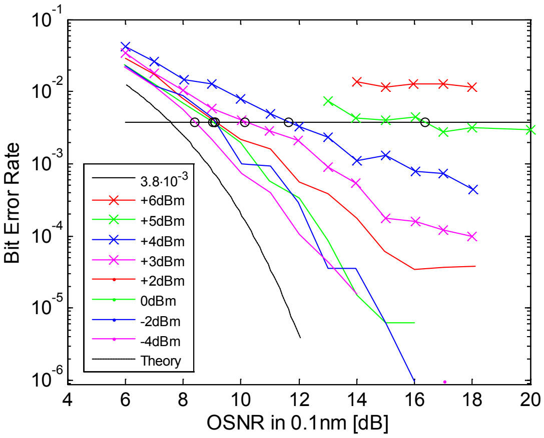

Fig. 23 – 1) BER vs OSNR: OPT - H has 5 taps

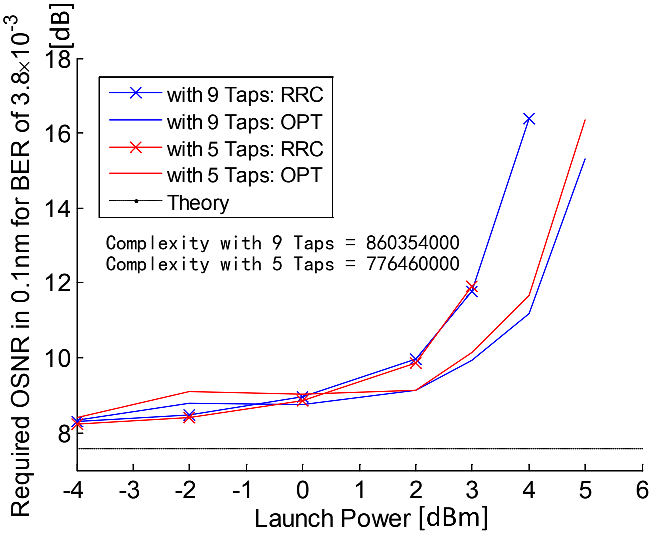

Fig. 24 – 1) ROSNR vs Launch Power : RRC & OPT pulses: Length H of 5 and 9

plots in the first row are results for both the RRC and the OPT pulses when 9 taps are used, plots in the second row are results when 5 taps are used for both pulses and the final third row shows the comparison of the computational complexity between 9 and 5 taps along with the required OSNR in 0.1 nm for a BER of 3.8×10^{-3} against different launch powers. We observe that for all the top 4 plots, the BER is always lower when the OPT type of pulses is used, as predicted by Ph.D. candidate Benoît Châtelain [56, 57]. If we compare the top left plots looking only at RRC pulses, we realize that there's practically no difference between using 9 or 5 taps: a result that is confirmed by the ROSNR vs Launch Power plot by the quasi-superimposed × marked two solid lines. For a numerical comparison, the RRC pulse between –4 and +3 dBm using 5 taps has, on average, a better performance of roughly 0.033 dB. Surprisingly enough, the inverse happens when the OPT pulse is used: over the same launch power range, the 9-tap length always gives a better performance, by 0.175 dB on average. It is hard to explain why 5 taps work better for RRC and 9 taps for OPT, but as the variation is quite low, we can make the hypothesis that the performances are very similar for longer, real time processing.

We equally observe that using only 5 taps lowers the final complexity by roughly 10%. This makes sense as the polarization demultiplexing process acts as a convolution of input signals with short vectors, in our case either of length 9 of 5. As we previously discussed, convoluting by a shorter vector inherently requires less computations. Another observation to be made comparing the two types of pulses is that at high powers, starting at +2 dBm and above, the OPT pulse outperforms the regular RRC pulse in terms of the BER it yields. We confirm this by looking at figures in the same row, where pulses RRC and OPT receive the exact same processing from end to end. Curves of the same colour in the last ROSNR vs Launch Power figure concur with this observation. For example, at +4 dBm of launch power, OPT requires an OSNR that is 5.2 dB lower than that of the RRC pulses to achieve a BER of 3.8×10^{-3} when both use 9 taps; an improvement mainly due to the OPT pulse receiving less SPM effects.

Therefore, we conclude that for RRC pulses, it is simply advantageous, both in terms of system performance and computationally, to use 5 taps instead of 9. When OPT pulses are used at the transmitter, however, the performance improvement in the ROSNR, up to 1.05 dB at +5 dBm of launch power, is most probably worth the 10% increase in the total computer complexity. For sure, the margin of our overall receiver dictates the final choice for OPT pulses

6.2 – Study of Comparison 2

The second study allows us to compare the impact of changing the method of adaptation of the h_{ij} coefficients of the $\mathbf{H}$ matrix in time. We study two different approaches. In the first one, we continuously adapt the h_{ij} coefficients at every symbol whereas in the second method, we adapt h_{ij}'s for 2048 symbols then keep them fixed for $8192-2048=6144$ symbols and repeat every 8192 symbols. For the record, we used a vector length of 5 taps for the four $\vec{h}_{ij}$ in both types of adaptation. We observe in the bottom figure on next page that the reduction of complexity is very minor when the coefficients are updated only 2048 times every 8192 symbols. A reduction of barely 2.5% of the total computer complexity (CC) is achieved by updating one fourth of the time. However, by comparing the solid lines together and the $\times$-marked lines together in this plot, we realize that this computation improvement is obtained at practically no cost as the solid and the $\times$ curves respectively overlay almost perfectly when we omit a single experimental point for the OPT pulse at +3 dBm in the 2048/6144 case. We therefore conclude that it is not needed to continuously adapt the coefficients of the $\mathbf{H}$ matrix in the polarization demultiplexing process. It proves that the variation of the principal states of polarization in the fibre is done on a scale much larger than $8192 \times 100\text{ ps} \approx 1\,\mu\text{s}$. When we compare results from the RRC pulse with those of the OPT pulse processed the same way, we can solely conclude what was already pointed out in the analysis of the first process, that is, Châtelain's OPT pulses render a much lower BER at high launch powers. In fact, for a launch power of +3 dBm, the ROSNR is improved by 1.8 dB in the continuously

Comparison 2 Figures

Always adapting:

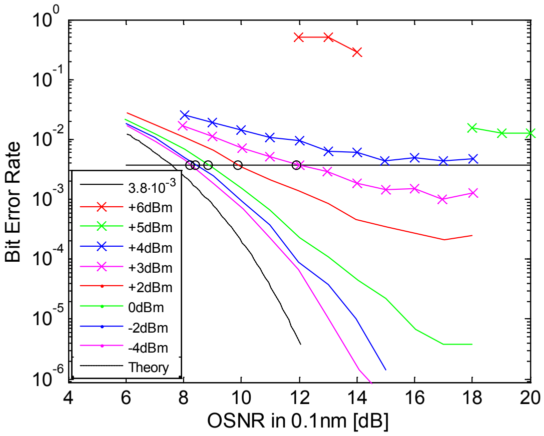

Fig. 25 – 2) BER vs OSNR: RRC - always adapting

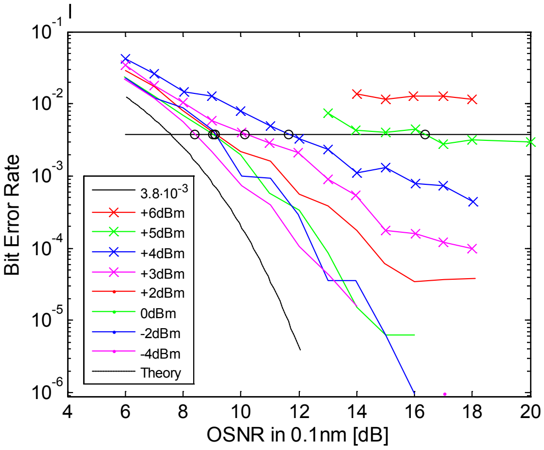

Fig. 26 – 2) BER vs OSNR: OPT - always adapting

Adapting for 2048 and fixed for 6144 :

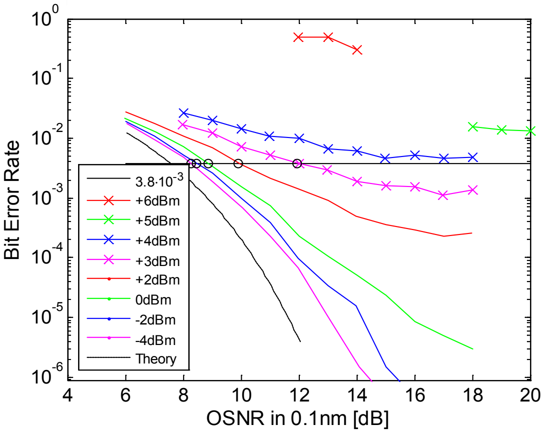

Fig. 27 – 2) BER vs OSNR: RRC - 2048/6144

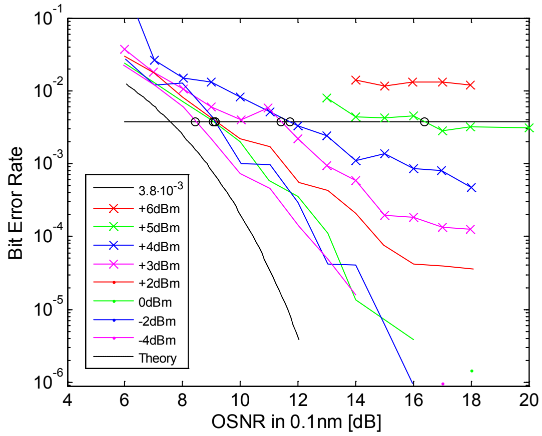

Fig. 28 – 2) BER vs OSNR: OPT - 2048/6144

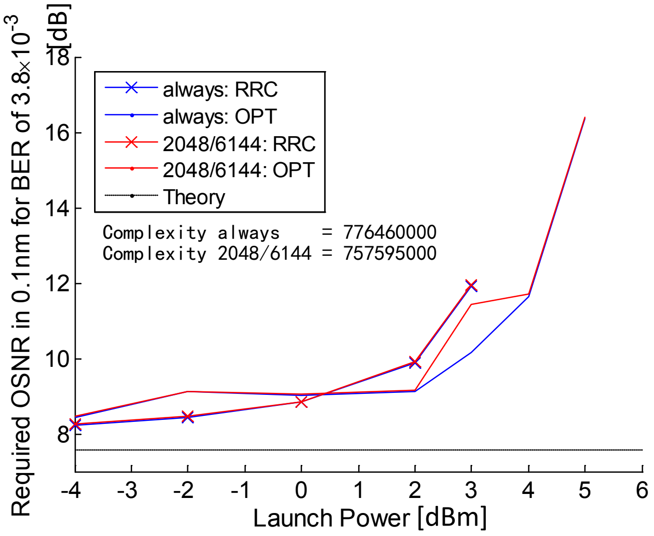

Fig. 29 – 2) ROSNR vs Launch Power : RRC & OPT pulses - always and 2048/6144 adapt/fixed

adaptive case. This enormous improvement solely due to the shape of the pulse, imprinted at the transmitter to send down the fibre is a gigantic step forward in the research of ways to combat nonlinear impairments in an optical system. It is worth to say that this observation is valid for the first two comparison studies above and that neither of those include nonlinear effect mitigation.

6.3– Study of Comparison 3

The third study allows us to compare the impact of including nonlinear mitigation in the digital signal process. We compare two different processing schemes. In the first one, we do not take into account any nonlinear mitigation technique and remove chromatic dispersion as a regular linear process in lump fashion in the frequency domain. We compare the results that this technique yields to a second approach where nonlinearities are mitigated using the Split-Step Fourier method. In this second technique, the beam propagation method that consists the SSFM allows the back propagation of the received optical field from the receiver to the transmitter. This technique, explained in §3.2.6, doesn't compensate for chromatic dispersion all at once in the frequency domain as we do in the first approach but use small propagation steps, each of which compensates for its small chromatic dispersion as well as for nonlinearities occurring within this small distance. The propagation step size utilized for this comparison is 5 km and consequently the NL small step process is repeated 1200/5 = 240 times to backpropagate the entire distance. The top 2 plots are BER vs OSNR results for both types of pulses when no NL mitigation is done and CD is bulk compensated in the frequency domain. The 2 plots in the middle row are results for both pulses when the SSFM is activated and the last plot shows the ROSNR vs Launch Power for both approaches, for both pulse types. The improvement in the system performance when nonlinearities are mitigated is tremendous. If we look at BERs using a regular pulse shape like the RRC pulse, located on the left-hand side of next page, we realize that the curves for all the different launch powers are pushed down. This is even more apparent at high launch powers of +2 dBm and above, whereas

Comparison 3 Figures

Without compensation of nonlinearities (5-tap CMA):

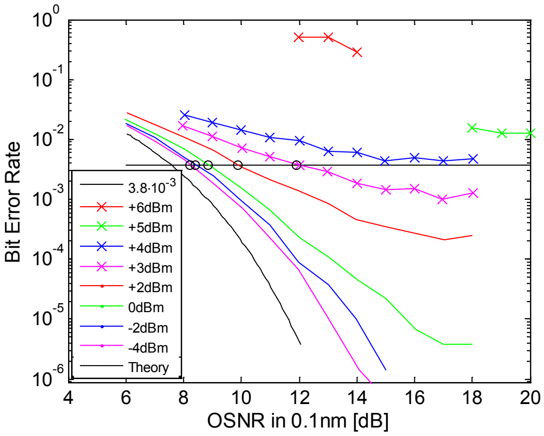

Fig. 30 – 3) BER vs OSNR: RRC-NL off/5-tap CMA

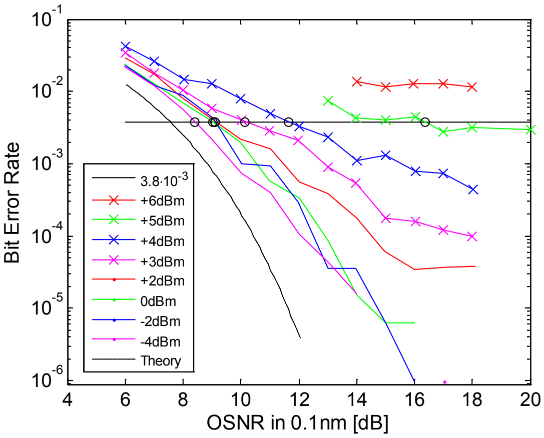

Fig. 31 – 3) BER vs OSNR: OPT-NL off/5-tap CMA

With compensation of nonlinearities (5-tap CMA):

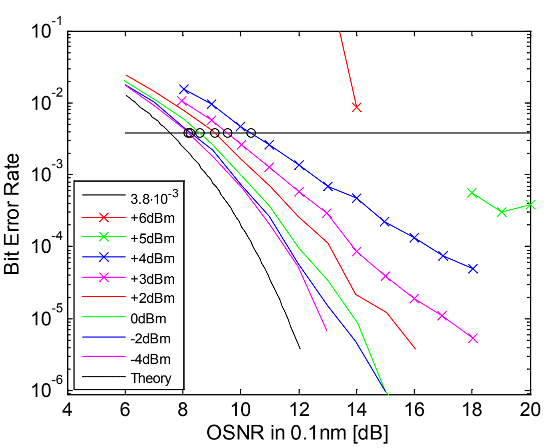

Fig. 32 – 3) BER vs OSNR: RRC-NL on/5-tap CMA

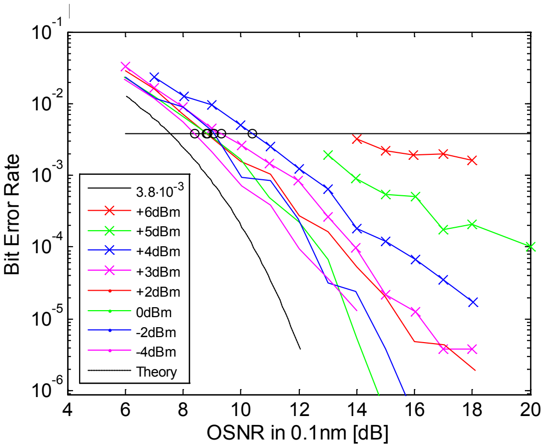

Fig. 33 – 3) BER vs OSNR: OPT-NL on/5-tap CMA

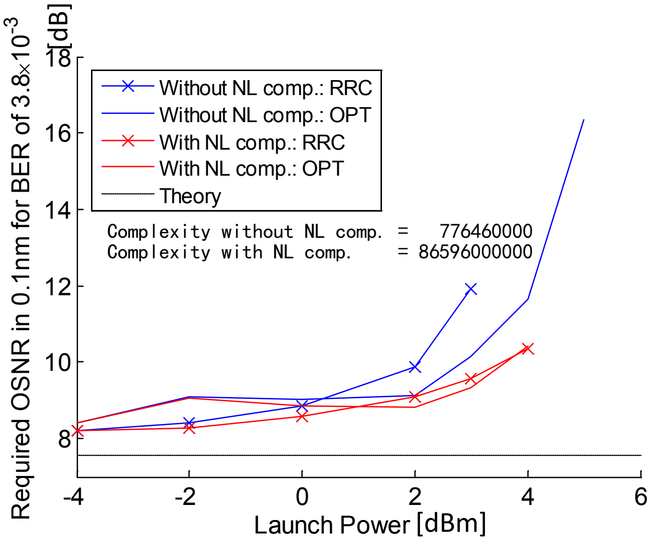

Fig. 34 – 3) ROSNR vs Launch Power: RRC & OPT pulses - with/without NL mit. with 5-tap CMA

the system improvement is not as significant at low powers of –4 or -2 dBm. Accordingly, we clearly observe a down push of the RRC curves in the bottom plot when NL mitigation is on. When we look at the results when Châtelain's OPT pulses are used, we observe that the system improvement is still present but not as strong as for RRC pulses. Curves are indeed pushed down, in both the BER vs OSNR and the ROSNR vs Launch Power plots for the OPT pulses but less substantially. This makes senses as the OPT pulses were conceived to receive less nonlinear impairments as they propagate down a fibre.

One important thing to observe is that the natural system performance benefit of using OPT pulses compared to RRC pulses is not that evident when NL impairments are reduced. The two plots in the second row agree with this observation as curves of launch powers from –4 to +4 dBm roughly lay around the same locations when comparing RRC to OTP pulses. To quantify system improvement for both the RRC and OPT pulse types, the required OSNR for $\mathrm{BER}=3.8\times10^{-3}$ for a launch power of +3 dBm is lowered by more than 2.3 dB for RRC pulses but only by 0.8 dB for OPT pulses. This shows not only how beneficial the inclusion of NL mitigation is to the overall error rate but also that if NL compensation is to be done at the receiver, the use of OPT pulses is not as advantageous. However, on the other hand, if the receiver does not compensate for NL effects digitally, the use of OPT pulses helps a lot to combat nonlinear impairments.

Per contra, this major improvement is not achieved for free. By looking at the total number of real multiplications and additions for the entire digital signal processes of both cases, we realize that the inclusion of NL compensation increases the number by more than 110 times that when no NL is accounted for. This means that not only much more processing power is required when NL compensation is activated, but practically all of it goes to the sole purpose of compensating NL effects. Therefore, under these conditions, the cost is seriously too much. Nevertheless, now that we know how advantageous compensating for

NL effects is, we realize how important investigating in other less computationally intense methods for NL effects reduction is. Consequently, we will process and study in later pages the results for step sizes bigger than 5 km. We can predict in advance that using fewer steps to backpropagate the same distance in the NL mitigation process will substantially lower the total complexity but the study will assess the tradeoffs of such coarser NL processing.

6.4 – Study of Comparison 4

For the fourth comparison, we confront face to face two methods that mitigate nonlinear impairments but that are differentiated by the number of taps utilized in the polarization demultiplexing process. The first method uses 9 taps while the second uses only 5 taps in the CMA subprocess. The results of these two processes are shown below. For this study it is more relevant to compare the results of RRC pulses together and OPT pulses together. When RRC pulses are utilized, we observe that the use of 5 taps or 9 taps in the CMA subprocess practically doesn't change the final BERs. By looking at figures on the left-hand side of next page, we observe that, to some extent, the results for the various launch powers practically overlay. For the single case of very high launch power of +6 dBm, the process involving 5 CMA taps is unable to converge for low OSNRs of 12 and 13 dB because of the high level of noisiness in the signal at the receiver, whereas the one involving a CMA that includes more neighbouring samples to extract data can actually converges and deal with such a signal. As the two methods give equal system performance, we can look at their complexity to differentiate them. We realize that, as expected, the method including 9 CMA taps requires more computations than the one using only 5 CMA taps. This result concur with what we observed in *Comparison 1*, but this time instead of a total complexity increase of 10% due to the longer vector length from 5 to 9, this same tap number increase turns into a little relative 0.1% increase in the total complexity when nonlinear compensation is included. This gives us, again, a sense of how NL compensation in computationally intense. Moreover,

Comparison 4 Figures

With compensation of nonlinearities using 9-tap CMA:

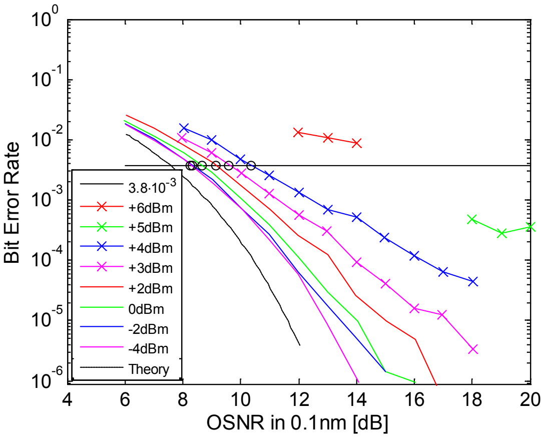

Fig. 35 – 4) BER vs OSNR:RRC - 9 tap CMA, NL on

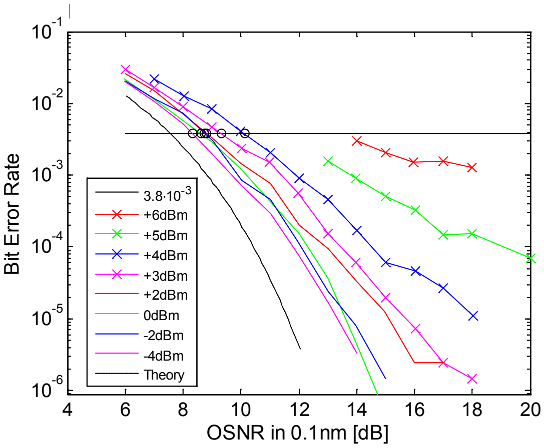

Fig. 36 – 4) BER vs OSNR:OPT - 9 tap CMA, NL on

With compensation of nonlinearities using 5-tap CMA:

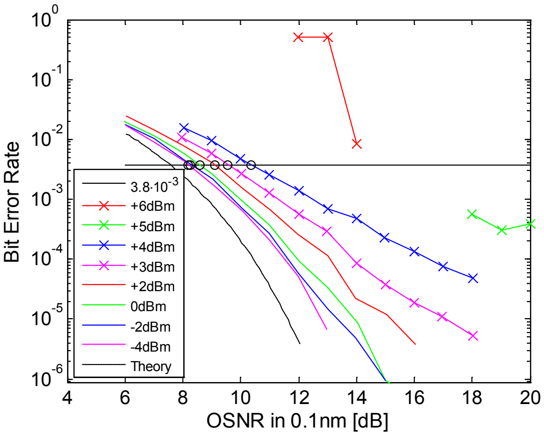

Fig. 37 – 4) BER vs OSNR:RRC - 5 tap CMA, NL on

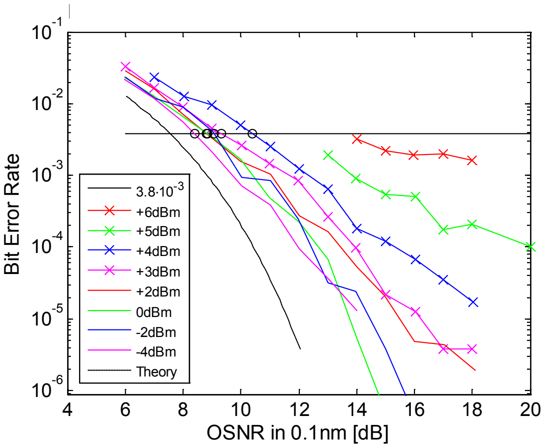

Fig. 38 – 4) BER vs OSNR:OPT - 5 tap CMA, NL on

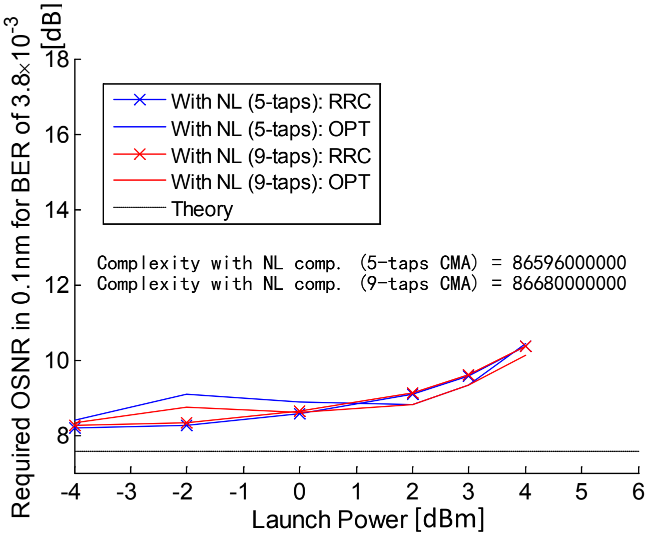

Fig. 39 – 3) ROSNR vs Launch Power: RRC & OPT pulses – 5 and 9-tap CMA with NL mitigation

Comparison 3 informed us of a rough 110 times increase in the CC when NL compensation is included, which roughly concurs with the 10%/0.1% ratio discovered in this fourth comparison, proving that NL mitigation takes over all the processing power. The nearly equal system performance with the RRC pulses is verified by looking at the $\times$- marked curves on the bottom plot on next page.

For the case using the OPT pulses, we realize that the system performance is slightly improved by using 9 taps instead of 5 in the CMA when NL is compensated. Compared to results in *Comparison 1* where NL was not compensated, the small improvement of, for example, 0.28 dB at +4 dB of launch power is not a lot less than the one without NL compensation being 0.46 dB. If we look at OPT curves only in the ROSNR vs Launch Power plots of *Comparison 4* and *Comparison 1*, we observe that they follow the same course, considering that the experimental +5 dB and +6 dB curves of BER vs OSNR never cross the 3.8×10^{-3} BER threshold when NL is compensated because we decided to stop acquiring at OSNRs of 13 and 14 dB respectively, as our initial quick processing of the data would not converge at lower OSNRs. Finally, the ROSNR vs Launch Power plot tells us that from launch powers of 1 dBm and above, the two types of pulse give very similar results, all meeting the BER threshold within an OSNR range of ± 0.16 dB.

6.5 – Study of Comparison 5

In this section we will analyze the impact of the method used to match filter and remove chromatic dispersion. As explained in sections §3.2.4 and §3.2.5, these two subprocesses are linear filters that have a representation in both the time and the frequency domain. Consequently, we are interested in knowing the impacts on the final BER but most importantly on the total computational complexity of each filter when applied using either domains. Therefore, we will look at results when A) both the matched filtering and the removal of the chromatic dispersion is done simultaneously in the frequency domain, B) the match filtering is initially done in the frequency domain followed the temporal filter removing chromatic dispersion, C) the matched filter is applied in the time domain followed by the chromatic dispersion removal in the frequency domain and finally D) the matched filter and the chromatic dispersion compensation are applied simultaneously in the time domain. When frequency domain equalization is used, the entire 2^{19} symbols' worth of time acquisition is used to do the FFT and therefore the entire length of the input signal gets filtered all at once. Additionally, for each time domain filtering of chromatic dispersion, the vector used for convolution with the useful signals always has full length, i.e., a length that allows compensation for the entire bandwidth of the signal while avoiding aliasing. For our configuration where $\beta_2 = -21.87\,\mathrm{ps}^2/\mathrm{km}$, $L = 1200\,\mathrm{km}$ and the signal bandwidth goes up to 10 GHz at a baud rate of 10 Gbaud/s, this number of taps is 61 [43]. Of course, we are aware that the computational complexity can be lowered by using a convoluter of a smaller length, but such an approach engenders some penalty as not all the frequencies are compensated and we decided not to vary this parameter. Moreover, time domain matched filtering is always applied using a convoluter of length 33, either for RRC or OPT pulses. Finally, for case D), the time domain convoluter allowing simultaneous removal of CD and application of MF always has a length of 101, again permitting full CD compensation.

As 4 methods have to be studied, we decided to present the results for RRC pulses on one page and those for OPT pulses on another for visual simplicity. We start by presenting the results when the RRC pulse is used. By looking at the top 4 figures on the page below, we realize how little or not the system performance changes by using one method or the other. In fact, besides the method where matched filtering is applied in frequency and CD is removed in time which degrades a little the overall system performance, we can observe that all the curves in the ROSNS vs Launch Power plot overlay. Because BER results are equal, it comes very interesting to look at the total computational complexity when each of the 4 techniques is used. This is where we find a real differentiator. The method that has the lowest computational complexity is the one where

Comparison 5 Figures : RRC Pulses Only

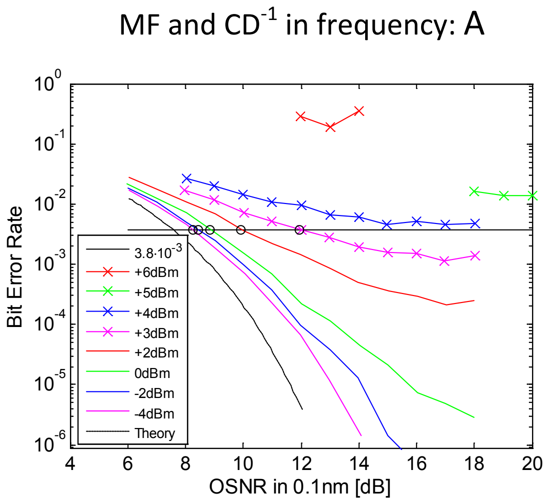

Fig. 40 – 5) RRC) BER vs OSNR: MF + CD^{-1} in f

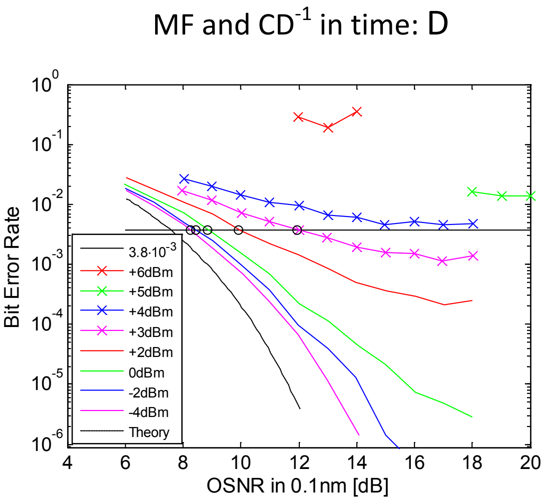

Fig. 41 – 5) RRC) BER vs OSNR: MF + CD^{-1} in t

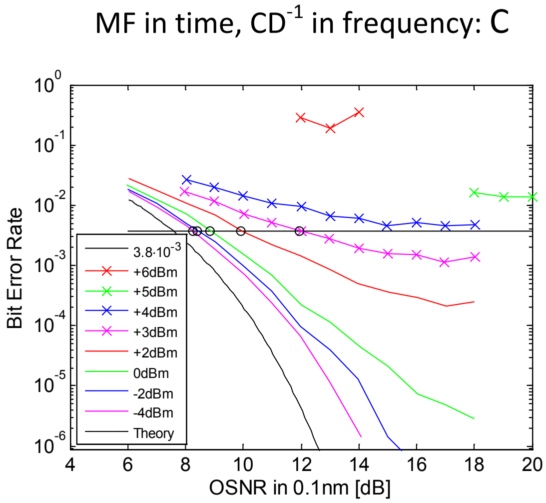

Fig. 42 – 5) RRC) BER vs OSNR: MF t, CD^{-1} f

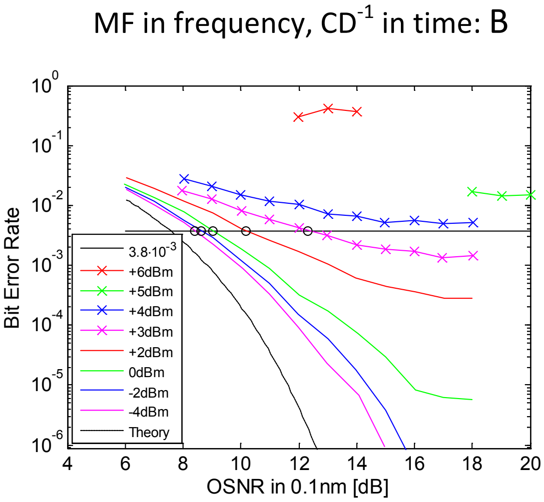

Fig. 43 – 5) RRC) BER vs OSNR: MF f, CD^{-1} t

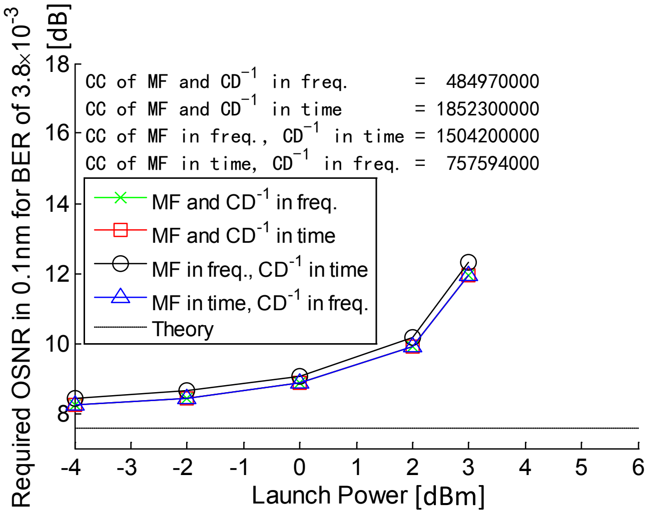

CC of MF and CD^{-1} in freq. = 484970000
CC of MF and CD^{-1} in time = 1852300000
CC of MF in freq., CD^{-1} in time = 1504200000
CC of MF in time, CD^{-1} in freq. = 757594000

Fig. 44 – 5) ROSNR vs Launch Power: RRC only – 4 methods to MF and CD^{-1}

both MF and CD^{-1} are applied in the frequency domain. We will assess the three other methods based on their relative extra complexity with respect to this one by normalizing their CC with that of the “MF and CD^{-1} applied in frequency” method. The second more computationally intense process is the one when matched filtering is applied in time and CD^{-1} in frequency, i.e., process C). This method requires 1.56 times more real multiplications and additions. We can understand why this method requires more computations than the previous one by coarsely studying the required amount of complex multiplication each sample has to receive to apply MF and combat CD. In the first case, when both filters are applied simultaneously, two FFTs are required along with one complex multiplication (CM) for each sample. As studied in the previous sections, an FFT of length N requires in the order of $\log_2(N)$ complex multiplication per sample. Therefore, processing in the frequency domain requires roughly $(2\log_2(N)+1)$ CM per sample. This number doesn’t change because we filter both CD and MF. In fact, if we were to filter only CD, the same complexity would be required. However, when we separate the two filters, one still applied in frequency and the other in time, we inherently increase the CC because we directly add extra multiplication and additions to filter separately in time another linear process. By looking at the length of the time convoluters mentioned above, we can already predict which of the two remaining methods will be in third place for its computer complexity. This second most complex process, C), has a convoluter of length 33. Process B) which keeps the matched filtering in the frequency domain but filters chromatic dispersion in time, uses a convoluter of length 61, and it is indeed the third most complex method with a total CC of 3.1 times that of the all-frequency method and of roughly 2 time that of C). Comparing the total CC of B) and C), we realize that their ratio is really close to the ratio of the length of the convoluter used for the time domain linear filter. This directly tells us that the longer the time domain filter, the more complex the processing will be. Finally, the most computationally complex of all the processes is the one where both MF and CD removal are applied in the time domain. For this case, even if no Fourier transforms are required which could be thought of as a good way to reduce the complexity by not computing two times a FFT, the CC is still really high at 3.8 times that of the all-frequency process. This informs us how linearly filtering in the time domain is cost ineffective.

One could think that dividing the entire signal into shorter blocks and processing each block independently in the frequency domain could increase the computational complexity of the all-frequency case and possibly make case C) more attractive. In fact, computing more FFTs of shorter length requires fewer computations than a single FFT of the entire sequence. This can be proven as follows. Imagine applying a FFT on a vector of length N. The computational complexity of doing so is roughly to the order of $N \cdot \log_2(N)$. Now imagine that we divide the initial vector into 16 smaller vectors, each of length $N/16$ and we process 16 FFTs, each requiring a complexity of $N/16 \cdot \log_2(N/16)$. The total complexity for processing the entire vector is now $N \cdot \log_2(N/16)$, and therefore the complexity per sample is $\log_2(N/16)$ instead of the initial $\log_2(N)$: a reduction by a ratio of $\log_2(16) = 4$ per sample. However, there are two trade-offs for operating in the frequency domain on smaller block sizes, or on shorter temporal acquisitions. The first is that short blocks contain less accurate frequency content than longer ones, simply because the statistics acquired by short temporal acquisitions contain less information on the signal than longer acquisitions. Removing chromatic dispersion on a signal that has biased frequency content can lead to a performance penalty. The second trade-off is the frequency resolution of short FFTs. Indeed, short or long FFTs of signals sampled at the same rate have frequency content that spans in the same range, from $-f_{\max}$ to $f_{\max}$. An FFT of length N will therefore have a frequency resolution of $\Delta f = 2f_{\max}/(N-1)$. One can clearly observe that the resolution will be finer using longer lengths. As chromatic dispersion is an all-pass filter (see Eq. (28)), this filter $H(f_n)$ will only apply inverted dispersion to frequencies $|f_n| = n \cdot \Delta f \leq f_{\max}$. As the real physical process of chromatic dispersion in an optical fibre is applied to all the frequencies continuously, it is better to mimic CD with the finest frequency discretization possible. This greater discretization is

Comparison 5 Figures : OPT Pulses Only

MF and CD^{-1} in frequency: A

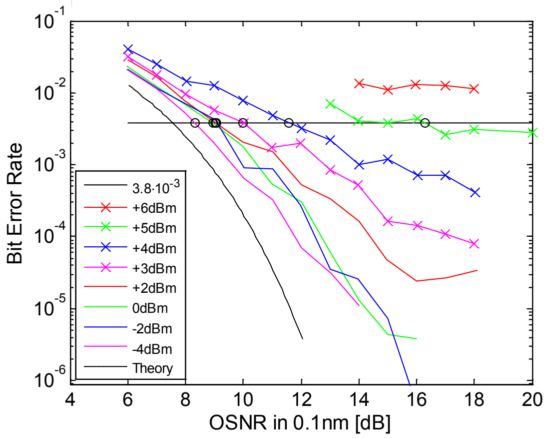

Fig. 45 – 5) OPT) BER vs OSNR: MF & CD^{-1} in f

MF and CD^{-1} in time: D

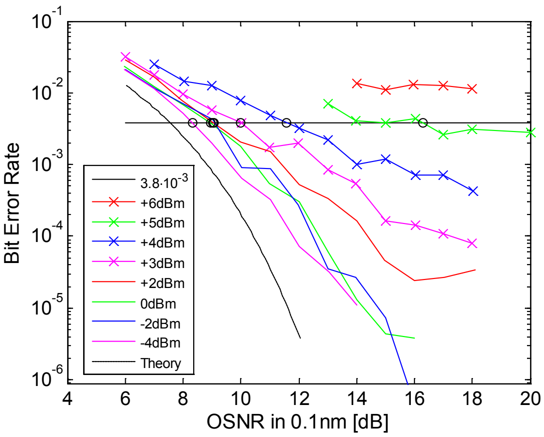

Fig. 46 – 5) OPT) BER vs OSNR: MF & CD^{-1} in t

MF in time, CD^{-1} in frequency: C

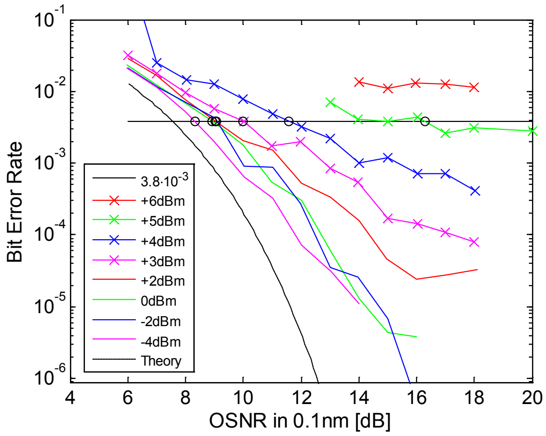

Fig. 47 – 5) OPT) BER vs OSNR: MF in t, CD^{-1} in f

MF in frequency, CD^{-1} in time: B

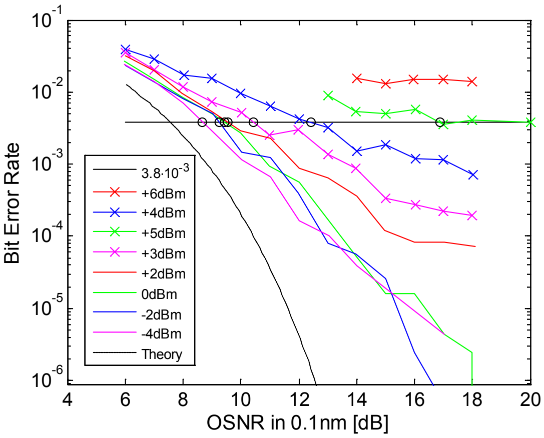

Fig. 48 – 5) OPT) BER vs OSNR: MF in f, CD^{-1} in t

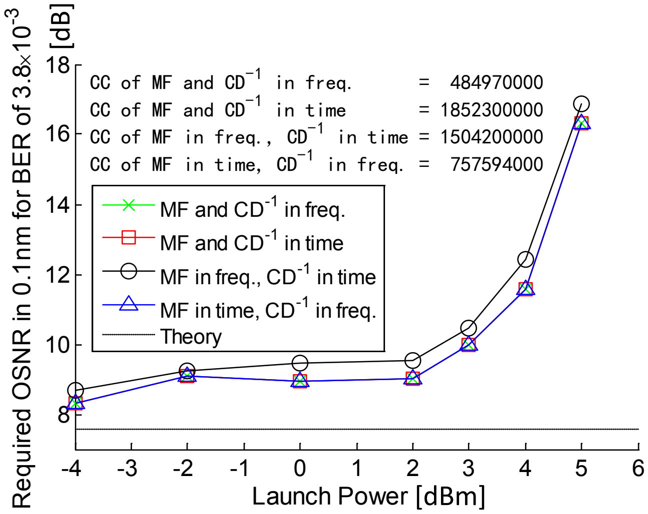

Fig. 49 – 5) ROSNR vs Launch Power: OPT only – 4 methods to MF and CD^{-1}

obtained by taking larger temporal lengths. Our study here is not to assess the impact of processing CD^{-1} using shorter lengths N but only to assess different ways of processing CD and MF in their time and frequency representation. To study the impact of shorter lengths, we could have proceeded by blocks of a fraction of the total length of 2×2^{19}, obtain BER vs OSNR results using the all-frequency method and repeat by increasingly shortening the block size until a system performance degradation is observed and stop at this point. This block size would give the smallest computational complexity for equal system performance.

The results when the OPT pulses were used are presented in the previous page. The observations and conclusion that can be drawn for the OPT pulses are the same as those made for the RRC pulses. One thing to point out is that the ROSNR at +3 dBm of launch power is 1.95 dB less for OPT pulses compared to RRC pulses when using one of the three methods giving the same results, proving again how tolerant to SPM the OPT pulse is. Of course, BERs as low as 3.8×10^{-3} can be reached at high launch powers due to the specific properties of this OPT pulse, allowing curves in the ROSNR for 3.8×10^{-3} BER vs Launch Power plot go to as high as +5 dBm instead of the +3 dBm limit for RRC pulses.

In light of this fifth comparison, we can conclude that it is very beneficial in terms of computational complexity to remove chromatic dispersion and to match filter simultaneously in the frequency domain. Moreover, it makes us tend to think that any bulk linear filter should be applied in the Fourier domain using long lengths.

6.6 – Study of Comparison 6

In this section we will study two different methods to update the coefficients h_{ij} of the polarization demultiplexing subprocess introduced in §3.2.7. We will repeatedly let the coefficients adapt for 2048 symbols using the CMA algorithm followed by a period where the coefficients are fixed and have values given by the last adaptation step. What we will vary is the duration of the period where the

h_{ij}'s are fixed. In the first case, this period lasts 6148 symbols and in the second, this period lasts 18432 symbols. In terms of time duration, coefficients are always adapted for roughly 0.2 μs and are then fixed for either 0.61 μs or 1.84 μs in a repeated fashion. As we process a total of $2^{19} = 524288$ symbols per polarization, the first method is repeated 64 times while the second is repeated 25.6 times. We show the BER vs OSNR curves for both RRC and OPT pulses along with the ROSNR vs Launch Power plot to characterize the methods' performances.

By observing the bottom plot on next page, we realize that keeping the h_{ij} coefficients fixed for a period three times longer doesn't change the final BERs, for any pulse. When we closely look at the two curves in ROSNR vs Launch Power plot for each of the RRC and the OPT pulses, we can clearly appreciate the similarities of the results of the two processes, where the required OSNR for a BER of 3.8×10^{-3} never changes by more than 0.07 dB for the two methods of adaptation. To differentiate the two methods, we can look at the total computational complexity that each method requires. It is obvious that the method where the h_{ij} coefficients stay fixed for a longer period will require less CC, as the adaptations explained in Eq. (31) do not have to occur within this period, saving processing power. This concurs with what we observe above: the complexity for the 2048/18432 adaptive/fix case is less than that of the 2048/6144 case. However, the complexity reduction with respect to the total complexity of the system when h_{ij} are fixed for 18432 symbols is very little: a mere 0.78% of reduction. This tell us how little computationally intense the adaptation of h_{ij}'s in the $\mathbf{H}$ matrix is. With such small variations, in both the ROSNR and the CC, is it harder to find which of the 2048/6144 or 2048/18432 methods is better. To answer this question, we have to look a little deeper at the ROSNR vs Launch Power plot. If we closely look at the curves, we observe that the 2048/6144 case is always slightly better than2048/18432, by a maximal value of 0.07 dB. Knowing that 0.07 dB equals 1.6%, we can answer the previous question by answering the following one: is a reduction in the total complexity of 0.78% worth the increase of ROSNR by 1.6%. Such a small complexity reduction

Comparison 6 Figures

Adaptive for 2048 / Fixed for 6144 symbols:

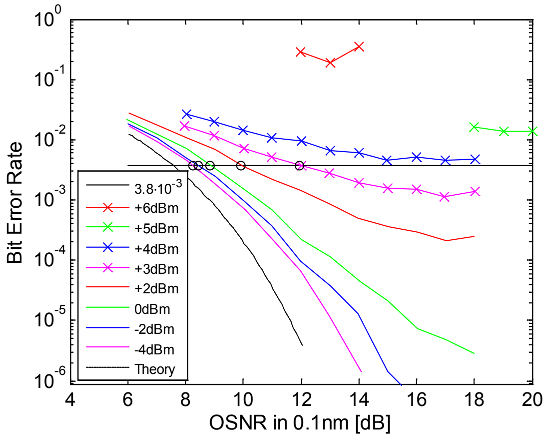

Fig. 50 – 6) BER vs OSNR:RRC - 2048/6144

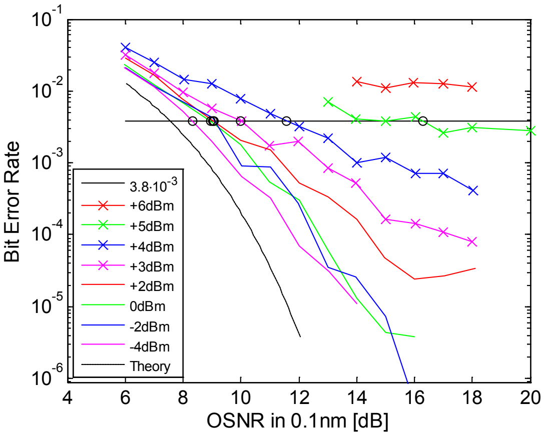

Fig. 51 – 6) BER vs OSNR:OPT - 2048/6144

Adaptive for 2048 / Fixed for 18432 symbols:

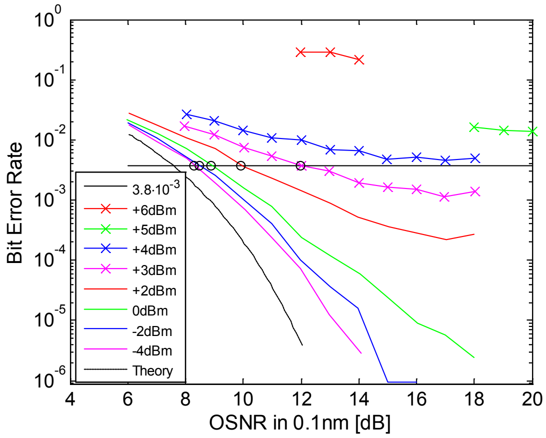

Fig. 52 – 6) BER vs OSNR:RRC - 2048/18432

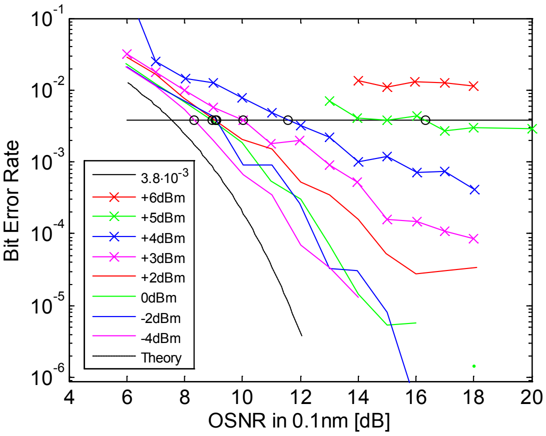

Fig. 53 – 6) BER vs OSNR:RRC - 2048/18432

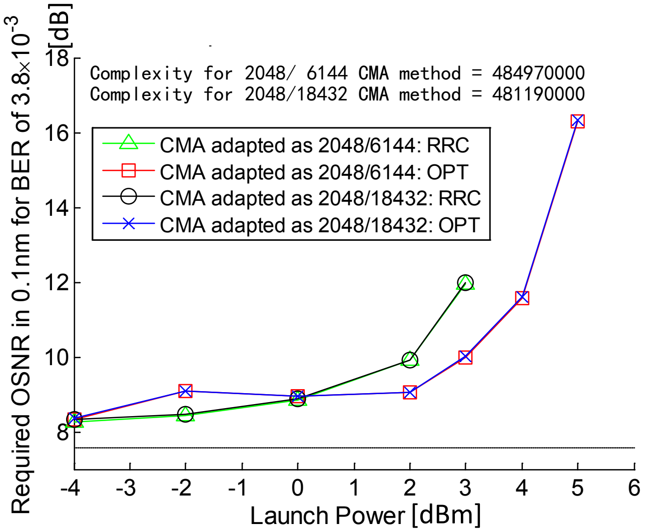

Complexity for 2048/ 6144 CMA method = 484970000
Complexity for 2048/18432 CMA method = 481190000

Fig. 54 – 6) ROSNR vs Launch Power: RRC & OPT - adapt for 2048, fixed for 6144 and 18432

might not worth the increase of the ROSNR, making the 2048/6144 method the preferred one. The final choice would really depend on the system margin itself.

6.7 – Study of Comparison 7

This section of the analysis will look at the impact on the final BER when the step factor μ in the CMA algorithm (see Eq. (31)) is varied from 1×10^{-3} to 5×10^{-3} on 4 different values: $\mu = 0.001$, 0.002, 0.003 and 0.005. For this study we will only show the BER vs OSNR curves for the extreme values of $\mu = 0.001$ and $\mu = 0.005$. We motivate this choice as the BER results for the 4 values of μ only very slightly change. On the ROSNR vs Launch Power plot, we will show the results for all the 4 values of μ. By looking at the two top-left figures, representing the RRC results, and the two top-right figures, representing the OPT results, we observe that the overall BERs between an adaptive coefficient μ of 0.001 or 0.005 don't change much. This means that the μ parameter has a stable value in between these two values. This is straightforwardly proven by looking at the proximity of the curves in the ROSNR vs Launch Power plot. When we closely look at this figure, we observe that the results using 0.005 are always slightly worst. We also observe that, on average, for all the launch powers, the OPT pulse has a ROSNR 0.1 dB lower for $\mu = 0.001$ than for $\mu = 0.005$ and the RRC pulse performs better on average for $\mu = 0.002$ compared to $\mu = 0.005$ by 0.057 dB. To differentiate $\mu = 0.001$ from 0.002 and find the best value, we find which of the 2 coefficients maximize the deviation from the results using $\mu = 0.005$. For the OPT pulse, 0.001 has a ROSNR lowered by 0.184 dB at launch power of +3 dBm and for the RRC pulse, it is also 0.001 that lowers the most the ROSNR from the 0.005 results, this time by 0.06 dB at launch power of 0 dBm. Therefore, we conclude that $\mu = 0.001$ is a better choice.

Even if results are similar between 0.001 and 0.005, one cannot say that μ can be increased by factors of 5 indefinitely without affecting the results. By doing so we would rapidly fall out of the stable zone. We can have a better understanding of

Comparison 7 Figures

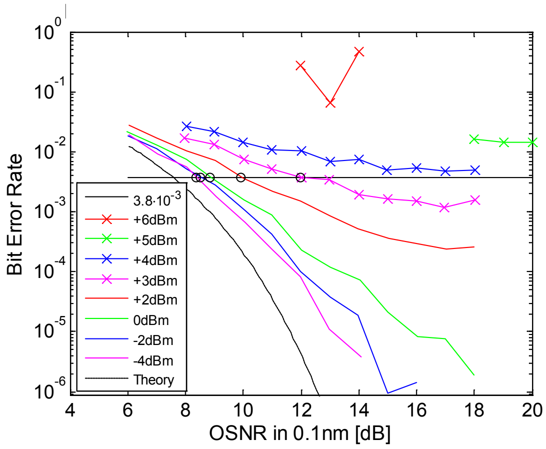

Fig. 55 – 7) BER vs OSNR: RRC : μ=0.001

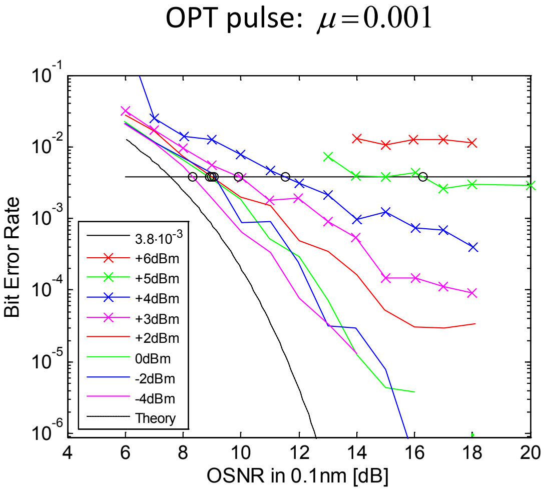

Fig. 56 – 7) BER vs OSNR: OPT : μ=0.001

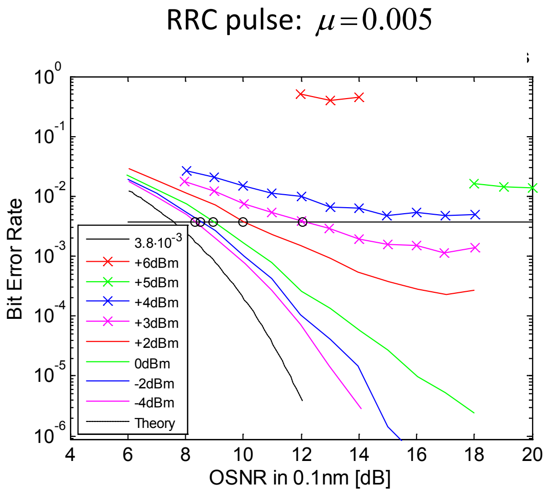

Fig. 57 – 7) BER vs OSNR: RRC : μ=0.005

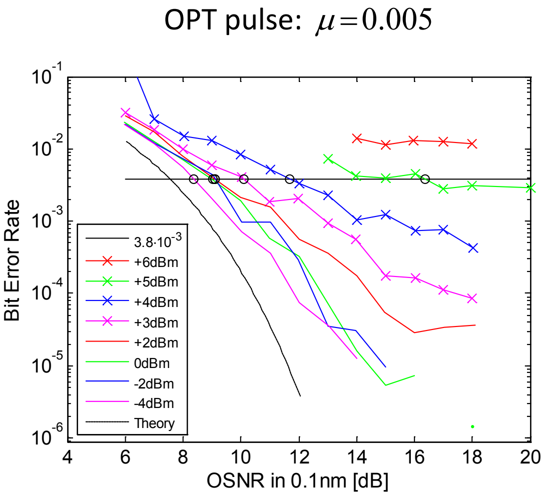

Fig. 58 – 7) BER vs OSNR: OPT : μ=0.005

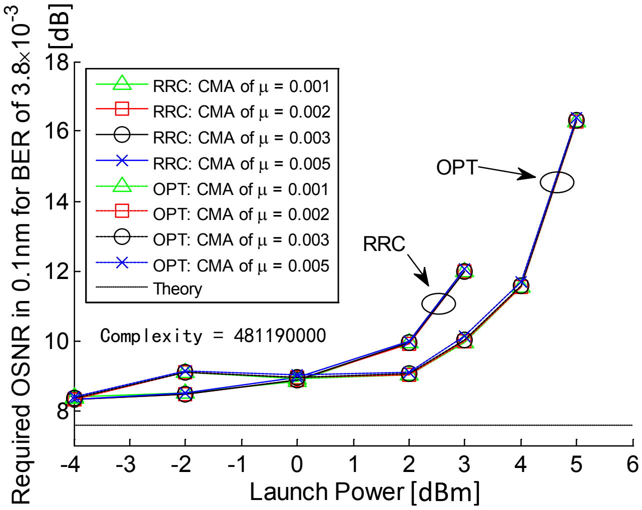

Fig. 59 – 7) ROSNR vs Launch Power: RRC & OPT : μ=1, 2, 3 or 5 x 10^{-3}

the impact of μ on final errors by looking at the equation that drives the updating method of $\vec{h}_{\mathrm{xx}}$: $\vec{h}_{\mathrm{xx}}^{i+1}-\vec{h}_{\mathrm{xx}}^{i} = -\mu\,\overbrace{(|\mathrm{x}_{\mathrm{out}}|^{2}-1)\,\mathrm{x}_{\mathrm{out}}\cdot\vec{\mathrm{x}}_{\mathrm{in}}^{*}} = -\mu\,\varepsilon\,\vec{\mathrm{x}}_{\mathrm{in}}^{*}$. The term under the curly bracket is $\nabla_{h}J(h)$, the vector gradient of the CMA cost function $J=E\left[(|\mathrm{x}_{\mathrm{out}}|^{2}-1)^{2}\right]$ where $\mathrm{x}_{\mathrm{out}}=(\vec{h}_{\mathrm{xx}}^{i})^{\dagger}\cdot\vec{\mathrm{x}}_{\mathrm{in}}$. We clearly see the impact of μ on the following $\vec{h}_{\mathrm{xx}}^{i+1}$ coefficients, and consequently on the output $\mathrm{x}_{\mathrm{out}}$, when updating from i to $i+1$. The more $\mu\rightarrow 0$, the less $\vec{h}_{\mathrm{xx}}$ is changed for each adaptation, to the limit where $\vec{h}_{\mathrm{xx}}$ stays fixed for $\mu=0$. The other limit, when $\mu\rightarrow 1$, means that $\vec{h}_{\mathrm{xx}}$ is always increased by full value of the update error $\varepsilon=(|\mathrm{x}_{\mathrm{out}}|^{2}-1)\,\mathrm{x}_{\mathrm{out}}$ and will make $\vec{h}_{\mathrm{xx}}^{i}$ wobble and diverge with increasing indices i as soon as $|\mathrm{x}_{\mathrm{out}}|\neq 1$. It is easier to see for real $\mathrm{x}_{\mathrm{out}}$, where the slope of the error ε equals 2 at $\mathrm{x}_{\mathrm{out}}=1$ while the error itself is 0, giving a bigger error ε than the deviation itself of $|\mathrm{x}_{\mathrm{out}}|$ from its desired value of 1. We could have studied a wider range of μ parameters, from values much closer to 0 to values much closer to 1, but the bulk of the results would not lead to a stable converged $\mathbf{H}$ matrix either because the adaptation is not sensitive enough (too small μ) or too sensitive (too high μ) to the inputs and we would simply have a symbol error rate of 3/4. By this study, we wanted to prove that the CMA algorithm has a stable output for step parameters in the relatively wide range 1×10^{-3} to 5×10^{-3}. Of course, changing μ does not impact the computational complexity.

6.8 – Study of Comparison 8

In this comparison, we will study the Carrier Phase Estimation process. More precisely, we will analyse the impact that the number of taps used in the CPE can have on the final BER and we will show the results for two different numbers of taps. The figures will show the BER vs OSNR plot for both types of pulses, each processed using 71 or 101 taps. The bottom figure shows the ROSNR vs Launch Power plot along with the total computational complexity. As we know, changing the number of taps doesn't change the CC, because of our efficient implementation of the moving average windows (see §4.2). As explained earlier, the goal of the CPE process is to remove the phase noise due to the LO and the transmit laser as well the any remaining frequency offset that the bulk removal done is the previous Carrier Frequency Offset (CFO) process did not remove.

We observe in the figures that the use of a number of taps as high as 101 removes without any problem the phase noise and remaining frequency. This means that the remaining frequency offset between the LO and the signal lasers after the CFO process is smaller than $50/4 = 12.5$ MHz (see § 3.2.9). We knew from previous study in § 3.2.8 that the maximal CFO for a QPSK signal at 10 Gbaud/sec is 1250 MHz. This means that our CFO removal algorithm suppress any frequency offset up to $\pm 1250\,\text{MHz}$ to $0 \pm 12.5\,\text{MHz}$, assuring us that our CFO removal process operates adequately. Moreover, we know that for a CFO removal process operating in the frequency domain using an FFT, the frequency discretization is roughly 40 KHz, obtained from $2\times 10\,\text{GHz}/2^{19} \approx 40\,\text{KHz}$ where the total bandwidth of the signal is 20 GHz and the FFT accounts 2^{19} points. If we allow a ± 4 points deviation of the frequency selected from the real mean intermediate frequency, this means that the CFO process removes frequency deviation to a precision of roughly $\pm 160\,\text{kHz}$, a value far from 12.5 MHz. Therefore, this working phase removal process using 101 taps attests that during the 2^{19}'s symbols duration of $\approx 52\,\mu\text{s}$, the LO's instantaneous phase derivative does not deviate by more than 12.5 MHz.

Consequently, one could think that as the CPE works for 101 taps, meaning that there's a maximum remaining frequency offset of 12.5 MHZ, it would give the same results for any other number of taps as long as it is below 101. Such a smaller number would then wrap the phase noise on the same circle of radius $R = 1/(2\tan(4\psi/2))$, with $\psi = 2\pi f_{\text{IF rem.}} T$, but covering a circle portion smaller than half the circumference. In fact, this for true up to a lower bound at which the results start to be biased. For too small tap lengths, the normally round 4 blobs of points that consists the constellation become squeezed in the angular direction. This phenomenon can be understood by observing the limit behaviour when the tap length is 1where all angular deviation from $(2k+1)\pi/4$, $k = \{0,1,2,3\}$, is removed, inherently biasing the naturally complex nature of additive white Gaussian noise of amplified spontaneous emission in optical amplifiers.

On the other hand, we found in § 3.2.9 that a maximal number of taps of 151 would still converge with a remaining intermediate frequency offset of 8 MHz. To explicitly demonstrate this with experimental results, we show below a figure of the corrected phase noise out of the CPE process for 6 different tap lengths For tap lengths greater then 391, we observe phase slips [60, 61]. Phase slips can occur when the outputs of the mean phase detector lie in the vicinity of the extremes of the $[-\pi, \pi]$ range. When the output of the mean phase is close to $+\pi$ or $-\pi$, $\pm 2\pi$ phase jump have to be applied to the output for proper phase tracking. This phase jump correction is called Phase Ambiguity Resolver (PAR), is part of the CPE algorithm and is needed as phasors pointing at $\pi - \delta$ and at $-\pi - \delta$ have numerically the same real and imaginary values.

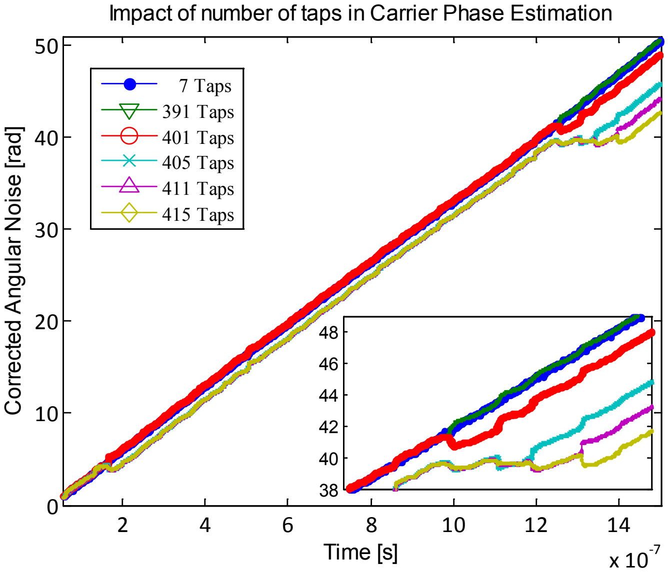

Fig. 60 –Phase Output of the CPE algorithm for 7, 391, 401, 405, 411 and 415 taps

From tap lengths 7 to 390, the BER does slightly vary but the CPE keeps track of the phase noise and the proper constellation is recovered. Starting at 401 taps and above, we observe several 2π phase slips, where their number increase with number of taps. It is worth noting that for QPSK signals and due to the fourth power operation, the 2π phase jump will turn into a $2\pi/4$ jump, rendering each decided symbols erroneous.

On the previous figure it is interesting to notice that all corrected phase initially start operating similarly and suddenly loose track and begin differing with higher tap lengths. This specific experimental result shows a phase noise that is almost constantly drifting during this time duration at a rate of roughly 5.3 MHz. Using the equation $4f_{\mathrm{IF}}T(M-1) \le 1/2$, with $M = 391$ and remembering that the $1/2$ factor comes from the half circumference allowance for phase wrapping, we prove here that our study works experimentally: by allowing a wrapping around $5/6$ th of the circumference instead of $1/2$, we fall back on the allowed remaining f_{IF} of 5.3 MHz. Said differently, for a f_{IF} of 5.3 MHz, the theoretical maximal number of taps is 391, which is what we observe experimentally.

The PAR works in conjunction with the moving average window of length M introduced earlier: its input is the angle out of the average of the elements in the window and its output is either the same as the input when no phase jumps are detected or a $\pm 2\pi$ rectified version of it in the contrary [48]. The length of this average window obviously changes its output as more or less terms are summed. This consequently changes the input to the PAR and possibly its output and the phase decided. This moving average window acts as low pass filter, and such filter could, for very noisy signals, not be able to properly track the drifting phase.

To prove similarity of results between 7 and 391 taps, we processed all our acquisitions using another number of steps: 71. By looking at the ROSNR vs Launch Power curves, we can say that the results for both types of pulse are the same. We show that any number of taps between 7 and 391 will properly remove the remaining frequency offset (for a maximum of $f_{\mathrm{IF}} = 5.3$ MHz) and the phase noise. The goal of our analysis here was not to find the lowest or the highest bound for each launch power and pulse type but to explain in detail the consequences of taking too long of too short window lengths.

Comparison 8 Figures

Carrier Phase Estimate using 101 Taps:

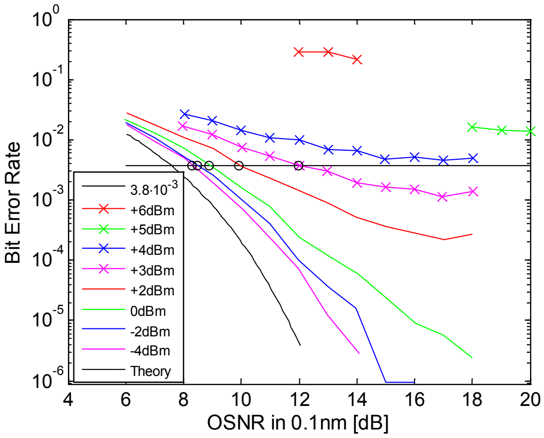

Fig. 61 – 8) BER vs OSNR: RRC – 101-tap CPE

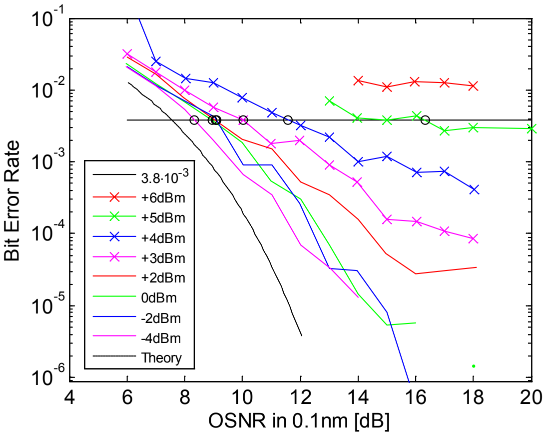

Fig. 62 – 8) BER vs OSNR: OPT – 101-tap CPE

Carrier Phase Estimate using 71 Taps:

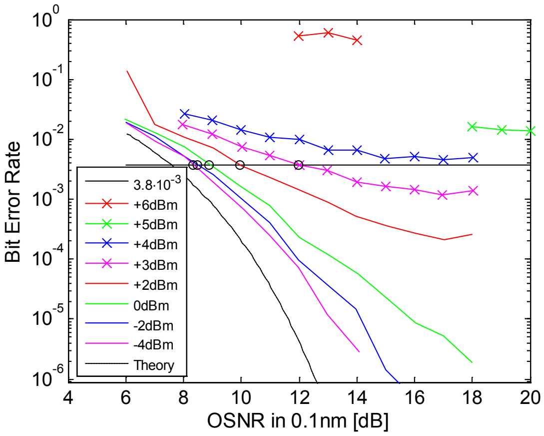

Fig. 63 – 8) BER vs OSNR: RRC – 71-tap CPE

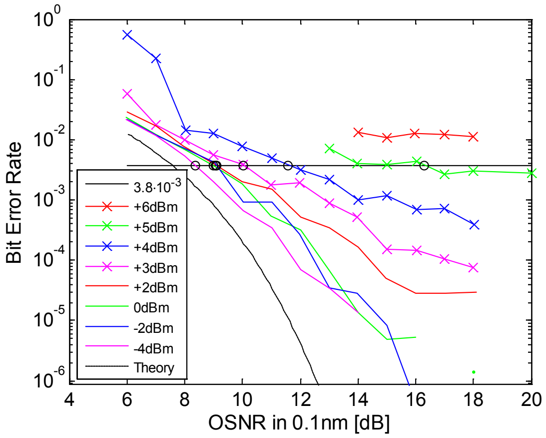

Fig. 64 – 8) BER vs OSNR: OPT – 71-tap CPE

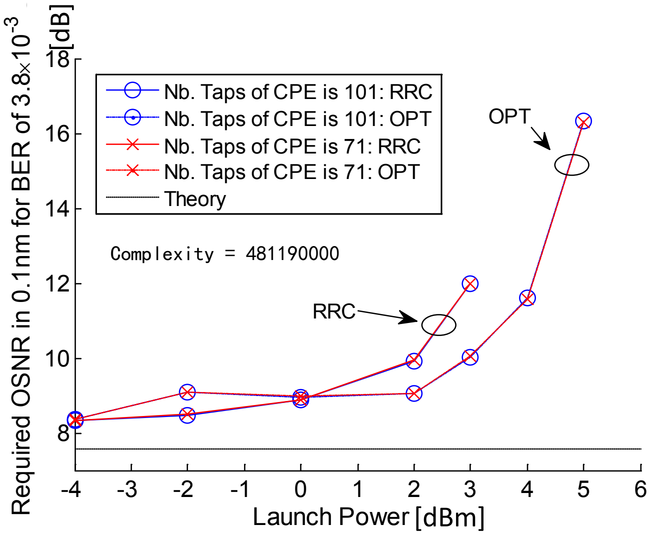

Fig. 65 – 8) ROSNR vs Launch Power: RRC & OPT: 101- and 71-tap CPE

6.9 – Study of Comparison 9

In this study, we compare the differences of two methods for removing the bulk frequency offset between the transmit and the LO lasers. The first method uses a frequency domain approach whereas the second method uses a time domain approach. For the first method, we use the Power Spectral Density (PSD) of the fourth power of the input signal to find a tone to which we assign the value of the frequency offset. As explained in earlier chapters, putting a QPSK signal to the fourth power completely removes the modulation. Both the time and the frequency domain approaches use this unmodulated data to find the frequency offset. The frequency approach computes the FFT of this unmodulated signal and finds the frequency at which the magnitude of the FFT has a maximal value. This frequency is labelled $4f_{\mathrm{IF}}$ and the phase $2\pi f_{\mathrm{IF}} nT$, $n = 0, 1, 2, \ldots$ is removed from symbols $\hat{a}_n$. For the time domain approach we use the method of A. Leven [47] and explained in §3.2.8 where each fourth power symbol is multiplied by the fourth power of the complex conjugate of the proceeding symbol. The resulting phasors are summed. The angle of the sum represents $4f_{\mathrm{IF}}$ and the intermediate frequency is removed using the same technique as for the PSD approach. For both approaches, the entire length of 2^{19} symbols is used to compute the FFT or in the sum. The computational complexity of the methods is calculated and displayed in the ROSNR vs Launch Power figure at the bottom of the previous page.

We observe that for very noisy signals, due to low OSNR and high nonlinear phase noise, the time domain approach doesn't work and the CFO doesn't capture the bulk frequency offset between the LO and Signal lasers. As a consequence, the remaining frequency offset is too large for the subsequent CPE algorithm to track and we observe a very high BER due to multiple phase slips. These points of non-convergence are seen in the top-right figure for the OPT pulses at +3 and +4 dBm for very low OSNR and even at high OSNRs when a lot a NL phase noise occur, at +6 dBm. On the other hand, the PSD method applied to the same very

Comparison 9 Figures

Time Domain Approach Using $\angle\left(\sum x_n^4 \bar{x}_{n-1}^4\right)$:

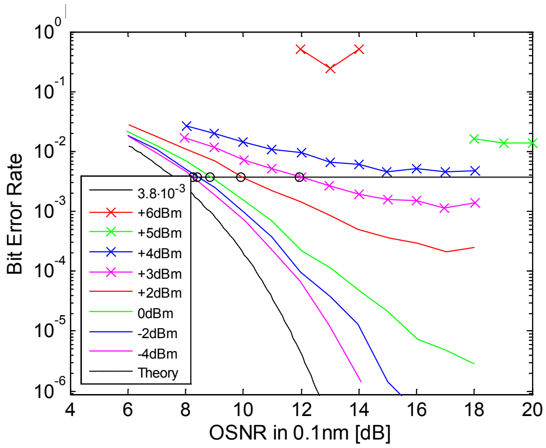

Fig. 66 – 9) BER vs OSNR: RRC –CFO in t

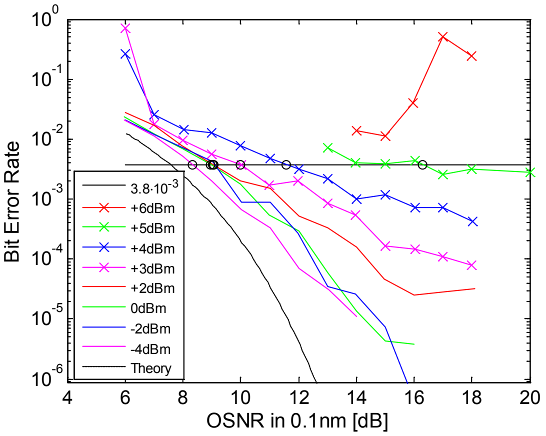

Fig. 67 – 9) BER vs OSNR: OPT –CFO in t

Frequency Domain Approach Using the PSD of x^4:

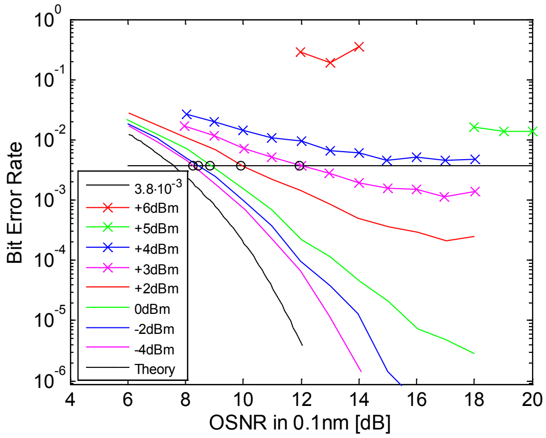

Fig. 68 – 9) BER vs OSNR: RRC –CFO in f

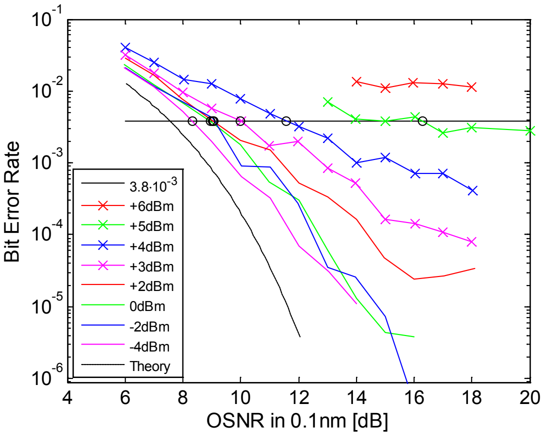

Fig. 69 – 9) BER vs OSNR: OPT –CFO in f

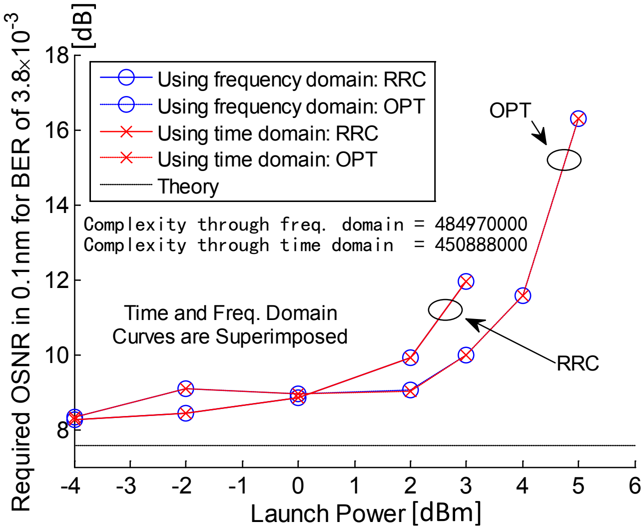

Fig. 70 – 9) ROSNR vs Launch Power: RRC & OPT: time and frequency domain removal of CFO

noisy sequences have no problem to deliver a tone that truly represents f_{IF}. Besides these extreme cases, we can observe that the two methods give coincident BERs. This observation is easier to make when looking at the ROSNR vs Launch Power figure. We see that the curves for the time approach and the frequency approach overlay, respectively for the RRC pulse and the OPT pulse. It then becomes very interesting to look at the computational complexity. We then realize that the time domain approach requires 7% less computations then its frequency counterpart. As a 7% reduction of the total required computations is significant, we conclude that the time domain approach is the better choice as it gives equal results to the frequency approach, at a computational cost reduction of 7%.

6.10 – Study of Comparison 10

In this last analytical section, we will study and compare the impact on the BER for three different nonlinear propagation steps. By nonlinear propagation step, we mean the distance increment for each nonlinear compensation application, named Δz in section §3.2.6. The steps we use and study are of 20 km, 10 km and 5 km. As a way to better assess the impact, we not only compare the results for these three steps values together but also with the case where no nonlinear mitigation is done at the receiver. For this case, the chromatic dispersion is removed all at once in the frequency domain, for the entire distance of 1200 km, instead of by chunks of 5, 10 or 20 km like is done when nonlinearity compensation is applied. Of course, one would expect that the smaller step would give the best results as it mimics more appropriately the beam as it propagates down the fibre.

The first set of figures presents the results only for the RRC pulse. We decided to separate presentation of the results for the RRC and the OPT simply because the OPT pulse was itself designed to mitigate nonlinearities without the need to apply nonlinear DSP at the receiver. Our goal here is more to compare the impact of the choice of NL step size than to compare the results of NL mitigation for RRC and OPT pulses. Although, as all the figures are presented, the reader can without any problem compare the results of the two pulses for a same step size. By looking at the figures for the 5, 10 and 20 km steps using the RRC pulse, we realize that, indeed, the BER is lower for smaller values of NL propagation distance. If we observe only one acquisition result, say at a launch power of +4 dBm with an OSNR of 18 dB, we realize that as the propagation distance Δz decreases, the resulting BER decreases as well: for $\Delta z = 20$ km, the BER equals 20.2×10^{-5}, for $\Delta z = 10$ km, the BER equals 7.0×10^{-5} and for $\Delta z = 5$ km, the BER equals 4.9×10^{-5}. This proves the effectiveness of our NL mitigation method and the accuracy of the parameters it uses, especially the nonlinear parameter γ.

For the $\Delta z = 5$ km case, it is very interesting to see how close the -4 dBm curve behaves with respect to the theoretical curve representing the BER in the purely linear case where only white Gaussian noise is assumed. This curve, representing a launch power that is known not to suffer a lot from nonlinearities, obeys very similarly to the linear theory. The curve doesn't go pass an OSNR of 13 dB because higher OSNRs showed no errors in $4\text{x}2^{19}$ bits received. Compared to the "No NL mitigation" case, this means that even at such low powers the benefit of NL compensation is perceptible. As a numerical comparison, the BER at a launch power of -4dBm with OSNR of 13 dB is at 11.05×10^{-5} without NL mitigation, at 7.69×10^{-5} for the $\Delta z = 20$ km case and at 6.73×10^{-5} for the $\Delta z = 5$ and 10 km cases. A BER reduction of 39 % by switching on the NL compensation even at such low power is very considerable.

When we look at the two figures representing BER results for the $\Delta z = 5$ and 10 km cases, we realize however how little the results change by doubling the nonlinear propagation distance. In fact, the ROSNR vs Launch Power figure at the bottom of the next page shows how close to a perfect superimposition the "5 km" and the "10 km" curves are. They differ by roughly 0.002 dB when we closely zoom in: an insubstantial difference. On the other hand, the "20 km" curve effectively shows a small penalty compared to the more precise NL mitigation approach of "10 km". The presence of the nonlinear uncompensated curve in this

Comparison 10 Figures: RRC Pulses Only

Steps of 5 km:

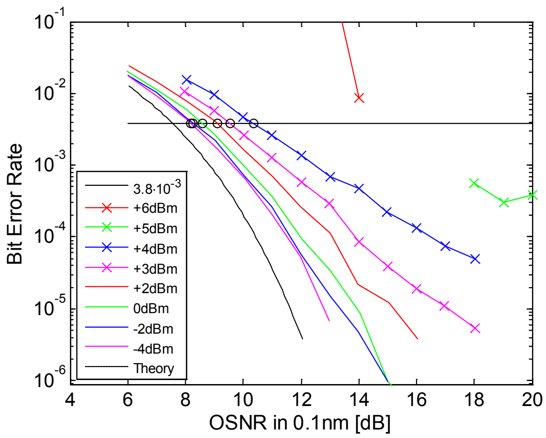

Fig. 71 – 10) BER vs OSNR: 16 steps per span

Steps of 10 km:

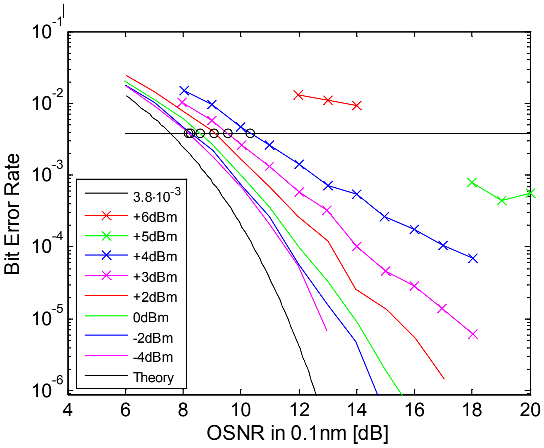

Fig. 72 – 10) BER vs OSNR: 8 steps per span

Steps of 20 km :

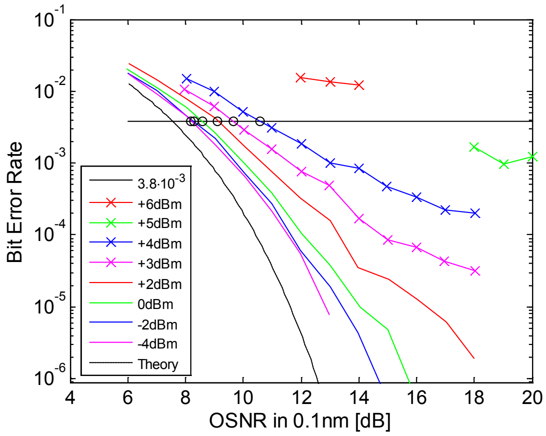

Fig. 73 – 10) BER vs OSNR: 4 steps per span

No NL Mitigation:

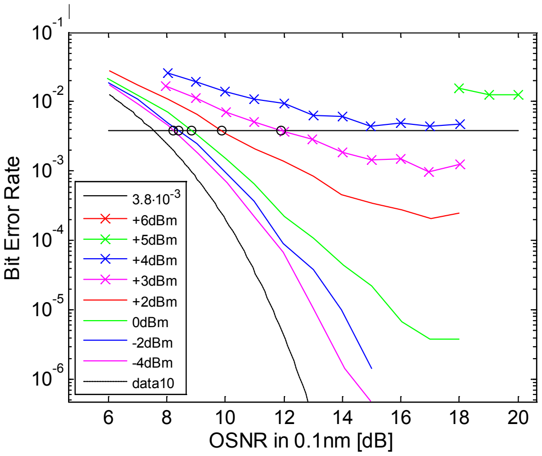

Fig. 74 – 10) BER vs OSNR: 0 steps per span

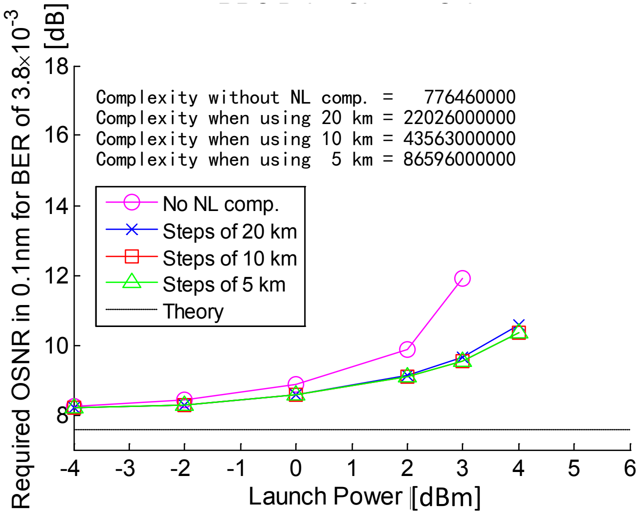

Fig. 75 – 10) ROSNR vs Launch Power: RRC only: 16, 8, 4 and 0 NL steps/span

figure gives us a better sense on the BER improvement increasing with launch power by applying NL compensation. We can appreciate how this curve is pushed down, allowing smaller signal power to noise ratio requirements by compensating NL even with relatively large steps of 20 km.

Finally, we want to compare the change in the computational complexity when we change the size of the nonlinear propagation distance. As expected, the total required amount of real multiplications and additions is decreased by increasing the NL propagation step size. We observe the nearly linear decrease of total CC with increasing step size. For instance, decreasing by a factor of 2 the number of NL steps per span of 80 km from 16 (5 km case) to 8 (10 km case) diminishes by a factor of 1.99 the total complexity. A reduction factor of 4, decreasing to 4 NL compensations per span (20 km case), diminishes by a factor of 3.93 the CC. This reminds us how computationally intense NL mitigation is, accounting for almost all the computations at the receiver, and shows an almost direct relation between the number of NL compensation steps applied per span with the total CC required. For the case when 4 NL compensations is applied per span, 2.2×10^{10} operations are required to process 2^{19} symbols' worth of time at 100 ps per symbol. This means that 420 Teraoperations/sec would be required in a real-time system, which is totally unrealistic as 2009 commercially available coherent receivers offer 12 Teraoperations/sec [62]. Our case without NL compensation requires 7.8×10^{8} operation, giving a real time implementation at 14.8 Teraoperations/sec, which is much closer to the available speed of commercial products.

The next page displays the results for the OPT pulse alone. As the BER vs OSNR curves look very similar for the three NL step sizes, we will focus our comparison on the ROSNR vs Launch Power figure. First of all, by comparing the three curves where NL is mitigated with the one where is it not, the realize that activating NL compensation is of course beneficial in terms of system performance, but the improvement is not as substantial as for the RRC pulses. The OPT pulse naturally behaves better at high powers when no NL mitigation is

Comparison 10 Figures: OPT Pulses Only

Steps of 5 km:

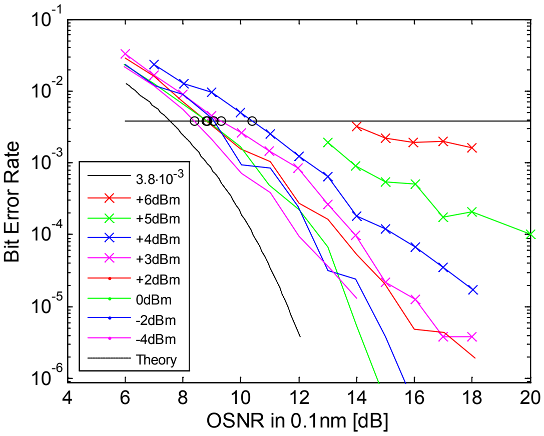

Fig. 76 – 10) BER vs OSNR:OPT 16 steps per span

Steps of 10 km:

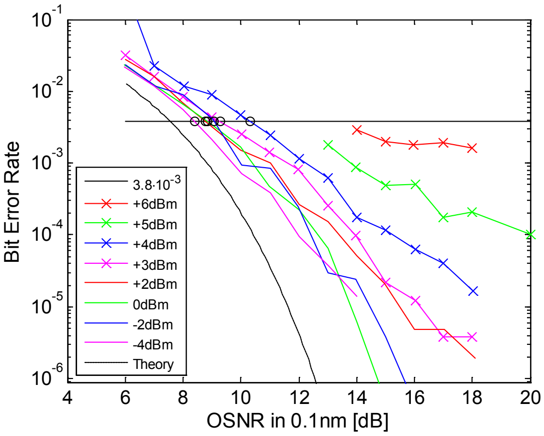

Fig. 77 – 10) BER vs OSNR: 8 steps per span

Steps of 20 km :

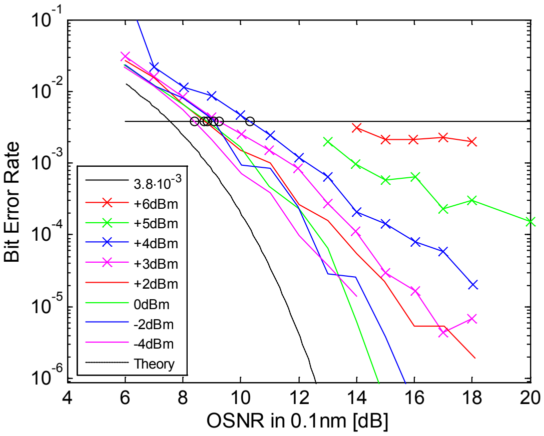

Fig. 78 – 10) BER vs OSNR: 4 steps per span

No NL Mitigation:

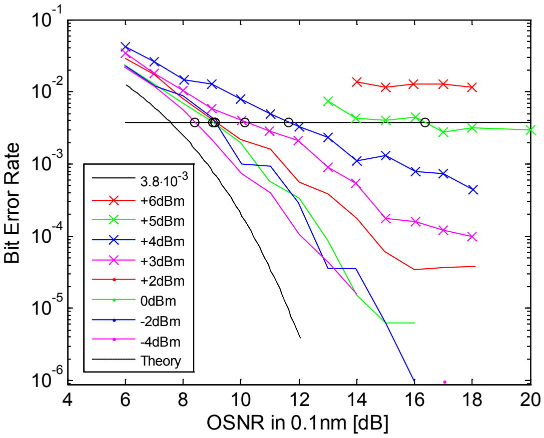

Fig. 79 – 10) BER vs OSNR: 0 steps per span

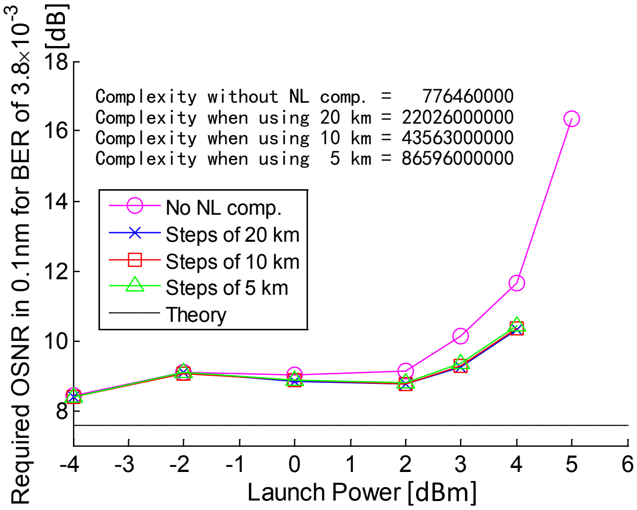

Fig. 80 – 10) ROSNR vs Launch Power: OPT only: 16, 8, 4 and 0 NL steps/span

applied at the receiver through DSP because they were conceived intentionally. Hence, the improvement when NL mitigation is activated is not as substantial and it shows in the bottom plot where the push downwards is not as strong.

Just like the results for the RRC case, the three curves almost overlay. However, when we closely look, the OSNR requirements are always a little bit lower when steps of 20 km are used compared to 5 or 10 km. This observation is surprising and unexpected. We believe that this behaviour could be explained through the OPT pulse as it was created in the sole purpose of diminishing the effect of Self-Phase Modulation. As our NL compensation technique mitigates at the same time SPM and Pol.-XPM, it could explain why compensating for both nonlinearities more frequently per span gives poorer results. With our NL mitigation methods, these two effects are fully compensated 16, 8 or 4 times per span. However, NL compensation every 20 km is much less accurate than every 5 km and represents less precisely the real NL impairments that happened in the fibre. As the OPT pulse received less SPM, fully compensating it 16 times per span, as much as Pol.-XPM, can lead to excessive SPM compensation and worsen results. We can confront this observation with the results obtained in [50], where the authors use NL pre-compensation instead of post-compensation as we do. They obtain at the receiver a clean eye diagram, showing that the nonlinear phase noise is removed. If they were to back propagate again the received signal though post DSP, results would be worsened because extra NL phase noise would be added. Analogously, this is what happens by fully compensating the SPM for the OPT pulse.

We can equally assess the simultaneous use of OPT pulse with NL compensation and find that both usage improves the OSNR requirements compared to an equal processing method applied on RRC pulses. For instance, as a numerical evaluation, the OSNR requirement for a BER of 3.8×10^{-3} improves by 0.27 dB at a launch power of +3 dBm using NL propagation steps of 10 km. Finally, the computational complexity obviously doesn’t change with the type of pulse used and our analysis on CC for RRC pulse directly applies to OPT pulse

6.11 – Summary of Analysis

We will summarize the conclusions drawn from each of the 10 analysis realized in this chapter, in order to point out the best way to post-process a DP-QPSK signal after an optical coherent receiver. By best way, we mean the choice of parameter values and methods that give the lowest bit error rate at the receiver. In the case where the method engenders a strong compromise on the computational requirements, we opt for the approach demanding the least computations.

In our first comparison, we studied the impact of the length of the depolarization process $\mathbf{H}$, for 9 taps and 5 taps. We obtained different results for RRC and OPT pulses. We conclude that, for RRC pulses, 5 taps gave better system performance and required less computation. For OPT pulses we conclude that 9 taps is a better choice with a trade-off of 10% increase of CC, increasingly improving the system performance with launch power, of 0.175 dB on average.

In our second study, we compared two methods to adapt $\mathbf{H}$: always adapted at every symbol or adaptive for 2048 symbols and constant for 6144 symbols. Both methods gave the same system performance, but as the non-always adaptive approach reduces the CC by 2.5%, we conclude that the 2048/6144 adapt/fix method is better.

In the third comparison, we compared the impact on the performance and on CC when nonlinear impairment mitigation is activated and when it is not. We observed an increase of the CC by 110 times when NL is compensated by chunks of $\Delta z = 5$ km. We conclude that for RRC pulses at high launch powers, the benefit on the final BER is enormous, e.g. 2.3 dB of ROSNR reduction at +3 dBm, but not as much for OPT pulses, lowering by less than 0.8 dBm the ROSNR. We conclude that NL mitigation does improve a lot the final BER, but with a significant drawback when using standard SSFM at $\Delta z = 5$ km. Therefore, NL compensation should be applied, but through a method requiring much less computations than the several-step-per-span SSFM method used.

The fourth analysis was studying the same parameter as the first analysis under the same conditions, except with nonlinearities mitigated. Similarly to what was observed in *Study 1*, it is also better to use 5 taps for RRC pulses when NL is compensated, only because it requires 0.1% less computations. For OPT pulses, 9 taps give a better ROSNR of 0.16 dB on average. We therefore conclude that, with or without NL mitigation, it is better to use 5 taps of RRC and 9 taps for OPT.

In the fifth comparison, we compared all the possible methods to match filter and apply the inverse chromatic dispersion, both either in the time or in the frequency domain. We conclude that, simply because of its smaller CC, it is better to remove chromatic dispersion and to match filter simultaneously in the frequency domain, for both type of pulses.

In our sixth comparison, we studied two non-continuously adaptive ways to update the coefficients of the depolarization **H** matrix. The first way kept **H** fixed for 6144 symbols and the second, for 18432. Both methods were adapting the coefficients for 2048 symbols and the process was repeated. The 6144 method had ROSNR results never better than 0.07 dB compared to the 18432 method, at a CC cost of 0.78%. We conclude that system margin would differentiate the best choice, but tend to prefer the 2048/6144 approach simply for its small overall ROSNR reduction.

In *Study of Comparison 7*, we varied the strength of the step size parameter μ to four different values, namely 0.001, 0.002, 0.003 and 0.005, to observe the impact on the tracking of the **H** matrix and consequently on the resulting BER. We conclude that $\mu = 0.001$ gives a lower BER, sometimes giving a ROSNR lowered as much as 0.18 dB compared to using $\mu = 0.005$.

The eighth comparison was intended to study the impact of varying the amount of elements in the carrier phase estimation process. The two number of taps used were 71 and 101, and both gave similar results, where the ROSNR didn't diverge by more than 0.018 dB, with equal computational complexity. As using 71 taps acts as a less stringent low pass filter and can recover higher remaining frequency offset, we conclude that the smaller window length of 71 is better than 101.

For the ninth comparison, we examined two methods to remove the bulk of the carrier frequency offset. The first method employs the power spectral density using the FFT of the signal and the other multiplies each element by the complex conjugate of the preceding element, and sums the results. We conclude that the time domain approach is a better choice as it gives the same results for a computational complexity reduction of 7%.

In the last comparison, *Study of Comparison 10*, we varied the number of steps per span of 80 km at which the nonlinear coefficients of the SSFM method are calculated. We varied between 16, 8 and 4 times per 80 km. For both type of pulses, all of these 3 step sizes require a gigantic amount of computations that is unrealistic with today's available processing speeds, even if a diminution by a factor of n of the number of steps almost proportionally decreases the total complexity. As the ROSNR results are no more than 0.3 dB apart from -4 dBm to +2 dBm for OPT pulse when comparing with and without NL compensation, we conclude not to compensate NL for OPT pulse if the launch power is lower or equal to +2 dBm. For the RRC pulse, the system performance increase, even using $\Delta z = 20$ km, is too strong not to recommend compensating NL, although the required computation increase stays out of reach of today's capabilities.

Chapter 7 : Conclusion and Future Work

Optical coherent receivers offer the advantage to access the amplitude and phase of the optical field. On the other hand, direct detection squares the complex optical electric field and looses track of any phase variation, making linear impairments happening in the optical fibre becoming nonlinear due to signal squaring. The advantage of coherent receivers is to allow post compensation in the electric domain of linear and nonlinear impairments through Digital Signal Processing applied at the receiver side. This new approach makes the use of optical compensators obsolete, and alleviates the optical link from expensive and bulky dispersion compensation modules that increase significantly the loss per span, traditionally compensated with additional amplification. Moreover, coherent receivers with DSP allow the use of advanced modulation formats which can increase manifold the spectral efficiency and also enable the recovery of polarization multiplexed signals, further doubling the transmission bit rate.

7.1 – Summary

In this thesis we presented the fundamental digital signal processing to be applied to a Polarization Division Multiplexed Quadrature Phase Shift Keying signal collected after an optical coherent receiver. The purpose of this work was to study different methods and parameters to use at the receiver in order to obtain the best system performances. Three types of optical receivers were presented: the direct detector, allowing the detection of the squared magnitude of the optical field and employed for intensity modulation only, the Mach-Zehnder demodulator followed by a direct detector, allowing the detection of phase modulated signals only, and finally the coherent receiver allowing the recovery of both phase and amplitude of any quadrature amplitude modulated signals. We revealed the building blocks of an optical coherent receiver.

The polarization diversity coherent receiver was detailed schematically and mathematically and the polarization variations in the optical fibre were exposed. The transmitter and local oscillator laser criteria along with the bandwidth of the analog to digital converters are exhibited as a function of the modulation format and symbol rate. A detailed analysis of laser phase noise followed and we explained its impact on the phase information.

We subsequently introduced the required digital signal processing to recover the information sent down the optical fibre and received through a polarization diversity coherent receiver, where impairments come from both the fibre and the receiver. We briefly discussed the minimum Nyquist sampling rate and we explained the origin of the impairments and ways to mitigate or suppress them. Thereafter, the metric used to analyse different methods and parameter values was presented and consisted of the final bit error rate yielded by the approach and the required amount of real additions and multiplications for post-processing, entitled the computational complexity.

Finally, we exposed the experimental setup used to capture several signals under different conditions, namely for two types of pulses, different launch powers with varying OSNRs. We analysed 10 different methods and parameters, extensively studied their impact on the system performances and found the best approaches based on our metric.

7.2 – Future Work

Several parameters and approaches studied in this work could be scrutinized more deeply. In this section, we propose possible directions for future research based on the work presented in this thesis.

The first study that would be interesting is an extension of our 6th comparison, where we adapt the demultiplexing coefficients h_{ij} for 2048 symbols and then leave them fixed. Our study shows that a fixed duration of 18432 symbols gives the same results as for 6144. Finding the longest fixed duration that gives a ROSNR penalty of 0.5 dB, for instance, would inform us how fast the PMD is varying in the fibre and would give the lowest computational complexity of this adaptive/fixed approach. Along the same vein, we could extend our study in *Comparison 7* to find the lower and the upper bound of the step size parameter μ and find the experimental convergence range of the CMA algorithm. We know that reducing the equalizer step size proportionally reduces the adaptation noise [63], but we could find the lower bound where μ is too small to converge.

We could also study other ways to subtract the carrier phase. We only used a single way in our study, i.e., the moving average window with different window lengths. We could study the impact on system performance by using other methods, for instance with a phase-locked loop. Another interesting approach would be to implement a CMA equalizer embedded with a decision-directed PLL, alleviating the need for separate operation of polarization demultiplexing, bulk carrier frequency offset removal and carrier phase estimation, which would most likely drastically reduce the total required computational complexity.

Finally and foremost, working on computationally more efficient ways to mitigate nonlinear effects in post-compensation through DSP is of capital importance. To increase to spectral efficiency and consequently the bit rate, higher order QAM signal constellations have to be employed, inherently requiring a higher OSNR at the receiver. For a signal like ours with a bandwidth of 20 GHz, theoretical ROSNRs for BER of 3.8×10^{-3} are 7.56 dB for QPSK and 11.21 dB for 16-QAM. Therefore, high OSNRs after long distances means higher launch powers, and accordingly more nonlinear effects imprinted on the signal. Proper information recovery for long haul transmissions is hardly attainable without implementable nonlinear processing in an ASIC semiconductor device for high powers.

References

[1] Cisco. (2010, May). *Cisco Announces Agreement to Acquire CoreOptics*. Available: http://newsroom.cisco.com/dlls/2010/corp_052010.html

[2] P. Winzer, "Beyond 100G Ethernet," *Communications Magazine, IEEE,* vol. 48, pp. 26-30, 2010.

[3] K. Roberts*, et al.*, "100G and beyond with digital coherent signal processing," *Communications Magazine, IEEE,* vol. 48, pp. 62-69, 2010.

[4] NEC. (2010, February). *Large-Capacity Optical Transmission Technologies Supporting the Optical Submarine Cable System*. Available: http://www.nec.co.jp/techrep/en/journal/g10/n01/100103.html

[5] M. Ohm and J. Speidel, "Differential optical 8-PSK with direct detection (8-DPSK/DD)," in *Photonische Netze (Photonic Networks), 5-6 May 2003*, Germany, 2003, pp. 177-81.

[6] M. Seimetz, "Performance of coherent optical square-16-QAM-systems based on IQ-transmitters and homodyne receivers with digital phase estimation," in *Optical Fiber Communication Conference, 2006 and the 2006 National Fiber Optic Engineers Conference. OFC 2006*, 2006, p. 10 pp.

[7] C. Toumazou*, et al.*, *Trade-Offs in Analog Circuit Design - The Designer's Companion*. Dordrecht, Netherlands: Springer, 2002.

[8] J. Lerdworatawee and N. Won, "Low noise amplifier design for ultra-wideband radio," in *Circuits and Systems, 2003. ISCAS '03. Proceedings of the 2003 International Symposium on*, 2003, pp. I-221-I-224 vol.1.

[9] M. Saiful Islam*, et al.*, "Distributed balanced photodetectors for broad-band noise suppression," *Microwave Theory and Techniques, IEEE Transactions on,* vol. 47, pp. 1282-1288, 1999.

[10] D. Syvridis*, et al.*, "Polarization state of the emission of external grating diode lasers," *Quantum Electronics, IEEE Journal of,* vol. 30, pp. 966-974, 1994.

[11] H.-C. Ji, *et al.*, "Effect of PDL-induced coherent crosstalk on polarization-division-multiplexed direct-detection systems," *Opt. Express,* vol. 17, pp. 1169-1177, 2009.

[12] T. Duthel, *et al.*, "Impact of Polarisation Dependent Loss on Coherent POLMUX-NRZ-DQPSK," in *Optical Fiber communication/National Fiber Optic Engineers Conference, 2008. OFC/NFOEC 2008. Conference on*, 2008, pp. 1-3.

[13] E. Hetch, *Optics*. San Francisco, CA, USA: Addison Wesley; 4th ed., 2001.

[14] A. E. Siegman, *Lasers*. Mill Valley, CA, USA: University Science Books, 1986.

[15] D. H. Ghafouri-Shiraz, *Distributed Feedback Laser Diodes and Optical Tunable Filters*. Chichester, West Sussex, UK: Wiley; 2nd ed., 2003.

[16] P. Gallion, *et al.*, "Single-frequency laser phase-noise limitation in single-mode optical-fiber coherent-detection systems with correlated fields," *J. Opt. Soc. Am.,* vol. 72, pp. 1167-1170, 1982.

[17] W. T. Silfvast, *Laser Fundamentals*. Cambridge, UK: Cambridge University Press; 2nd ed., 2008.

[18] J. R. Barry and E. A. Lee, "Performance of coherent optical receivers," *Proceedings of the IEEE,* vol. 78, pp. 1369-1394, 1990.

[19] B. E. A. Saleh and M. C. Teich, *Fundamentals of Photonics*. Hoboken, NJ, USA: Wiley-Interscience; 2nd ed, 2007.

[20] A. Yariv and W. Caton, "Frequency, intensity, and field fluctuations in laser oscillators," *Quantum Electronics, IEEE Journal of,* vol. 10, pp. 509-515, 1974.

[21] T. Hodgkinson, "Receiver analysis for synchronous coherent optical fiber transmission systems," *Lightwave Technology, Journal of,* vol. 5, pp. 573-586, 1987.

[22] X. Chen, "Ultra-Narrow Laser Linewidth Measurement," Doctor of Philosophy Dissertation, Electrical and Computer Engineering, Virginia Polytechnic Institute and State University, Blacksburg, Virginia, 2006.

[23] M. Azizoglu and P. A. Humblet, "Reference transmission and receiver optimization for coherent optical communication systems," in *NTC-92. National Telesystems Conference (Cat. No.92CH3120-3), 19-20 May 1992*, New York, NY, USA, 1992, pp. 14-1.

[24] H. Nyquist, "Certain Topics in Telegraph Transmission Theory," *American Institute of Electrical Engineers, Transactions of the,* vol. 47, pp. 617-644, 1928.

[25] H. J. Landau, "Sampling, data transmission, and the Nyquist rate," *Proceedings of the IEEE,* vol. 55, pp. 1701-1706, 1967.

[26] F. Derr, "Coherent optical QPSK intradyne system: concept and digital receiver realization," *Lightwave Technology, Journal of,* vol. 10, pp. 1290-1296, 1992.

[27] J. M. Madapura. (2008). *Achieving Higher ADC Resolution Using Oversampling - AN1152*. Available: ww1.microchip.com/downloads/en/AppNotes/Achieving Higher ADC Resolution Using Oversampling 01152A.pdf

[28] R. G. Lyons, *Understanding Digital Signal Processing*. Upper Saddle River, NJ, USA: Prentice-Hall, 2nd ed., 2004.

[29] S. Haykin, *Adaptive Filter Theory*. Upper Saddle River, NJ, USA: Prentice Hall, 4th ed., 2001.

[30] R. D. Gitlin, *Data Communications Principles*. New York, USA: Plenum Press, 1992.

[31] T. G. Hodgkinson*, et al.*, "In-phase and quadrature detection using 90° optical hybrid receiver: experiments and design considerations," *Optoelectronics, IEE Proceedings J,* vol. 135, pp. 260-267, 1988.

[32] J. G. Proakis, *Digital Communications*. New York, USA: McGraw-Hill Science, 5th ed., 2007.

[33] R.-J. Essiambre, "The Optical Fiber Channel: Limits to Capacity of Fiber-Optic Communication Systems," presented at the Fundamentals of Communications and Networks Workshop; Bell Labs - INRIA Workshop, Murray Hill, NJ, USA, 2009.

[34] G. Agrawal, *Nonlinear Fiber Optics*. San Diego, CA, USA: Academic Press; 4th edition, 2006.

[35] G. Agrawal, *Lightwave Technology Telecommunication Systems*. Hoboken, NJ, USA: John Wiley & Sons, Inc., 2005.

[36] H. C. Ji*, et al.*, "Effect of polarization dependent loss on polarization-shift-keying transmission system," in *APOC 2002: Optical Components and*

Transmission Systems, October 16, 2002 - October 18, 2002, Shanghai, China, 2002, pp. 313-318.

[37] M. Kuschnerov*, et al.*, "DSP for Coherent Single-Carrier Receivers," *Lightwave Technology, Journal of,* vol. 27, pp. 3614-3622, 2009.

[38] K. Roberts*, et al.*, "Performance of Dual-Polarization QPSK for Optical Transport Systems," *Lightwave Technology, Journal of,* vol. 27, pp. 3546-3559, 2009.

[39] C. D. Poole and R. E. Wagner, "Phenomenological approach to polarisation dispersion in long single-mode fibres," *Electronics Letters,* vol. 22, pp. 1029-1030, 1986.

[40] K. Kikuchi, "Polarization-demultiplexing algorithm in the digital coherent receiver," in *IEEE/LEOS Summer Topical Meetings, 2008 Digest of the*, 2008, pp. 101-102.

[41] J. Treichler and B. Agee, "A new approach to multipath correction of constant modulus signals," *Acoustics, Speech and Signal Processing, IEEE Transactions on,* vol. 31, pp. 459-472, 1983.

[42] S. J. Savory*, et al.*, "Electronic compensation of chromatic dispersion using a digital coherent receiver," *Optics Express,* vol. 15, pp. 2120-2126, 2007.

[43] S. J. Savory, "Digital filters for coherent optical receivers," *Optics Express,* vol. 16, pp. 804-17, 2008.

[44] P. J. Winzer*, et al.*, "56-Gbaud PDM-QPSK: coherent detection and 2,500-km transmission," in *Optical Communication, 2009. ECOC '09. 35th European Conference on*, 2009, pp. 1-2.

[45] H. Louchet*, et al.*, "Improved DSP algorithms for coherent 16-QAM transmission," in *Optical Communication, 2008. ECOC 2008. 34th European Conference on*, 2008, pp. 1-2.

[46] NewFocus. (24 May 2006). *TLB-7000 StableWave™ Tunable Lasers*. Available: http://www.newfocus.com/products/documents/catalog/215.pdf

[47] L. Andreas*, et al.*, "Frequency Estimation in Intradyne Reception," *Photonics Technology Letters, IEEE,* vol. 19, pp. 366-368, 2007.

[48] G. De Jonghe and M. Moeneclaey, "Cycle slip analysis of the NDA FF carrier synchronizer based on the Viterbi & Viterbi algorithm," in

Communications, 1994. ICC '94, SUPERCOMM/ICC '94, Conference Record, 'Serving Humanity Through Communications.' IEEE International Conference on, 1994, pp. 880-884 vol.2.

[49] A. Viterbi, "Nonlinear estimation of PSK-modulated carrier phase with application to burst digital transmission," *Information Theory, IEEE Transactions on,* vol. 29, pp. 543-551, 1983.

[50] K. Roberts*, et al.*, "Electronic precompensation of optical nonlinearity," *Photonics Technology Letters, IEEE,* vol. 18, pp. 403-405, 2006.

[51] L. E. Nelson*, et al.*, "Performance of a 46-Gbps Dual-Polarization QPSK Transceiver With Real-Time Coherent Equalization Over High PMD Fiber," *Lightwave Technology, Journal of,* vol. 27, pp. 158-167, 2009.

[52] Y. Z. Guoan Bi, *Transforms and fast algorithms for signal analysis and representations*. Boston, USA: Birkhäuser Boston; 1 edition, 2003.

[53] P. Duhamel, "Implementation of "Split-radix" FFT algorithms for complex, real, and real-symmetric data," *Acoustics, Speech and Signal Processing, IEEE Transactions on,* vol. 34, pp. 285-295, 1986.

[54] U. Meyer-Baeser, *Digital Signal Processing with Field Programmable Gate Arrays*. New York, USA: Springer; 2nd ed., 2007.

[55] Intel©. (2010, July). *Vector Math Library (VML) Performance and Accuracy Data*. Available: http://software.intel.com/sites/products/documentation/hpc/mkl/vml/vmldata.htm

[56] B. Châtelain*, et al.*, "Optimized pulse shaping for mitigating optical nonlinearity," in *Lasers and Electro-Optics, 2009 and 2009 Conference on Quantum electronics and Laser Science Conference. CLEO/QELS 2009. Conference on*, 2009, pp. 1-2.

[57] B. Châtelain*, et al.*, "Impact of pulse shaping on the SPM tolerance of electronically pre-compensated 10.7 Gb/s DPSK systems," in *Optical Fiber Communication (OFC), collocated National Fiber Optic Engineers Conference, 2010 Conference on (OFC/NFOEC)*, 2010, pp. 1-3.

[58] C. Fludger, "10 x 111 Gbit/s, 50 GHz spaced, POLMUX-RZ-DQPSK transmission over 2375 km employing coherent equalisation," presented at the Optical Fiber Communication, Post Deadline Paper, Anaheim, USA, 2007.

[59] Z. Xiang*, et al.*, "A novel DSP algorithm for improving the performance of digital coherent receiver using single-ended photo detection," in *Optical Communication, 2008. ECOC 2008. 34th European Conference on*, 2008, pp. 1-2.

[60] K. Seki, "Phase Ambiguity Resolver for PCM Sound Broadcasting Satellite Service with Low Power Consumption Viterbi Decoder Employing SST Scheme," *IEICE transactions on communications,* vol. E78-B(9), pp. 1269-1277, Septembre 1995.

[61] K. Seki*, et al.*, "Phase ambiguity resolver for coherent detection mobile wireless communication systems with a very low power consumption Viterbi decoder employing SST scheme," in *Universal Personal Communications, 1994. Record., 1994 Third Annual International Conference on*, 1994, pp. 210-214.

[62] K. Roberts and I. Roberts, "DSP: A disruptive technology for optical transceivers," in *Optical Communication, 2009. ECOC '09. 35th European Conference on*, 2009, pp. 1-4.

[63] N. K. Jablon, "Joint blind equalization, carrier recovery and timing recovery for high-order QAM signal constellations," *Signal Processing, IEEE Transactions on,* vol. 40, pp. 1383-1398, 1992.